University of Huddersfield

University of Huddersfield Repository

Liu, Yue

IN- SITU STRUCTURED LIGHT TECHNIQUES STUDY TO INSPECT SURFACES DURING ADDITIVE MANUFACTURE

Original Citation

Liu, Yue (2021) IN- SITU STRUCTURED LIGHT TECHNIQUES STUDY TO INSPECT SURFACES DURING ADDITIVE MANUFACTURE. Doctoral thesis, University of Huddersfield.

This version is available at https://eprints.hud.ac.uk/id/eprint/35704/

The University Repository is a digital collection of the research output of the University, available on Open Access. Copyright and Moral Rights for the items on this site are retained by the individual author and/or other copyright owners. Users may access full items free of charge; copies of full text items generally can be reproduced, displayed or performed and given to third parties in any format or medium for personal research or study, educational or not-for-profit purposes without prior permission or charge, provided:

- The authors, title and full bibliographic details is credited in any copy;
- A hyperlink and/or URL is included for the original metadata page; and
- The content is not changed in any way.

For more information, including our policy and submission procedure, please contact the Repository Team at: E.mailbox@hud.ac.uk.

http://eprints.hud.ac.uk/

IN- SITU STRUCTURED LIGHT TECHNIQUES STUDY TO INSPECT SURFACES DURING ADDITIVE MANUFACTURE

YUE LIU

A thesis submitted to the University of Huddersfield in partial fulfilment of the requirements for the degree of Doctor of Philosophy

The University of Huddersfield

July 2021

Copyright statement

i. The author of this thesis (including any appendices and/or schedules to this thesis) owns any copyright in it (the “Copyright”) and he has given The University of Huddersfield the right to use such copyright for any administrative, promotional, educational and/or teaching purposes.

ii. Copies of this thesis, either in full or in extracts, may be made only in accordance with the regulations of the University Library. Details of these regulations may be obtained from the Librarian. This page must form part of any such copies made.

iii. The ownership of any patents, designs, trademarks and any and all other intellectual property rights except for the Copyright (the “Intellectual Property Rights”) and any reproductions of copyright works, for example graphs and tables (“Reproductions”), which may be described in this thesis, may not be owned by the author and may be owned by third parties. Such Intellectual Property Rights and Reproductions cannot and must not be made available for use without the prior written permission of the owner(s) of the relevant Intellectual Property Rights and/or Reproductions

Acknowledgements (Preface)

Pursing the truth on the academic way is full of challenge. I believe one cannot overcome obstacles or resolve issues only relying on himself/ herself. Luckily, for me, there are so many great people who have given me help and assisted me to cross the barriers on my PhD study journey.

First and foremost, I would like to express sincere gratitude to my supervisor Professor Xiangqian Jiang for offering me the opportunity to join this advanced innovative laboratory to research structured light techniques and to entrust me with this topic. The guidance, support and freedom she granted me assisted me tremendously for my work. I appreciate all her contributions in providing me necessary facilities and funding to undertake this research and to attend international conferences inside and outside the UK. Especially, her charismatics and engaging academic research which inspired me for this scientific research.

I shall also express my deepest appreciation to my co-supervisor Prof. Liam Blunt for his valuable advice, technical assistance, full trust and the unreserved dedication on my research path. I starting additive manufacture research from scratch, his guidance and instruction in the research work assisted me magnificently. I am wholeheartedly grateful to his devotion and efforts. Additionally, I really appreciate the time and diligence he spent on reviewing and rectifying my writing including reports, papers and thesis.

I would also like to thank my co-supervisor, Dr. Feng Gao for his guidance, technical support and full trust in me. His advice and guidance in my research work have been of great help to me. I am wholeheartedly grateful to his devotion and efforts. In addition,

I am very grateful to him for the time and effort he has put into my writing, including reports, papers and essays.

My heartfelt thanks to Professor Zhang Zonghua of Hebei University of Technology. He provided the foundation for my introduction to structural light measurement and recommended me to study for a doctorate at University of Huddersfield. I would like to thank all the committee members of the EPSRC Center for Advanced Metering Innovation and Manufacturing, including Dr. Wenhan Zeng, Dr. Shan Lou, Dr. Luca Pagani, Dr. Prashant Kumar, Dr. Yongjia Xu, Dr. Yuchu Qin, Dr. Dawei Tang, Dr. James Williamson, Dr. Hussam Muhamedsalih, Dr. Tao Zhang, Dr. Duo Li and Mr. Chris Dawson and others. I would also like to thank the members of the cooperation company Wayland Additive, including Mr. Will Richardson, Mr. Ian Laidler and Mr. Chris Smith. I appreciate all the help and help they give me when I have problems. Finally, I will thank all my family members, friends and everyone I met in my life. The endless and unconditional help and love contribute all of me. I will give my huge thanks to my great country — China, who gives me everything. I deeply appreciate the maintenance support from China Scholarship Council (CSC).

Abstract

Three-dimensional (3D) shape measurement techniques play an increasingly important role in the quality control proceedures of industry, such as aerospace, bioengineering, information security, automobile, integrated circuits and so on. Additive manufacturing (AM) provide significant advantages over conventional subtractive manufacturing techniques in terms of the wide range of part geometry that can be obtained. The key metal AM technology is powder bed processing. During the AM process, powder delivery occurs thousands of times. Therefore, the assessment of delivery quality would be advantageous for the process to provide feedback for process control. After the energy source melts the powder bed, the detection of the machined surface is also a critically important criterion for the evaluation of the manufacturing quality. This thesis presents an in-situ quantitative inspection technique for the powder bed post raking and printed surface after melting, the technique uses fringe projection profilometry. In this thesis, system calibration methods, phase analysis algorithms, and error correction methods are investigated. A novel surface fitting algorithm is employed to reduce the influence of phase error and random noise during system calibration. A novel intelligent fringe projection technique using a support-vector-machine (SVM) algorithm is proposed to measure the 3D topography of high dynamic range surfaces on a layer by layer basis within the EBAM machine. A simple calibration method is used to eliminate phase errors during system calibration. The proposed in-situ inspection technique has been installed on a commercial electron beam melting (EBM) AM machine. Exemplar powder beds with defects and printed surfaces, are measured with the proposed technique. The whole inspection process lasts less than 5 seconds. Experimental results showed that the powder and the

melting surface defects could be efficiently inspected using the proposed system and the measurement result could be fed back to the build process to improve the processing quality.

For the inspection of highly reflective surface geometries that have been further machined post AM, phase measuring deflectometry (PMD) has been widely studied for the 3D form measurement. This thesis presents a new direct PMD (DPMD) method that measures the full-field 3D shape of complicated specular objects. A mathematical model is derived to directly relate an absolute phase map to depth data, instead of the gradient. The 3D shape of a monolithic multi-mirror array having multiple specular surfaces was measured. Experimental results show that the proposed DPMD method can obtain the full-field 3D shape of specular objects having isolated and/or discontinuous surfaces accurately and effectively.

In this thesis, the fringe projection and the deflectometry techniques are studied. Two different measurement systems were used to measure different roughness surfaces. The experimental results shows the rough surfaces, reflective surfaces, and the highly reflective specular surfaces can be measured and reconstructed by the proposed methods.

Contents

Abstract 5
List of Figures 10
List of Tables 16
List of abbreviation 17
Chapter 1 Introduction 18
1.1 Research background 18
1.1.1 Powder bed systems 19
1.1.2 Powder feed system 20
1.1.3 Wire feed system 21
1.2 Thesis layout 22
1.2.1 Electron Beam Additive Manufacturing process 23
1.3 Aims and Objectives 26
1.4 Contributions to knowledge 27
1.5 Journal Publications 28
1.6 Conference paper 29
Chapter 2 Literature review of additive manufacture and surface form metrology 30
2.1 Additive manufacture 30
2.1.1 Laser Powder Bed Fusion system (L-PBF) 30
2.1.2 Electron beam fusion system 32
2.2 Surface form metrology 34
2.2.1 Classification of 3D measurement technology 34
2.2.2 Encoding methods classification of structured light system 42
2.2.3 Structured light system for rough surface measurement 47
2.2.4 Structured light system for shiny surface measurement 50
2.2.5 Structured light system for high reflective surface measurement 52
2.2.6 Machine learning applications in structured light surface metrology 54
2.3 Phase analysis and algorithms 56
2.3.1 Phase calculation 56
2.3.2 Phase unwrapping algorithms 59
2.4 Other inspection methods in additive manufacture 63
2.4.1 In-process inspection techniques 63

2.4.2 Post-process inspection techniques 65
2.5 Summary 68
Chapter 3 Theoretical and experimental investigation of structure light system for rough surface 70
3.1 Introduction 70
3.2 3D measurement principle of structured light system based on sinusoidal patterns 72
3.2.1 Inspection system for AM 72
3.2.2 Measurement principle of the fringe projection technique 74
3.3 System calibration 76
3.3.1 Camera calibration 76
3.3.2 Depth calibration 81
3.3.3 Transverse calibration 89
3.4 Simulation 90
3.5 Phase error corrections 92
3.5.1 Surface fitting calibration 93
3.5.2 Whiteboard calibration 97
3.5.3 Nonlinear effect calibration 104
3.6 Deployment 106
3.6.1 Hardware and system 106
3.6.2 Software 109
3.7 System evaluation 110
3.7.1 Precision and resolution along transverse direction 110
3.7.2 Precision and resolution along z direction 112
3.8 Experimental 116
3.9 Summary 119
Chapter 4 Developed structure light system for high dynamic range surface based on machine learning 121
4.1 Introduction 121
4.1.1 Saturation issue in AM inspection 125
4.1.2 Traditional HDR methods 127
4.2 The measurement principle of HDR system 129
4.2.1 HDR method principle in AM 129
4.2.2 Classification principle of Support vector machines (SVM) 131

4.3 SVM training and testing 133
4.3.1 Binary classification 133
4.3.2 SVM training 135
4.3.3 SVM testing 137
4.4 Experiments 139
4.5 Summary 145
Chapter 5 Theoretical and experimental investigation of structure light system for high precision and reflective surface after post-machining 147
5.1 Introduction 147
5.2 Measurement principle of direct phase measurement deflectometry 148
5.2.1 DPMD based on LCD parallel position relationship 148
5.2.2 Based on arbitrary LCD position DPMD 151
5.3 Development of system 153
5.3.1 Prototype 1 with one camera and one projector 153
5.3.2 Prototype 2 with one camera and two LCDs 154
5.3.3 Prototype 3 with freedom position of LCDs 155
5.4 System calibration 155
5.4.1 Prototype 1 and 2 system calibration 155
5.4.2 Prototype 3 calibration 159
5.4.3 Chromatic aberration calibration 161
5.5 Experiment 163
5.6 Summary 167
Chapter 6 Conclusions and Future work 168
6.1 Conclusions 168
6.2 Future work 170
References 172

List of Figures

Figure 1. 1 Metal AM components 18
Figure 1. 2 Generic illustration of a powder bed system..... 20
Figure 1. 3 Generic illustrate of a powder feed system 21
Figure 1. 4 Generic illustrate of a wire feed system 22
Figure 1. 5 EBM Manufacture and inspection flow chart of additive manufacturing system..... 25
Figure 2. 1 (a) Schematic drawing of an laser-based AM machine and (b) Arcam EBAM machine 32
Figure 2. 2 Classification diagram of optical three-dimensional measurement technology..... 34
Figure 2. 3 The measurement principle of stereo vision technique 36
Figure 2. 4 TOF vision system 38
Figure 2. 5 Fizeau interferometer 39
Figure 2. 6 Measurement principle of Moiré Topography 40
Figure 2. 7 Example of the De Bruijn encoding [56] (a) Stripe-pattern by Zhang et al. (b) Multi-slit pattern similar to the one proposed by Monks et al. (c) Hybrid pattern in the RGB space. (d) Hybrid pattern intensity profile. 44
Figure 2. 8 Representative binary coding methods. (a) Simple binary coding; (b) Gray coding.[]..... 45
Figure 2. 9 Sinusoidal fringe patterns and the profiles 46
Figure 2. 10 Triangular patterns and the plot of the cross section..... 47
Figure 2. 11 Trapezoidal patterns and the plot of the cross section 47
Figure 2. 12 The principle of fringe projection technique..... 50
Figure 2. 13 Schematic diagram of deflectometry measurement principle 53
Figure 2. 14 Some types of deflectometry system 54
Figure 2. 15 Sinusoidal fringe patterns after phase shifting (a) i=1;(b)i=2;(c)i=3;(d)i=4 58
Figure 2. 16 Wrapped phase map by phase-shifting algorithm (a)wrapped phase map (b) the profile image of the wrapped phase that crosses line 70 59
Figure 2. 17 Unwrapped phase by optimum frequency selection phase unwrapping algorithm 60
Figure 2. 18 The principle of heterodyne phase unwrapping..... 61

Figure 2. 19 Fringe order $O_1(x)$ and unwrapped phase $\Phi_1(x)$ 62

Figure 2. 20 Classification of some optical methods according to their accuracy and working distance 67
Figure 3. 1 Typical powder bed defects..... 71
Figure 3. 2 A conceptual set up of the fringe projection inspection system 72
Figure 3. 3 A flow chart of build process 74
Figure 3. 4 (a) Schematic of fringe projection set up and (b) Camera image of deformed fringes 75
Figure 3. 5 A pinhole-imaging model..... 77
Figure 3. 6 A chessboard for camera calibration..... 79
Figure 3. 7 The position of the chessboard in the camera coordinate system..... 80
Figure 3. 8 Camera captured chessboard images (a) All captured images (b) Extracted corner points 80
Figure 3. 9 Camera calibration results..... 81
Figure 3. 10 Fringe projection system and ceramic calibration board with concentric circles 83
Figure 3. 11 The procedure of depth calibration..... 84
Figure 3. 12 Binarization and centre extraction of circle ring..... 86
Figure 3. 13 Compared with two obtaining depth data methods in AM system 87
Figure 3. 14 Two fringe projection system with different view angles and the centre extraction errors(a)AM fringe projection system (b) The camera face to the calibration board (c) centre extraction error in ellipse centre (d) extraction in circle ring 88
Figure 3. 15 Two obtaining depth method when the camera directly face to the calibration board..... 88
Figure 3. 16 Schematic of transverse calibration 89
Figure 3. 17 The transvers calibration procedure flowchart..... 90
Figure 3. 18 Simulation of measurement accuracy for the proposed method 92
Figure 3. 19 Phase error and measurement error (a) The impact of calibration board black circle rings on captured phase data (b) The measurement results due to the effects of the black circle rings on the calibration board (c) The zoomed area of the measurement results..... 93

Figure 3. 20 Wrapped phase map and unwrapped phase map after identifying outliers(a) Wrapped phase with the outliers removed (b) Unwrapped phase without the outliers..... 94
Figure 3. 21 Compared measured distance along one row near the middle of the white plate results between before and after corrections, X axis represents the pixel positions, vertical axis is the reconstructed depth of the surface (a) z=-2.5 mm (b) z=2.5mm 96
Figure 3. 22 3D shape measurement results of a flat plate (a) 3D shape measurement results with impact of black circle ring (b) 3D shape measurement results with the proposed method 97
Figure 3. 23 The procedure of the depth calibration..... 98
Figure 3. 24 The procedure of transverse calibration..... 99
Figure 3. 25 Measurement results of a flat plate (a) 3D shape measurement results with impact of black circle ring (b) 3D shape measurement results with the proposed method 100
Figure 3. 26 Compared measured distance along one row near the middle of the white plate results, X axis represents the width, vertical axis is the reconstructed depth of the surface (a) z=-5.4 mm (b) z=1.3mm 101
Figure 3. 27 A twenty-cent coin and 3D reconstruction results. (a) Photograph of the coin; (b) 3D measurement results of the coin after corrections. (c) 3D measurement results of the coin before corrections (b) Zoom in the error..... 102
Figure 3. 28 The 2D profile of the measurement error because of ring effect. 103
Figure 3. 29 Printed metal sample and 3D reconstruction results. (a) Photograph of tested printed sample (b) Areal map of tested printed sample before corrections (c) Areal map of tested printed sample after corrections 103
Figure 3. 30 The relationship of input intensity and output intensity..... 105
Figure 3. 31 Hardware of fringe projection system (a) DLP projector (b) CCD camera 107
Figure 3. 32 Fringe projection system with an interferometer (a) Prototype 1 system (b) Measurement result of a 3D-printed part 107
Figure 3. 33 Powder delivery system with fringe projection system (a) Prototype 2-implemented on powder delivery system (b) exemplar measurements..... 108
Figure 3. 34 Prototype 3 system with inspection system in a new EBM machine .. 109
Figure 3. 35 The control software of fringe projection system 110

Figure 3. 36 Measurement accuracy and error range in X and Y directions (a) X direction (b) Y direction 111
Figure 3. 37 Error range compared with interferometer and depth evaluation results (a) the measurement relationship between the fringe projection system and the interferometer (b) measurement accuracy and error range in Z directions..... 113
Figure 3. 38 The profile of four testing positions that are measured by fringe projection system 113
Figure 3. 39 The profile of one sinusoidal signal with one period..... 114
Figure 3. 40 Illustration of the standard ceramic step and measured 3D shape data prototype 2 (a) Photograph of the standard ceramic step (b) the measured 3D shape 115
Figure 3. 41 Partially built parts within powder bed post a single build cycle 117
Figure 3. 42 Excessive powder delivery on top of partially build parts (a) Photograph of tested powder bed (b) Areal map of tested powder bed..... 117
Figure 3. 43 Areal map and extracted profiles of the excessive powder delivery (due to rake damaged) on top of partially build parts 117
Figure 3. 44 3D measurement results of the building process 118
Figure 3. 45 A finished part measurement result..... 119

Figure 4. 1 The saturation issue appears when the Ebeam melts the metal powder and the surface becomes shiny (a) Fringe pattern with saturation pixels (b) 3D data with saturation issue..... 125
Figure 4. 2 A typical EBAM Manufacture and inspection flow chart of additive manufacturing system 126
Figure 4. 3 The reflective properties of the metal surface 127
Figure 4. 4 Multi exposures measurement results..... 128
Figure 4. 5 The two separate exposure measurement results merged 129
Figure 4. 6 The classification principle of SVM (a) Support vectors delimiting the margin between classes. (b) Samples mapping from input space into feature space 132
Figure 4. 7 Schematic diagram of SVM multi-classification method..... 133
Figure 4. 8 Standard part manufacturing by turning for dichotomous classification 133
Figure 4. 9 Dichotomous classification imaged for training 134
Figure 4. 10 SVM Dichotomous classification results..... 134

Figure 4. 11 The process of “shiny” surface inspection 135
Figure 4. 12 Training and verification flow chart of SVM classifier 136
Figure 4. 13 The training surfaces which manufactured by spark erosion..... 136
Figure 4. 14 The scatter diagram of manufacturing surfaces 137
Figure 4. 15 The test samples compared with predict samples..... 138
Figure 4. 16 The training surfaces which manufactured by EBAM 138
Figure 4. 17 The test samples compared with predict samples..... 139
Figure 4. 18 Prototype system with fringe projection system in a new EBM machine 140
Figure 4. 19 The captured fringes with two measurements and the merged fringes 141
Figure 4. 20 The wrapped phase and the unwrapped phase with the fringe frequency 81 80 72 142
Figure 4. 21 The measurement result of a manufacturing square 143
Figure 4. 22 Measurement result of printed parts with prediction exposure time (X and Y represent the size of the square projected measured surface) 144
Figure 5. 1 Schematic setup of the 3D measurement system based on moving 149
Figure 5. 2 A deflectometry system based on beam splitter..... 150
Figure 5. 3 Schematic setup of the developed 3D deflectometry system 151
Figure 5. 4 Prototype 1 with one camera and one projector..... 153
Figure 5. 5 Prototype 2 with one camera, two screens and a BS 154
Figure 5. 6 Prototype 3 with arbitrary position of LCDs 155
Figure 5. 7 Schematic of the calibration method 155
Figure 5. 8 Schematic calibration method of the 3D measurement system, prototype 2 156
Figure 5. 9 Diagram of the calibration of d 158
Figure 5. 10 Diagram of R/T matrices Calibration Method 159
Figure 5. 11 The calibration results of camera 160
Figure 5. 12 Applications of multi-colour channels acquisition in fringe projection system..... 161
Figure 5. 13 The fringe aberration between the red and blue channels for all columns 163
Figure 5. 14 Hardware of the prototype 2 system and prototype 3 system 164
Figure 5. 15 Measured depth of the measured step..... 165

Figure 5. 16 A monolithic multi-mirror array on the MIRI Spectrometer Optics for the James Webb Space Telescope 166
Figure 5. 17 Phase of the monolithic multi-mirror array. (a), (b), (c) are three wrapped phase maps having 64, 63 and 56 projected fringes, while (d) is the absolute phase map 166
Figure 5. 18 Measured depth of the monolithic multi-mirror array 167

List of Tables

Table 3. 1 Internal parameters of the camera 81
Table 3. 2 Measured distance compared with the interferometer measurement..... 96
Table 3. 3 Details of the accuracy and precision along depth direction..... 101
Table 3. 4 Details of the accuracy and precision along transverse direction..... 110
Table 3. 5 Details of the accuracy and precision along depth direction..... 112
Table 3. 6 The experimental results on the measured step (Unit: μm)..... 115
Table 4. 1 The prediction results 138
Table 5. 1 Internal parameters of camera 161
Table 5. 2 [R1,T1] matrix..... 161
Table 5. 3 [R2 T2] matrix..... 161
Table 5. 4 Experimental results for the accurately positioned mirror (Unit: mm) 164
Table 5. 5 Experimental results on the measured step (Unit: mm)..... 165

List of abbreviation

AM	Additive Manufacturing
EBM	Electron beam melting
3D	Three-dimensional
EBAM	Electron Beam Additive Manufacturing
ASTM	American Society for Testing and Materials
PBF	Powder Bed Fusion
DMLS	Direct metal laser sintering
SHS	Selective heat sintering
SLM	Selective laser melting
SLS	Selective laser sintering
L-PBF	Laser powder bed fusion
CAD	Computer-Aided Design
PMD	Phase measuring deflectometry
CCD	Charge-coupled device
CMM	Coordinate measuring machine
PSI	Phase shifting interferometry
WLI	White light interferometry
WSI	Wavelength scanning interferometry
DPMD	Direct Phase measuring deflectometry
LCD	Liquid Crystal Display
DOF	Depth of Field
CCD	Charge-Coupled Device
FOV	Field of View
LUT	Lookup Table
HDR	High dynamic range
CNN	Convolutional neural network
SVM	Support Vector Machine
KNN	K-Nearest Neighbors
RBN	Restricted Boltzmann Machine

Chapter 1 Introduction

1.1 Research background

Additive manufacturing (AM) techniques of metallic materials, also referred to as three-dimensional (3D) printing, has become a practical fabrication technology and has been developing rapidly in both industrial and academic fields in recent years. AM provides significant advantages in manufacturing complex geometries and internal features by adding powder material one cross-sectional layer at a time [1]. Due to its processing advantages, AM can create parts ideal for demanding applications which are lightweight, complex, and strong [2]. Figure 1.1 shows three metal AM components. Figure 1.1(a) and (b) are the turbine wheels manufactured by AM, which reduced the internal weight and can increase the component life, as well as reducing wear on bearings. Figure 1.1(c) shows a complex hollow structure, which reflects that AM can manufacture complex internal structures. Therefore, it has big potential for applications in both aerospace automotive and medical implant fields amongst many others.

Figure 1. 1 Metal AM components

In 2009, Bourell et al. reported a roadmap for AM based on the idea of key elements of the total AM manufacturing chain. They were divided into five important facets of AM which are Design; Process modelling and control; Materials, processes, and AM machines; Biomedical applications; Energy and sustainability applications [3]. From this, how to manufacture products efficiently and reliably is a key factor in AM. There

are many challenges and research issues that need to be addressed, including improving part surface finish, improving the mechanical performance of printed parts, and reducing stress concentrations, defect detection/embedded material discontinuities, and reduction in inter-build variation [4]. Consequently, in-situ inspection is “cornerstone” technology during the AM process that can critically aid in improving product quality and reduce material consumption. According to the ASTM classification [ISO/ASTM 52900] [5] methods of metal additive manufacturing can be divided into three categories which are powder bed system, powder feed system, and wire feed system.

1.1.1 Powder bed systems

Figure 1.2 shows a generic schematic diagram of a general powder bed system which consists of a transfer device (built plate and transfer stage), melting device (energy source), and powder delivery device. Each layer of powder (10-100µm) is dispensed from a powder hopper and the powder layer is raked across the work area. The energy source (electron beam or laser) is programmed to melt or sinter the powder at fixed locations to give the desired shape for each layer. This process is repeated thousands of times to create a solid three-dimensional component. This type of AM machine uses an enclosed chamber. The electron beam system is additionally under vacuum, the laser system operates in an inert gas environment. The powder bed system is used to manufacture high-resolution features, internal structure whilst maintaining good maintain dimensional control.

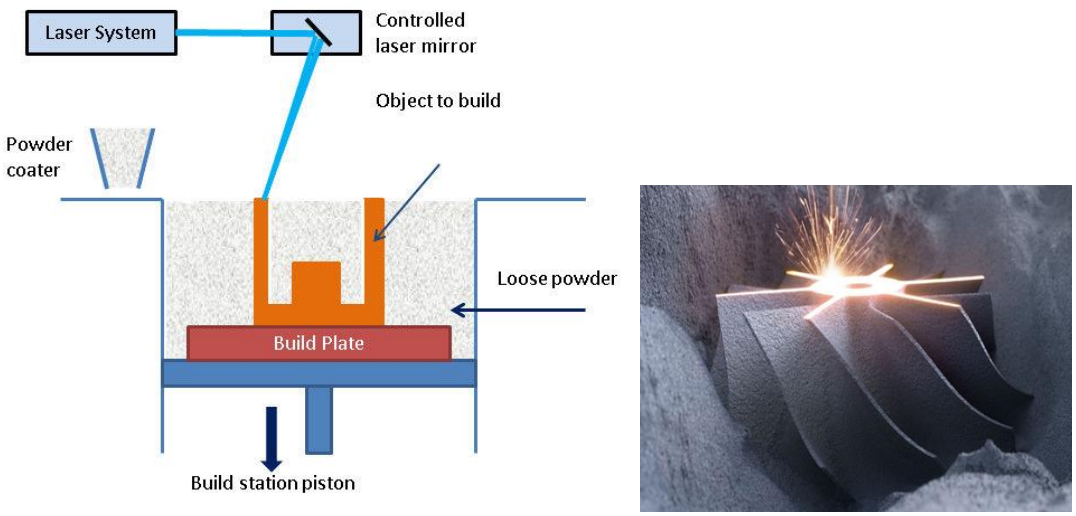

Figure 1. 2 Generic illustration of a powder bed system [6]

1.1.2 Powder feed system

Figure 1.3 is a generic illustration of AM powder feed system, which consists of a laser system, a coaxial powder deposition device (powder size range of 60–150 μm), a control system, and a transfer system. Compared with powder bed systems, powder feed systems lend themselves more readily to build large volume scales. In other words, the build volumes from these systems are generally larger, for example, the size can reach over 1.2 m^3. In these systems, metal powder is conveyed from a nozzle onto the workpiece surface. A melt source is used to melt the monolayer conveyed powder or more of the powder into the designed shape. The melt source continuously melts the metal powder or the previously deposited metal and base metal to build a thin deposited layer. This process is repeated thousands of times to create a 3D component. For the transfer device, there are two main types of systems. The first type is that the printed piece is fixed, and the deposition head moves. The second type is that the deposition head remains stationary, and the printed piece moves. These systems have the ability to manufacture big size printed pieces and to refurbish worn

or damaged components. They are operated in a non-enclosed environment. However dimensional control is poor than the powder bed systems.

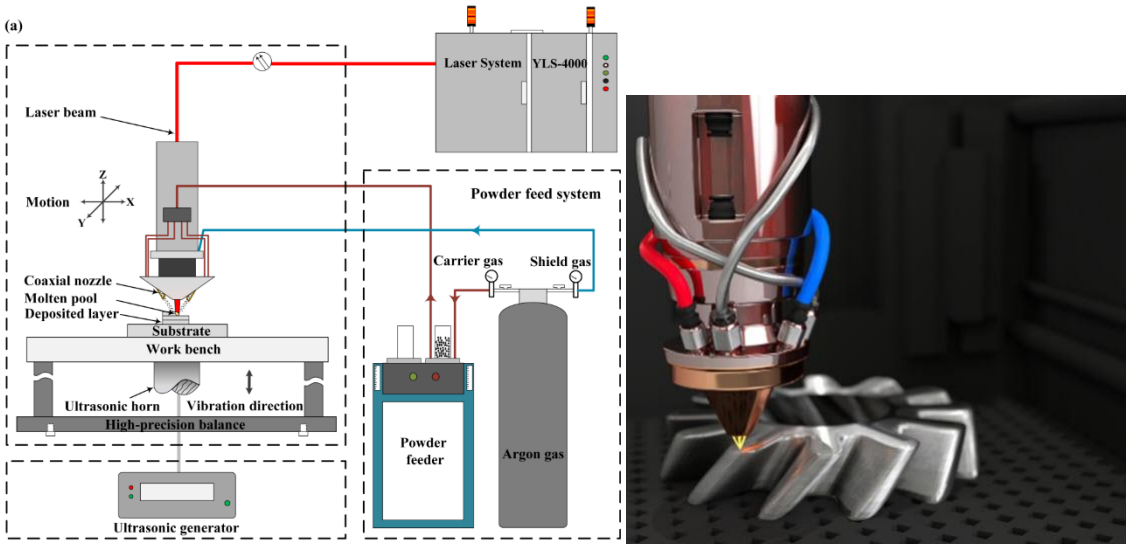

Figure 1. 3 Generic illustrate of a powder feed system [7]

1.1.3 Wire feed system

Figure 1.4(a) is a schematic of a wire feed system. These systems are similar to powder feed systems. The difference between wire feed system and powder feed system is the different feedstock methods. The energy source for these units can include electron beam, laser beam, and plasma arc. These systems are also used to build large volume scale parts. The wire is conveyed and the melt metal is deposited until to create the designed 3D products. In general, wire feed systems are well suited for high deposition rate processing and large volume building. However, the dimensional accuracy of the printed samples is low which usually requires secondary machining. Figure 1.4(b) is an example of the printed sample manufactured by a wire feed system.

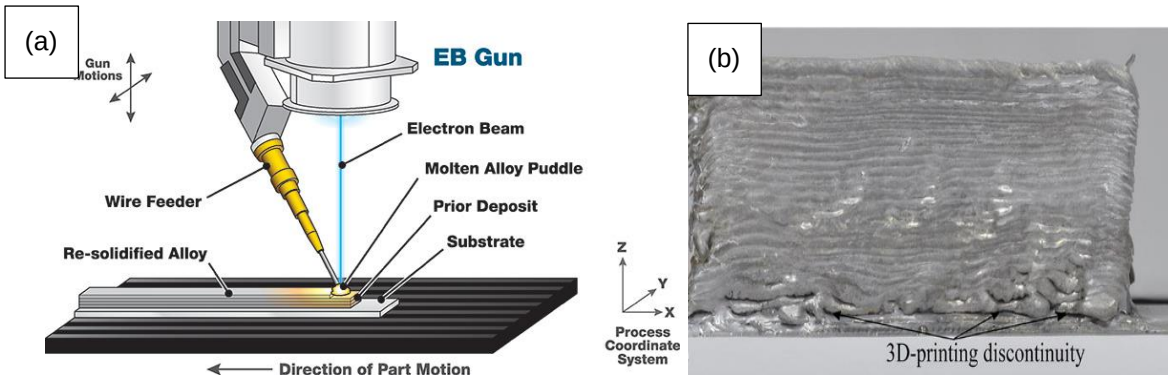

Figure 1. 4 Generic illustrate of a wire feed system [8]

1.2 Thesis layout

This thesis consists of nine chapters including the introduction and references. A synopsis of chapter 2 to chapter 6 is provided in this section. In addition, a brief rationale for the experimental methods and the novelty of this thesis are discussed.

- Chapter 2 is the current literature review work of AM and surface form metrology, comprising of three sections. Section 2.1 is an overview of AM, section 2.2 is a review of surface form metrology, and section 2.3 section describes the phase wrapping and phase unwrapping algorithms to analyse the phase information in 3D measurement technologies. 2.4 is a review of the others surface metrology for metal AM and section 2.5 is a summary.
- Chapter 3 presents the developed and deployed inspection system that is based on fringe projection profilometry technique. Section 3.1 is overview of fringe projection technique. Section 3.2 describes the measurement principle of fringe projection profilometry. Section 3.3 presents system calibration work by combining a fitting algorithm. Section 3.4 is simulation. Section 3.5 is phase error corrections. Section 3.6 is hardware and software introduction. Section 3.7 is system evaluation. Section 3.8 is experiment work. Section 3.9 is a summary.

- Chapter 4 describes the developed fringe projection system for shiny surface measurement. Section 4.1 is an overview of high dynamic range measurement. Section 4.2 describes the measurement principle of printed surface in AM based on developed fringe projection profilometry. Section 4.3 presents the training and testing method of a machine learning algorithm. Section 4.4 is the experiment work of high dynamic range measurement. Section 4.5 is a summary.
- Chapter 5 presents a direct phase measurement deflectomety system for high reflective surface measurement. Section 5.1 is the introduction of the deflectomety system. Section 5.2 is the measurement principle of deflectometry. Section 5.3 is the development of the system. Section 5.4 present the system calibration methods. Section 5.5 is experiment work. Section 5.6 is a summary.
- Chapter 6 presents the conclusion of this research work and the future work.

1.2.1 Electron Beam Additive Manufacturing process

Electron Beam Additive Manufacturing (EBAM) is one of the powder bed fusion techniques with the electron beam as the powder melting source. For the EBAM process, two significant steps are pre-sintering of powder post-delivery, and powder melting namely metal solidification, these two processes are integral to AM and they occurs many thousands of times during a build cycle. If the powder delivery process is dysfunctional then after the melting and solidification process, cracks and pores can occur within the printed objects due to the low quality or inconsistency of the powder delivery [9]. If the solidified surface is out of the plane due to thermal swelling for example, powder rake damage and product failure can still occur during the process. Hence one function of an effective in-situ detection approach for assessment of

powder delivery quality and to inspect each layer after build to inspect in and out of the plane is essential to improve manufacturing precision and to enhance product quality [10].

The EBAM manufacturing process is shown in Figure 1.5. After process parameters are set, a layer of powder is dispensed from a powder hopper. For an effective in-situ metrology inspections system, the system must first inspect the powder bed to assess if the surface is defect-free enough to carry on with the melting process. Once the powder layer is distributed well, a 2D slice is melted using an energy beam applied to the powder bed. If the powder delivery is assessed as deficient then the power delivery will be repeated until the surface is smooth enough or the process terminated. Secondly after the powder fusion, the inspection system should inspect the printed part to detect lateral print dimensions and out of plain error. If no problems are detected or the problem can be resolved through changing process parameters, then the build will carry on, if a problem is detected i.e. the part build deviation is beyond a given threshold then the build is halted.

This whole process is repeated throughout the build cycle until the build is complete. After the build is completed, the completed part can be post-processing or further inspected under measurement laboratory conditions. X-ray Computer Tomography, are applied to detect internal defects. If the internal inspection meets the requirements the post build inspection process can proceed, e.g. after additional surface subtractive machining, inspection systems inspects the final dimensions and surface. Between powder delivery and melting, there are 4–5 seconds AM machine preparation time, an in situ inspection system must make use of this gap to inspect the powder bed to avoid

time constraints on the total part build budget. The time for the printed part inspection follows to same logic as the first powder bed inspection.

In this thesis, the author will focus on addressing three key issues during the AM process. Firstly the challenge for an optical in-situ optical inspection system is to inspect the state of the rough powder bed to assess the powder delivery. After the melted the EBM powder cools, the metal powder is solidified and the reflective characteristic of the surface changes from diffuse to highly reflective, especially the reflective properties of the solidified metal surface will be changed when the EBM power changes. Consequently the second challenge is to inspect the rough powder bed and the reflective metal surface at the same time thus requiring a high dynamic range because after solidifying, the surface will be reflective and high precision. The third challenge is to develop an optical system that has high-precision reflective surface detection capability.

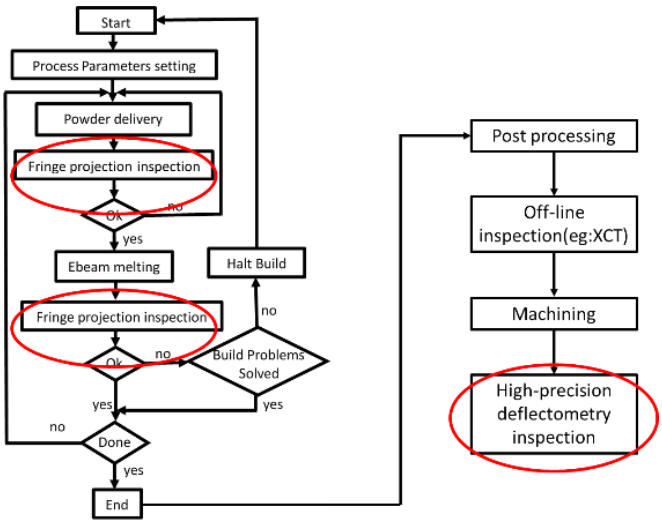

Figure 1. 5 EBM Manufacture and inspection flow chart of additive manufacturing system

Machine vision technology has become the future development trend for powder bed detection, flaw detection, and performance detection in additive manufacturing. 3D

measurement can provide depth information compared to 2D photogrammetry. The fringe projection technique is an effective 3D inspection techniques with the advantages of a full field, high speed, high accuracy, low cost, and large field of view [11,12,13,14]. Fringe projection techniques can inspect rough surfaces, such as the powder bed, non-reflective manufacturing surface in AM systems. However, during the melting and solidification process, some surface characteristics can be changed, some surfaces become shiny, reflective, or even specular this is challenging for fringe projection techniques. When reflective shiny metal surface are captured by the camera, the phase information is lost, resulting in the loss of depth information. In these situations, a further developed fringe projection technique that can measure high dynamic range surface needs to be investigated. Deflectometry is another effective 3D measurement technique that can measure reflective surfaces. For these optical inspection techniques, many issues need to be addressed, such as system calibration, phase analyses, high dynamic range measurement, geometric modeling, error correction, etc. Solving these issues for in situ AM can not only address the key issues in AM process but also can be applied to other industrial fields.

1.3 Aims and Objectives

The aim of the present research is to develop techniques to inspect the shape of the rough powder bed, printed powder, and final reflective surface. The technique should meet several key criteria. Firstly, during the AM process, the resolution of the in-situ inspection needs to be 0.05 mm with 200mm×200mm field of view. Secondly, both two in-situ inspection processes' times must be under 5 seconds. Thirdly, after AM processing a layer, the system must achieve non-continuous reflective surface measurement.

The specific objectives are given to fulfil the above aims, as follows:

- To review state-of-the-art 3D form measurement techniques, fringe projection system calibration techniques, and inspection techniques in AM.
- To theoretically and experimentally investigate methods of the rough surface inspection, reflective surface inspection, and specular surface inspection.
- To develop a 3D inspection system for rough surface measurement in AM.
- To develop a 3D inspection system for high dynamic range surface measurement to analyse printed components.
- To develop a 3D inspection system for non-continuous specular surface measurement.
- To research novel system calibration methods for the rough surface inspection system and novel system calibration methods for the non-continuous reflective surface system.
- To research phase analyses methods for high-speed measurement.
- To research machine-learning algorithms applied in 3D inspection techniques to address high dynamic range issues.
- To deploy the developed system in a “real” EBeam environment.

1.4 Contributions to knowledge

The research work in this thesis includes the following contributions to knowledge:

- Theoretical and experimental investigation of the fringe projection system calibration to obtain high accuracy and eliminate calibration board marks effect
- The theoretical and experimental investigation of the fringe projection system for the powder bed inspection in AM process.

- Developing an intelligent fringe projection system for high dynamic range surface inspection in AM.
- The theoretical and experiment investigation of the deflectometry systems for dis-continues specular surface inspection and calibration methods.

1.5 Journal Publications

1. Liu Y, Blunt L, Zhang Z, Rahman HA, Gao F, Jiang X. In-situ areal inspection of powder bed for electron beam fusion system based on fringe projection profilometry. Additive Manufacturing. 2020 Jan 1;31:100940[15].

2. Liu Y, Blunt L, Gao F, Jiang XJ. High-dynamic-range 3D measurement for E-beam fusion additive manufacturing based on SVM intelligent fringe projection system. Surface Topography: Metrology and Properties. 2021 Jun 17[16].

3. Liu Y, Blunt L, Gao F, Jiang X. A Simple Calibration Method for a Fringe Projection System Embedded within an Additive Manufacturing Machine. Machines. 2021 Sep;9(9):200[17].

4. Liu Y, Huang S, Zhang Z, Gao N, Gao F, Jiang X. Full-field 3D shape measurement of discontinuous specular objects by direct phase measuring deflectometry. Scientific reports. 2017 Aug 31;7(1):1-8[18].

5. Huang S, Liu Y, Gao N, Zhang Z, Gao F, Jiang X. Distance calibration between reference plane and screen in direct phase measuring deflectometry. Sensors. 2018 Jan;18(1):144[19].

6. Zhang Z, Wang Y, Huang S, Liu Y, Chang C, Gao F, Jiang X. Three-dimensional shape measurements of specular objects using phase-measuring deflectometry. Sensors. 2017 Dec;17(12):2835[20].

1.6 Conference paper

1. Liu Y, Blunt L, Gao F, Jiang J. In-situ high dynamic range inspection in Ebeam machine based on fringe projection profilometry. In21st International Conference of the European Society for Precision Engineering and Nanotechnology 2021 Jun 10. Euspen[21].

2. Blunt L, Liu Y, Zhang Z, Smith C, Knight D, Gao F, Townsend A, Jiang X. An in-process, layer wise surface metrology system for a new E-Beam additive manufacturing machine. In20th International Conference of the European Society for Precision Engineering and Nanotechnology 2020 Jun 8 (pp. 565-568). Euspen[22].

3. Liu Y, Zhang Z, Blunt L, Saunby G, Dawes J, Blackham B, Rahman HA, Smith C, Gao F, Jiang X. In-situ inspection system for additive manufacturing based on phase measurement profilometry. In19th International Conference of the European Society for Precision Engineering and Nanotechnology 2019 (pp. 324-327). Euspen[23].

4. Liu Y, Zhang Z, Blunt L, Saunby G, Dawes J, Blackham B, Rahman HA, Smith C, Gao F, Jiang X. In-situ areal inspection of powder bed for electron beam fusion AM system based on fringe projection. In2018 ASPE and euspen Summer Topical Meeting on Advancing Precision in Additive Manufacturing 2018 (pp. 259-264). American Society for Precision Engineering, ASPE[24].

Chapter 2 Literature review of additive manufacture and surface form metrology

This chapter provides a review of the additive manufacturing and current state-of-the-art 3D measurement techniques. The chapter is divided into four sections: section 2.1 is an overview of AM, section 2.2 is a review of surface form metrology, and section 2.3 is phase analysis and algorithms, and section 2.4 is a review of the others surface metrology for metal AM and section 2.5 is a summary.

2.1 Additive manufacture

Additive manufacturing technologies were categorized into seven types by the International Organization for Standardization (ISO/ASTM 52900 [5]). They are vat photo polymerization, material extrusion, sheet lamination, powder bed fusion, binder jetting, material jetting, and directed energy deposition [25]. This thesis specifically focuses on one of them, Powder Bed Fusion (PBF). PBF is a technology that realizes 3D printing by melting powder over a plate surface. This 3D printing technique includes the following techniques: Direct metal laser sintering (DMLS), Electron beam melting (EBM), Selective heat sintering (SHS), Selective laser melting (SLM), and Selective laser sintering (SLS). According to the heat source, the powder bed system can be divided into laser powder bed fusion system (L-PBF) and electron beam powder bed fusion system, where electron beam melting is carried out under vacuum.

2.1.1 Laser Powder Bed Fusion system (L-PBF)

The powder bed fusion systems consists of a transfer device (built plate and transfer stage), a melting device (provide the thermal energy to melt the powder), and a powder delivery device (blade or roller for spreading powder) as shown in Figure 1.2. The

peculiar nature of L-PBF is using laser as the energy source which is the photons (generated by the laser source) interaction with the powder bed. The size of powder level is micro (10-50µm) and the manufacturing process is in an inert gas atmosphere. There are a lot of physical processes involved, such as transmission and reflection of laser energy, particles adhesion, powder melting and solidification, molten metal flow and a microstructural evolution [26]. An illustration of the L-PBF manufacturing principle is shown in Figure 2.1(a). The component is manufactured layer by layer. The powder roller delivers one layer of powder to the work area, then the laser melts the new powder at specific locations as guided by the CAD layer wise design. The powder is solidified as soon as the laser moves to the neighbouring powder portion until the designed shape is obtained. The final component is an ensemble of micron-size welding lines overlapping from a thin layer of metal powder to a 3D structure part. The temperature in the centre of the laser beam usually reaches 1500-Celsius degrees, which is much higher than the melting point of metal powder. This L-PBF system has the capability to manufacture the product with an upper surface roughness value of Ra 4-10µm [27]. Laser-based AM approaches have the potential to improve the manufacturing quality in aerospace, medical, and industrial processes [28]. Following part build, the parts must be removed from the build plate by wire erosion cutting and then must be heat treated to remove induced thermal stresses.

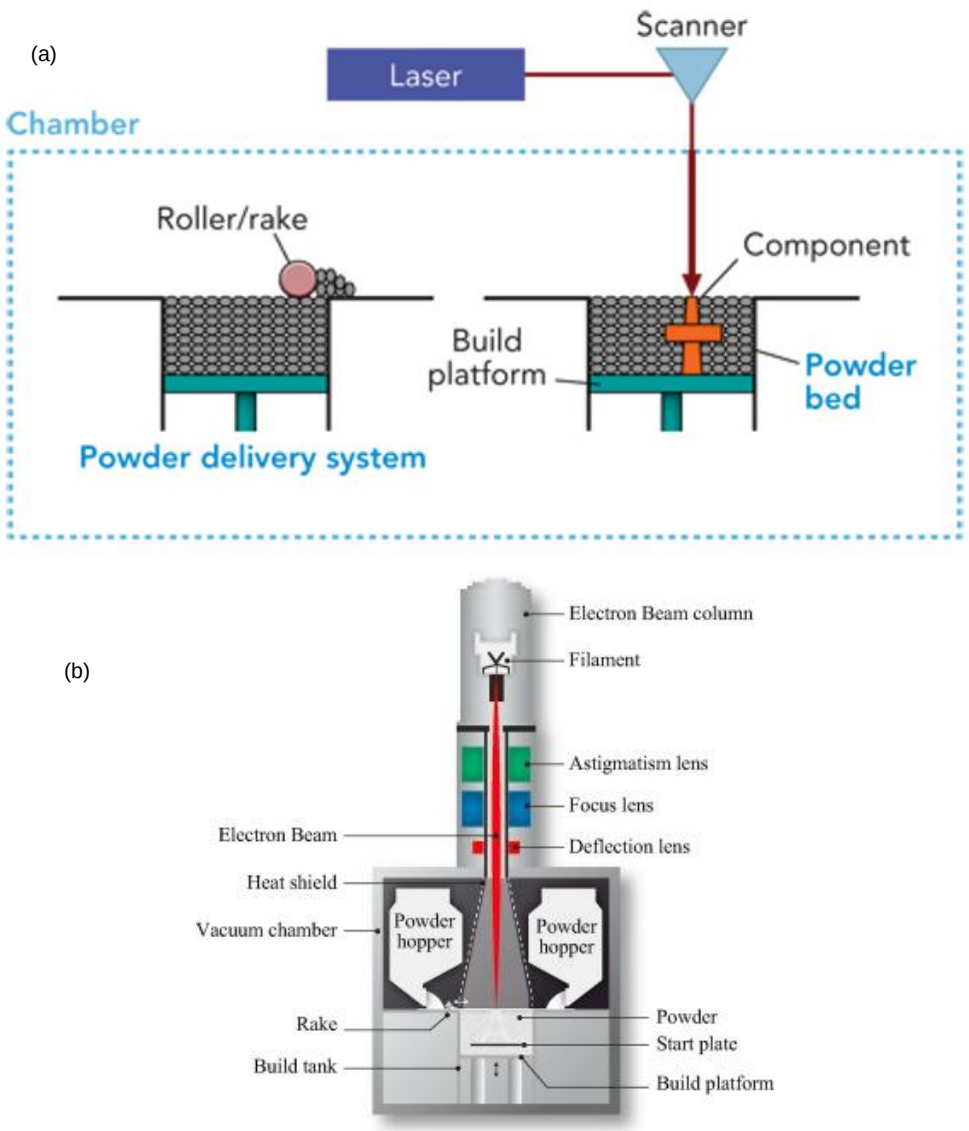

Figure 2. 1 (a) Schematic drawing of an laser-based AM machine [29] and (b) Arcam EBAM machine [30]

2.1.2 Electron beam fusion system

Electron beam fusion systems namely electron beam additive manufacturing (EBAM), is another powder bed fusion-based AM system. In these systems, the power source is an electron beam that is used to fuse powder bed instead of a laser. Figure 2.1(b) shows a schematic of the ARCAM EBAM machine which was commercialized in Sweden in 1997. Electrons are emitted by a heated tungsten filament, which is accelerated and controlled by two magnetic coils. In the middle part of the machine is

the powder bed build stage. The metal powder, the particles size is in the range of 40-100 µm. Each layer of powder is delivered by a hopper and forms a thin layer by a rake before each layer build and the typical layer thickness is in the range of 0.05–0.2 mm. After powder bed delivery, the electron beam scans on the powder bed at specific locations as guided by the CAD layer wise design, which melts the powder bed. Each powder layer is scanned in two stages, the preheating stage (to lightly sinter/bind the powder in the build region) and the melting stage. A high scanning speed beam first scans the powder to a sintered state in the preheat stage, while a low scanning speed beam melts the powder until one layer is completed. After one layer is finished the transfer stage is lowered, the new layer powder is spread from the hopper. This process repeats thousand times until all layers are printed. Inside the chamber, the build process takes place in a high vacuum with 10^{-4} to 10^{-5} mbar [31]. A wide range of materials can be used in EBAM systems, such as titanium alloys(Ti-6Al-4V, Ti-6Al-4V EI), cobalt chrome, titanium aluminide, Inconel (625 and 718), stainless steels, tool steels, copper, aluminium alloys, beryllium, and so on[32] Post build the part can be easily removed from the build plate and there is no requirement for heat treatment.

SLM and EBAM systems are two of the most promising additive manufacturing technologies that can make full-density metallic components using CAD assisted layer-by-layer fabrication methods. Compared with the SLM system, the EBAM system can achieve higher build rates; because it has high energy density and high scanning speeds additionally, EBAM needs less or no build supports. However, the SLM whilst needing more supports in the build can manufacture better dimensional and face finish qualities.

2.2 Surface form metrology

For AM or other mechanical manufacturing fields, the inspection of machining quality is an important feedback data input for the manufacturing precision. Therefore, the form measurement of the surface is important to the manufacturing process. This section reviews the classification of 3D optical technologies and some other major 3D optical technologies in subsection 2.2.1. Subsection 2.2.2 introduces some coding algorithms. Subsection 2.2.3-2.2.5 according to different roughness surfaces, form measurement methods are introduced. Moreover, subsection 2.2.6 includes some machine learning algorithms in 3D optical metrology.

2.2.1 Classification of 3D measurement technology

According to the different lighting modes, the current optical 3D measurement technologies can be divided into two categories: passive measurement and active measurement. Figure 2.2 is the classification diagram of optical 3D measurement technology.

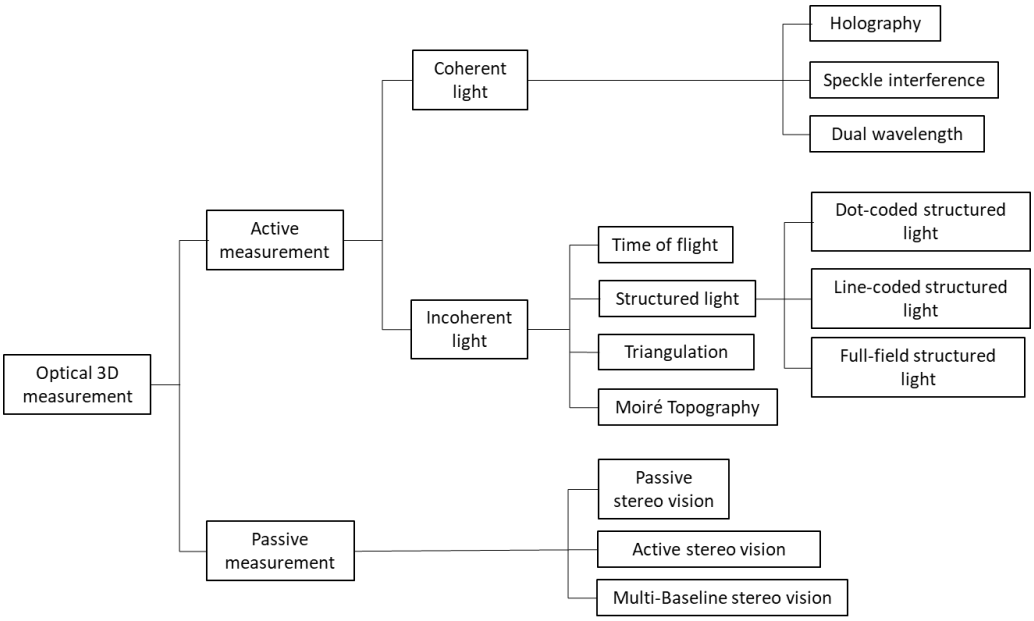

Figure 2. 2 Classification diagram of optical three-dimensional measurement technology

Passive 3D measurement technology uses one or more cameras to take a two-dimensional picture of the object without an active projecting light source. The depth information of the object is extracted from the images, and the 3D surface shape data is obtained. These methods are not suited for precision measurement because of the poor measurement accuracy and massive calculation. However, these methods have a wide range of applications in 3D target recognition, intelligent positioning, unmanned driving, and other fields. A typical passive 3D measurement technique is stereo vision.

Stereo Vision

Stereo Vision is one of the typical non-contact optical techniques in the field of machine vision [33]. Stereo Vision techniques can be roughly divided into passive Stereo Vision, active Stereo Vision and Multiple-Baseline Stereo [34][35]. Passive Stereo Vision is namely passive measurement, in which two or more cameras are used to take multiple images of the same object, and the triangular geometric relationship and parallax principle are used to reconstruct the 3D surface, as shown in Figure 2.3 [36]. Passive stereo vision needs to know the distance between the camera and the test objects. Therefore, this method requires the objects to be static or the image matching and construction of moving objects with motion compensation [37]. In addition, multi-camera employed in the system can improve measurement accuracy due to it the fact that the technique has a matching baseline. The basic measurement principle of active stereo vision is the same as passive stereo vision, but the active stereo vision technique uses the dynamic motion of the cameras and object for inspection. In these methods, 3D data can be reconstructed by multi angle images which are captured by the cameras. Because of multi-angle capture, much more detailed information of tested surface could be recorded, the reconstruction accuracy can be improved. Active

stereo vision system would be fixed on a robotic arm for inspection. Multiple-Baseline Stereo utilizes many cameras to take many images to match together to improve the accuracy of the 3D measurement results. This approach addresses the error from discontinuities because of multi-camera data capturing. However, Multi-images would increase the searching area for matching pixels, which will lead to false matching.

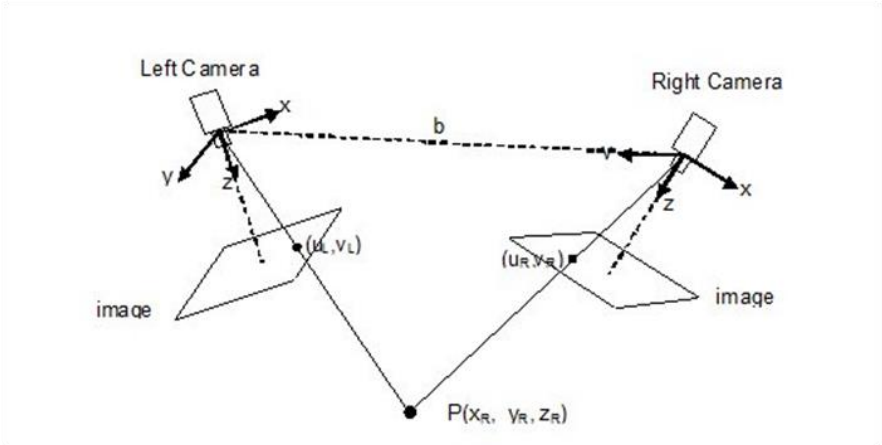

Figure 2. 3 The measurement principle of stereo vision technique [36]

In summary, stereo vision technology has high requirements in surface material, colour and background light intensity, which increases the computational complexity and it is difficult to deal with surfaces with occlusion and low texture. However, stereo vision technology still has some advantages for the measurement of large 3D shapes such as buildings, airplane bodies, auto piloting, etc. [38]. The current research deals with addressing image matching issues, false boundary issues, surface texture reflection issues, obstacles identification issues, etc. which improves the measurement accuracy of the stereo vision technique [39].

Compared with passive 3D methods, the active 3D measurement technology obtains the depth information of the inspected object by actively projecting the coded light

source and analysing the reflected light information to reconstruct 3D data. The main active 3D measurement methods are described as following.

Time of flight

Time-of-Flight (TOF) is one of the commercially used techniques[40], which is an image sensing technology that can construct object depth information. A single camera is used to measure the time delay of modulated light from an active emitter in the TOF system[41]. The measuring principle of TOF is that a single laser pulse is emitted from a transmitter to the measured surface, the pulse is reflected at the object and is captured by a receiving detector. By measuring the pulse round-trip flight time, according to the speed of light, the measurement system can calculate the distance between the object and the detector. Coupled with an additional scanning device and laser pulse on the entire surface scanning, the measurement system can obtain 3D shape data. Furthermore, a developed TOF method by measuring the phase shift between an emitted and a received signal has been investigated [42]. The signal that modulates the constant frequency phase information is recorded by the detector. The key component is a sensor that can measure the phase difference and distance information without scanning. The measurement range of this technique is from a few centimetres up to 50 meters. However, the major limitation of TOF is that the low resolution with millimetres level measurement and special sensors need to be designed to meet the requirements of recording two different types of information. Due to the low manufacture price and the enormous progress in TOF vision systems [43], nowadays 3D TOF cameras can be applied in many areas such as robotic, medical, industrial, automotive safety and multimedia applications [44].

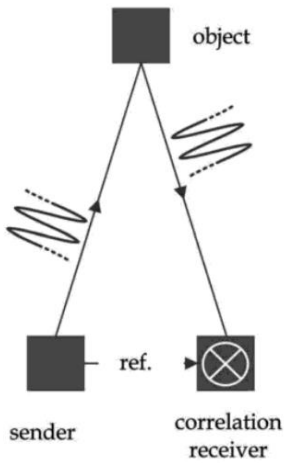

Figure 2. 4 TOF vision system[45]

Interferometry

Interferometry is a renowned non-contact optical method for measurement of optical surface with high axial resolution down to sub-nanometre levels. It takes advantage of the wave properties of light to analyse surface characteristics by separating source light into two independent paths and then recombining them to achieve interference, which is monitored by a digital camera. Different setups can be used, such as Fizeau interferometers (see Figure 2.5), Michelson interferometer, Mirau interferometer, Linnik interferometer etc., Many popular metrology techniques based on interferometry are built for form measurement [46], such as phase-shifting interferometers (PSI), white light interferometers (WLI), wavelength scanning interferometers (WSI), etc. [47]. Phase-shifting interferometers can be classified into two types: single wavelength interferometers and multiple wavelength interferometers. Single wavelength interferometers are ideal for measuring flat and spherical surfaces with sub-nanometre accuracy. However, it is very difficult to achieve the measurement when the test surface is aspheric or two steps due to the well-defined 2π phase ambiguity issue (as in AM surfaces). Multiple wavelength interferometers can be

utilized for specular surfaces with discontinuities up to few millimetres, and can achieve high vertical resolution up to sub-nanometre level. However, fast large-scale form measurement still has its limitation. Interferometers are widely used in astronomy [48], optics, engineering measurement, oceanography, seismology, spectral analysis, quantum physics experiments, remote sensing, radar and other precision measurement fields [47].

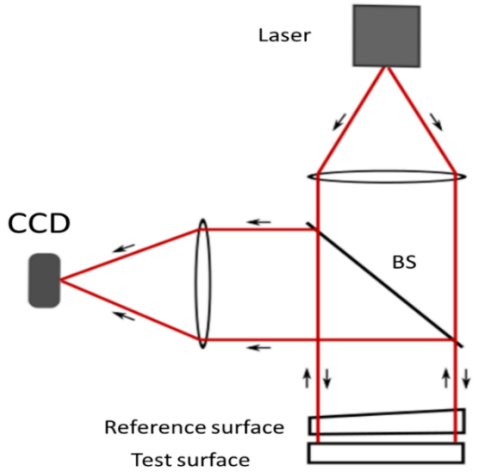

Figure 2. 5 Fizeau interferometer

Moiré Topography

The principle of basic Moiré topography is triangulation, in which fringes are projected on the surface through a projector, and the fringes are deformed by the target surface height [49]. The camera captures these deformed fringes through a reference grating from another angle, the overlapping Moiré fringes can be observed for post-processing as shown in Figure 2.6. The depth information of the object can be reconstructed by analysing the Moiré fringes [50]. Moiré topography has the following characteristics: the experimental equipment is simple, does not need a coherent light source; Suitable for measurement of larger and deeper objects; Low requirements for the measurement

environment [49]. The traditional Moiré topography mainly includes two methods: the shadow method [50] and the projection method [51][52]. In the shadow type, only one grating is needed for measurement, while in the projection type, the projection grating and the reference grating need to be separated from each other. The shaded Moiré method can directly observe the contour distribution on the surface of a target object, however, it is not suitable for measuring large objects because it is difficult to make large gratings. Compared with the shadow method, the projection method is more flexible. The projection method can use the small size reference grating to measure large objects. The measurement resolution of Moiré topography is higher than that of TOF (range see Figure 2.15), and the resolution can be greatly improved by the phase shift technique.

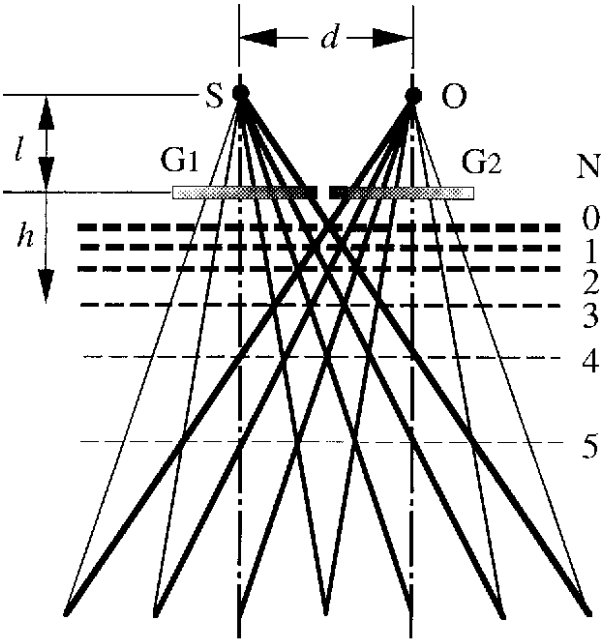

Figure 2. 6 Measurement principle of Moiré Topography [50]

Depth from defocus (DFD)

The basic measurement principle of DFD and depth from focus (DFF) are geometric triangulation. In each optical system with a lens, the object can be clearly captured by the cameras, when the objects are in the depth of field. This technique requires the use of defocus images, which means the target image surface must exist within the depth of field range. The blur of the image will increase when the distance of the object increases from the focus plane. During the measurement, two images with different defocus levels are captured. DFD is to determine the relative blur between two defocusing images, which means the geometry of a scene can be estimated by measuring the amount of blur in an image. According to the relative blur and fuzzy parameters of the optical system, depth information can be calculated from the blur of the images. One typical DFD technique is depth information restoration technique from a fully digital auto-focusing system [53] [54]. Another approach is the defocus depth measurement from fuzzy quantity analysis [55]. The former method is based on point spread function estimation which is estimated by using characteristic information of the image. After averaging the step responses of edge containing sub-images and subdivide the input image, the reconstruction accuracy can be improved. The latter method establishes the geometrical relationship between the size of the fuzzy circle and the imaging system parameters to determine the best focusing position. DFD relies on the texture features of the surface to calculate the relative blur. When the feature of the object surface is too simple or too complex, it will be difficult to obtain the relative blur correctly. The range of the resolution can be found in Figure 2.15.

Structured Light Technique

Structured light technique is an active triangulation technique that has been widely investigated [56]. The measurement process is that the coded light is projected to the

object surface by the projection equipment, and deformed structured light image on the object surface is recorded by the image sensor, then the 3D surface shape data of the object is retrieved from the recorded image by the appropriate method [57]. The structured light technique can be divided into dot-coded structured light, line-coded structured light and full-field structured light according to different light sources [58]. Dot-coded structured light method is a point-to-point scanning that is time-consuming [59]. Compared with the dot-coded method, the line-coded method has a faster scanning speed [60]. It has a problem for inspection of dark, transparent and specular surfaces due to surface characteristics limitations. However, the line-coded method has the advantages for large object 3D reconstruction. Full-field structured light method has high speed, high accuracy and a large field of view which can realize the whole field measurement quickly and accurately [61]. The grating projection technique is a typical method of full-field structured light. The key element of coded structured light techniques is the coding strategy which includes colour coding, binary coding, phase coding, etc. These encoding methods will be discussed in detail in section 2.2.2.

2.2.2 Encoding methods classification of structured light system

The full-field structured encoding light method has high effectiveness and high accuracy which has been developed in both academic institutions and commercial fields. Structured light techniques consist of a mechanical grating, LCD (liquid-crystal device) or digital projector light source to generate encoding patterns, and a camera will be gathering local information around this encoded point. After establishing the geometric relationship of the system and the corresponding matching relationship between light source and image, the depth of each point data can be determined. This

sub-section will mainly introduce coding methods including De Bruijn colour coding, binary coding, phase coding, etc.

De Bruijn Codifications

De Bruijn coding belongs to pseudo-random arrays theory [62]. The De Bruijn sequence has a one-dimensional window property, namely, a certain length of sub-sequence is unique in the total sequence [63]. In other words, for an n-element de Brujin sequence of window size m, that is, a cyclic sequence of length n×m, any sub-sequence of length m appears only once in the whole cycle [64][65]. Because of the unique property, as long as the attributes of the sub-sequence elements and the order are extracted, their position in the total sequence can be determined. Figure 2.7(a) [66] shows the coding pattern based on the De Bruijn sequence, which consists of 125 vertical fringes with eight different hue levels colour. The edges of fringes are located in each line by searching local maximum value. The value is determined by the function: $F = dR^2 + dG^2 + dB^2$, where d*R*, d*G*, and d*B* are the intensity gradients of the red, green, and blue channels on the current scan-line. This coding method only needs to project a single image which meets the demand of dynamic measurement. However, this is discrete coding with low lateral resolution, and the measurement results are easily affected by the colour and texture of the measured surface. Figure 2.7 (b) (c) (d) are other similar methods by De Bruijn coding.

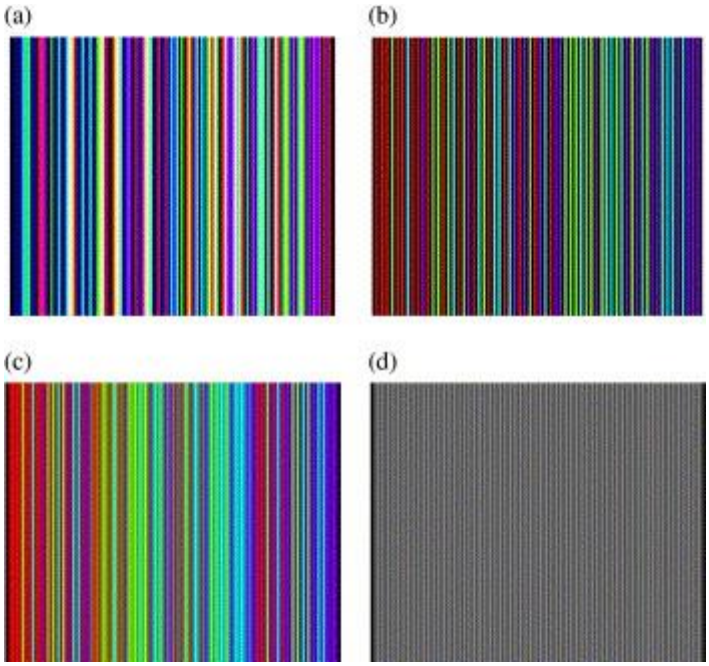

Figure 2. 7 Example of the De Bruijn encoding [66] (a) Fringe-pattern by Zhang et al. (b) multi-slit pattern proposed by Monks et al. (c) Hybrid pattern in the RGB. (d) Hybrid pattern intensity profile.

Binary structured Codifications

Binary coding is one of the well-known intensity-based methods that project multiple binary-coded patterns [67]. Since only two illumination levels (black-0 and white-1) are used, the sequence of 0's and 1's can be captured by the camera and with the decoding from the corresponding pattern on the projector. Figure 2.8 shows the representative binary coding methods. This coding method uses binary bits to represent 8 sequential integer numbers as shown in figure 2.8(a). If the left three patterns are projected sequentially at times t1, t2, and t3, the captured binary image can be decoded as the binary sequence as shown on the right. 3D reconstruction can be obtained by the determined code word for each camera pixel. In this case, it is less effective to noise for code word identification. However, the vertical resolution of this method is relatively low because the projected images are always larger than the

sensor's pixel. Therefore, it needs more patterns to increase resolution, which slows down the measurement speed. Figure 2.8(b) shows another binary coding method (Gray coding). Gray coding method allows changing status of one sequence patterns from 0 to 1 or from 1 to 0 at a given projector pixel. Compared with the simple binary coding method, Gary coding method has better measurement resolution, Gray code method requires less image acquisition and has relatively high measurement efficiency. A multi-level gray coding method has been proposed to reduce the number of patterns in order to improve the measurement speed [68]. Though the measurement speed can be improved, this method is sensitive to noise from the camera and image defocus. The 343478 method requires a small number of images to be collected and has a relatively high measurement efficiency, but it needs to rely on the threshold method to segment the image, and the measurement results are easily affected by the texture, colour, and uneven illumination of the measured surface.

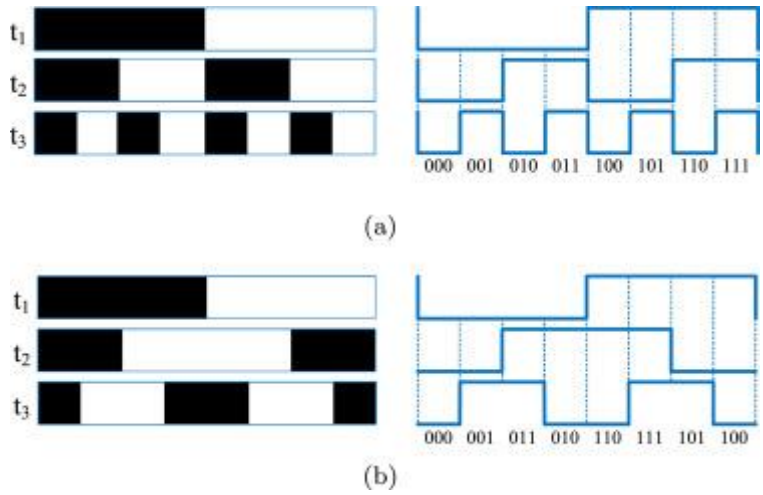

Figure 2. 8 Representative binary coding methods. (a) Simple binary coding; (b) Gray coding.[69]

Phase Codifications

Among all 3D structured light techniques, using phase information instead of intensity can get higher spatial and/or temporal resolutions [10-100 μm]. It has advantages of robustness to noise, robustness to surface reflectivity variations. One classic coding method is that sinusoidal fringe patterns are projected to the object surface, and the phase-shifting algorithm is used to calculate the phase. The measurement resolution can reach up to 0.1% of the fringe pitch. In order to obtain an absolute phase map, some unwrapping algorithms need to be involved which will be introduced in section 2.3. The advantages of this method are high resolution and simple decoding but the method needs to project more patterns which reduces measurement efficiency. Figure 2.9 shows the sinusoidal fringes and the corresponding profile images.

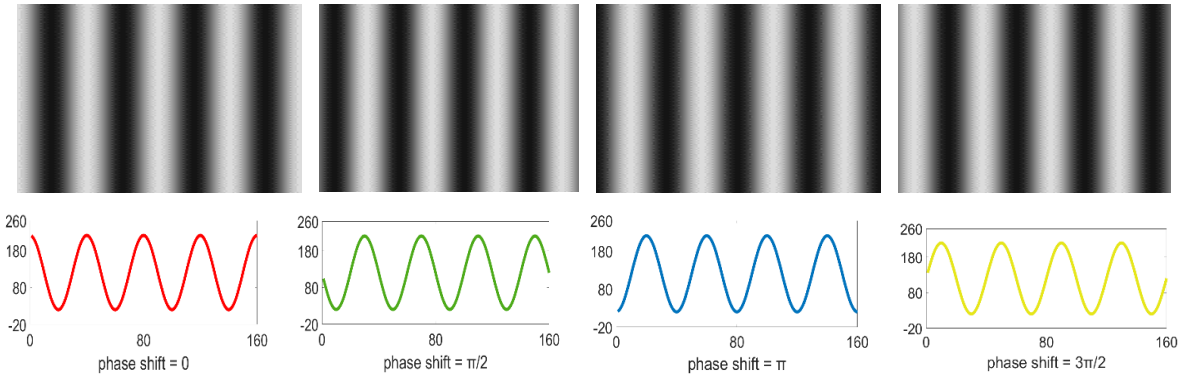

Figure 2. 9 Sinusoidal fringe patterns and the profiles

Another two similar methods are triangular phase codification and trapezoidal phase codification. Triangular [70] phase codification encodes the use of triangular patterns which refers to the shape a plot of the cross-section of the pattern as shown in Figure 2.10. The triangular shape between the two images can be recovered by calculating the intensity ratio [71]. The wrapped intensity ratio distribution is obtained by removing the triangular shapes. After the unwrapped calculation, this can be used with the intensity ratio for height conversion to retrieve 3D data. Trapezoidal [72] phase

codification is similar to the triangular phase algorithm, the example trapezoidal structures and the profile images as shown in Figure 2.11 [73].

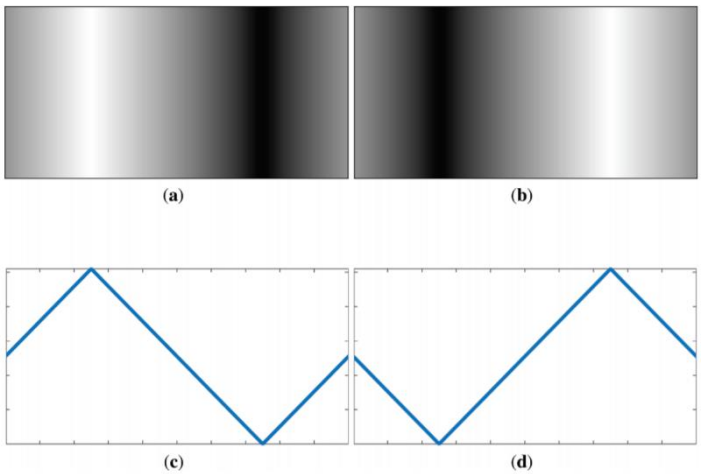

Figure 2. 10 Triangular patterns and the plot of the cross section

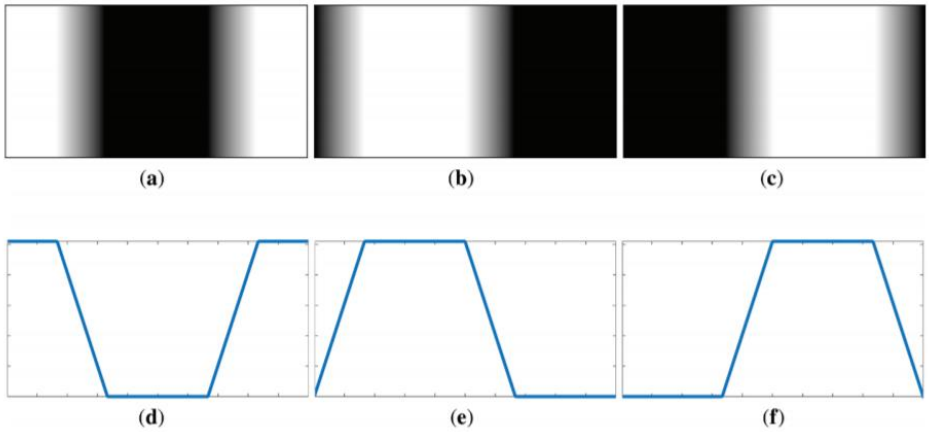

Figure 2. 11 Trapezoidal patterns and the plot of the cross section [73]

2.2.3 Structured light system for rough surface measurement

The above subsection reviewed the classification of 3D optical measurements and the classification of structured light encoding techniques. Therefore, it is known that structured light technology is an active optical measurement, for different precision, surface reflective characteristics and environment requirements, users must choose the appropriate measurement method and encoding methods to build different

structured light system. Most structured light projection techniques can inspect rough surfaces, excluding black surfaces, due to the diffuse reflection of the surface.

The following sub-section will give an overview of the 3D measurement of rough surface which includes the system calibration techniques and review several developed structured light measurement methods.

Calibration methods

In order to obtain a traceable measurement of the 3D shape, a significant step for an optical imaging system is to find the geometrical relationship between the camera and the projector, as well as the relationship between the world coordinates and the camera image coordinates, more commonly known as system calibration, which determines the measurement precision and repeatability. System calibration can be divided into camera calibration and geometric calibration. Existing geometric calibration methods for 3D inspection systems can be categorized into model based [74], polynomial [75], and least squares [76].

The Model-based method [77] is based on a geometrical model. The geometrical relationship between the camera and the projector is established by triangulation theory. After calculating system parameters, 3D data can be obtained by the phase map. The Least-squares method seeks to find the nonlinear relationship between the phase map and the 3D data. In this case, the calibration procedure becomes more flexible and easier, because system geometric parameters do not need to be calculated directly. For example, Zhang[78] proposed a method using a white plate with discrete certified markers on the surface to calibrate horizontal and vertical parameters, a one-to-one mapping between camera points and projector points is then

established, which is implemented in practical environments without any precise translating stage. The polynomial method seeks to express the relationship between the phase and depth coordinates by a polynomial relation, and the relation fits the relative position between the camera and the projector. Since the phase and depth relationship of the fringe projection system is close to linear, but due to nonlinear effects, lens distortion and other factors, more than three polynomials are needed to ensure the measurement repeatability. Windecker [79]proposed a calibration method to determine the sensitivity field by using a low-order polynomial, which builds up the transfer function of the phase and the height. Sutton [80] used a third-order polynomial to calculate phase and height information pixel-by-pixel by a phase–height transformation.

Other developed methods

There are still some other methods used to improve accuracy, speed and measurement stability. Zhang [13] proposed a method based on a phase-shifting algorithm to acquire 3D absolute coordinates in order to improve measurement speed. Huang et al[81], used a typically single colour pattern because different colour channels can code different phase information. In this case, the shape acquisition results are affected by the variations of the surface colour. Reich[82] proposed a 3D measurement method for complex objects by using photogrammetry and fringe projection. The principle of the fringe projection technique is shown in Figure 2.12. Quan[83] proposed the relationship between phase and the depth by using a reference plane to move to a known distance, Guan[84] used a composite structured light pattern to realize real-time 3D shape measurement.

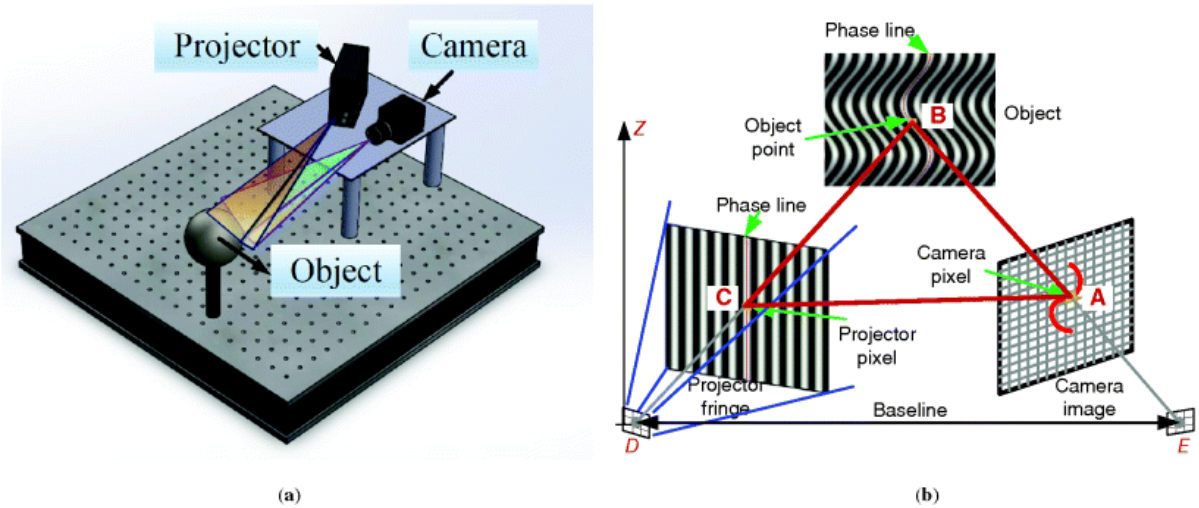

Figure 2. 12 The principle of fringe projection technique

After system calibration, 3D data of the rough surfaces can be calculated by decoding phase information. Although many researchers have made some achievements in this field, there are still some problems to be solved, such as practical applications in some industrial fields, real-time 3D detection, colour textured surface detection, 3D measurement of transparent and highly reflective objects, etc.

2.2.4 Structured light system for shiny surface measurement

Structured light systems have a wide range of applications. However, there are still some problems to be solved, such as highly reflective object inspection. In industry, there are many metal parts that need to be machined and inspected, and the phenomenon of light saturation will appear when traditional structured light technology is used. Therefore, this kind of high dynamic range measurement problem needs to be solved.

The intensity saturation is problematic whenever optical inspection technology especially structured light is used for measuring shiny surfaces, such as metal surfaces or ceramic surfaces. Some researchers have conducted a series of studies

on this issue. The solutions can be grouped into three categories. The first category is the multi-exposure method which is to obtain less incoming light by adjusting the exposure time of the camera, the saturated intensity of the image is neutralized. Zhang [85] presented a method encompassing a sequence of fringe images with different exposures followed by a “selection” of the brightest but unsaturated corresponding pixel to produce the final fringe pattern. This method requires multiple image capture sets, which consumes time and slows down the measurement process. Ekstrand [86] studied an approach to generate sinusoidal fringe patterns by properly defocusing binary images with an automatically adjusting exposure time. This technique reduces the measurement time and improves the intelligence of the inspection system. But the single exposure time does not fit a large range of reflective surface measurement. Suresh [87] proposed an improved multi-exposure method which, after projecting binary sinusoidal patterns, capturing two images during the projector’s bright period and dark period, using different exposure times. This approach increased measurement speed but still needed additional fringe patterns to obtain absolute phase. This set of methods relies on changing exposure time to obtain unsaturated images in order to solve the problem of achieving high dynamic range measurement. The second category is to eliminate the reflective effect, which is essentially equipment-based techniques facilitated by adjusting parameters or using special devices. Salahieh[88] presented a multi-polarisation fringe projection imaging technique to eliminate saturated points and combine the results of different exposures to measure both dark and shiny areas. This method requires the application of special polarizing cameras, as well as the addition of a polarizing film in front of the projector lens, which increases the hardware cost. Liang [89] investigated a polarized short wavelength to solve low fringe contrast problem and it was applied to measure 3D

surface shapes of translucent objects. It uses the short wave polarization technique to measure the transparent object, but does not solve the problem of measuring the reflective object. Jiang [90] presented a novel 3D scanning technique to generate a synthetic fringe image with different illumination intensity captured with different camera exposure times to solve the saturation problem. This technique used the dual parameters of adjusting the projection brightness and camera exposure to solve the problem of measuring the different reflectance of the surface, but the methods still needed to shoot multiple sets of images without realizing automatic and intelligent detection. The third category is based on RGB colour channels to separate saturated pixels from images. Klinker [91] utilized the different performance of pixels in RGB colour space to remove the highly reflective areas. However, this method is sensitive to noise. Shen [92] proposed a simple separation method, which used specular free images to estimate chromaticity of diffuse reflection. It increased measurement speed but reduced the measurement accuracy.

The above methods provide a series of solutions to the problem of reflective surface measurement, and the problem of saturation in the detection of metal surfaces and reflective surfaces by using structured light measurement technology has been effectively investigated.

2.2.5 Structured light system for high reflective surface measurement

For structured light techniques, another challenge is specular surface inspection. Due to the different measurement principles of specular surfaces and diffused surfaces, different inspection techniques are used in 3D measurement. Phase measuring deflectometry (PMD) is method one of the most popular methods for specular surface inspection.

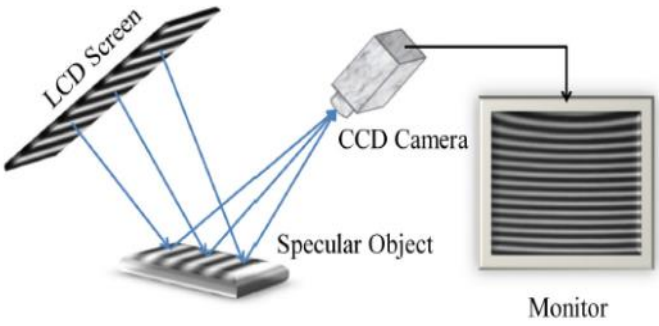

Figure 2. 13 Schematic diagram of deflectometry measurement principle

Phase measuring deflectometry (PMD) or fringe reflection deflectometry (FRD) has been widely studied to measure specular freeform surfaces [93][94]because of the advantages of non-contact operation, full-field measurement, fast acquisition, high precision and automatic data processing [95][96]. PMD has been applied to measure aspheric mirrors and dynamic specular surfaces and to detect subsurface cracking [97], from a micro-size to a large specular surface [98][99]. Compared with the fringe projection technique, the principle of PMD is different, the techniuque needs to display straight sinusoidal fringe patterns on a screen or to project a structured pattern onto ground glass as shown in Figure 2.13. From a different viewpoint, fringe patterns reflected by a measured surface appear deformed with regarding to the slope variation of the specular surface and the modulated fringe patterns can be captured by an imaging device, such as a charge-coupled device (CCD) camera. Phase information in the deformed fringe patterns is demodulated to obtain the slope of the measured specular surface and the 3D shape of the tested surface can then be reconstructed by integrating the gradients[100]. Due to the ambiguity issue of the measurement, another set of known parameters should be provided to complete the measurement. Namely, the absolute height measurement can be achieved by another adding camera,

that is, two or more cameras with a display equipment [101][102], or by moving the display screen with one single camera[103], or by using a single camera with a dual display device[104]. Figure 2.14 (a) shows monocular deflectometry with a shifted screen. Based on the geometric relationship between the LCD and the CCD, the relative slope of the tested surface can be achieved. An LCD is fixed on the transfer stage, after moving by a known distance, the form of the test specular surface can be calculated. Figure 2.14 (b) shows the stereo deflectometry technique. Two cameras capture deformed fringes via specular reflection in different views. After the two-camera calibration, the corresponding pixels are calibrated in both cameras, the slope of test surface can be determined. The measurement principle of Figure 2.14(c) is similar with figure (a), which use two LCDs to replace moving LCD. In this case, the measurement efficiency can be improved by eliminating restrictions on the moving stage.

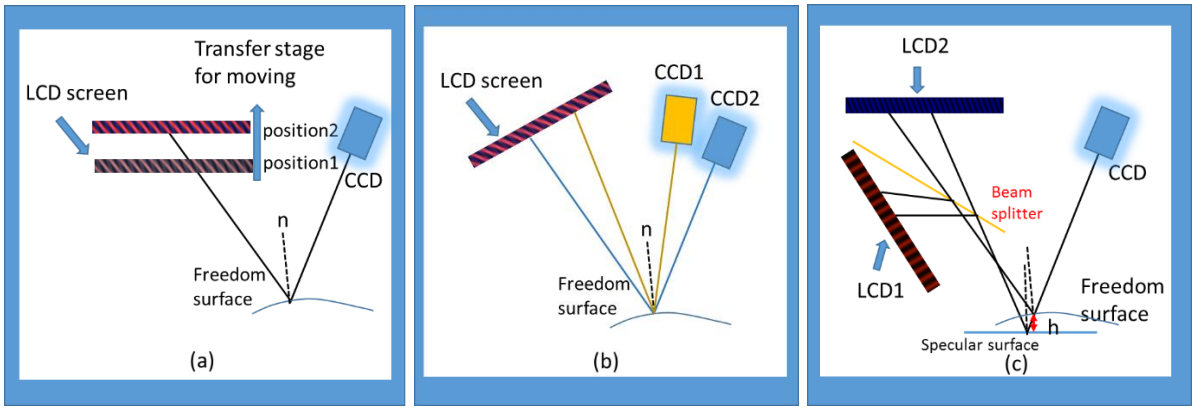

Figure 2. 14 Some types of deflectometry system

2.2.6 Machine learning applications in structured light surface metrology

The application of intelligent sensing is increasingly extensive owing to the development of machine learning algorithms. The concepts of smart city, smart factory, smart home and other reasonings are put forward to further accelerate the process of

intelligence systems. In terms of the present research, machine learning technology has the ability to combine with fringe projection technology to provide a new solution to the problems existing in fringe projection technology. Feng [105] proposed a single-frame grating fringe analysis method based on a deep learning framework. The idea is to use only one fringe image as input and use the deep neural network to simulate the phase demodulation process of the time domain phase shift method. By constructing two convolutional neural networks (CNNs), phase information is obtained from fringe information. However, this method can only be used to measure non-complex surfaces. Feng's group also developed a deep learning algorithm to solve high dynamic range measurement in a recent paper, which improved the dynamic range of three-step phase-shifting without any additional projected images. They achieved depth precision of 0.1 mm [106], which in the present case is insufficient for the proposed system. Xiang[107] proposed a new phase analyse method by SVM to reduce fringes number, which has the same low precision issues in real measurement. Spoorthi G.E.et al [108] proposed a phase-based neural network (PhaseNet) to achieve two-dimensional spatial phase unwrapping. The input of this method was the wrapped phase map. By constructing the neural network, the phase unwrapping order and the unwrapped phase map can be obtained. But the data for this method comes from simulation, this requires more in-depth calculation and optimization when dealing with real complex geometry surfaces. Yan et al. [109] proposed a method to reduce noise of the fringe pattern by using deep learning algorithms. This method constructed a deep convolutional neural network with 20 layers where the input data is a noisy fringe image. After a series of CNN processing, the output data is the noise suppressed fringe image. The training method of the network is supervised training, and the training label used is a simulated raster image with no noise. However, this

method uses simulation to generate the training data. There are differences between the actual raster image and the simulated raster image, which will put higher requirements on the performance of the algorithm. Therefore, a smart fringe projection technology that can take advantage of machine learning and also meet precise measurements requirements to measure complex surfaces needs to be developed.

2.3 Phase analysis and algorithms

Some optical measurement techniques were reviewed in section 2.2. The development of structured light measurement techniques for rough surface measurement, shiny surface measurement, and specular surface measurement was discussed. During the measurement, the sinusoidal fringes are projected onto the sample surface, the deformed fringes carry the surface shape information. The phase analysis algorithms determine the measurement range and accuracy. Different phase analysis algorithms are suitable for different measurement surfaces and measurement requirements. In other words, phase calculation or phase analysis is significant in measurement processing. In this section, the author will discuss the phase-shifting algorithms used to obtain wrapped phase and the optimum frequency selection algorithm to determine the absolute phase values.

2.3.1 Phase calculation

Over the years, numerous phase calculation methods have been developed, and here the most popular ones will be considered. There are many classic phase algorithms such as Fourier Transform (FT) [110], Windowed Fourier Transform (WFT) [111][112][113]and Wavelet Transform (WT) [114], which are the spatial domain algorithms to calculate from a single deformed fringe. The integrated new phase calculation algorithms such as multiscale windowed Fourier transform [115], Hilbert

transform [116][117] , DC signal elimination [118][119] , or machine learning methods were investigated by research other institutions[120] [121].

During fringe projection measurement, sinusoidal fringes are generated from a PC and projected to the sample surface. The ideal sinusoidal fringe image can be generated as,

$$I(x,y)=A(x,y)+B(x,y)\cos(\Phi), \qquad 2.1$$

where $I(x,y)$ is the projected intensity, $A(x,y)$ is the average intensity relating to the pattern brightness and background illumination, $B(x,y)$ is the intensity modulation, Φ is the phase to be solved for. Theoretically, based on Equation 2.1, it is hard to retrieve the phase value. It can however be rewritten by the Fourier transform profilometry (FTP) method as the following, as investigated by Takeda in 1983 [122].

$$I(x,y) = A(x,y) + 0.5 \times B(x,y)[e^{j\Phi(x,y)} + e^{-j\Phi(x,y)}] \qquad 2.2$$

where $e^{j\Phi(x,y)}$ and $e^{-j\Phi(x,y)}$ are conjugate relationship. Then Equation 2.3 can remove the conjugate and modulation B(x, y),

$$I'(x,y) = 0.5 \times B(x,y)e^{j\Phi(x,y)} \qquad 2.3$$

The wrapped phase can be written by following equation,

$$W(\phi) = -\arctan(\frac{I(I'(x,y)}{R(I'(x,y)}) \qquad 2.4$$

Where I(I') and R(I') represent the imaginary information and the real part. Therefore, a wrapped phase can be retrieved as the single fringe pattern, which is applicable for moving objects. However, this method is suitable for objects with simple texture, smooth surface and low fringe noise levels.

In order to obtain more accurate wrapped phase information, another wrapped phase algorithm has been extensively investigated over the years is highlighted. The phase-shifting algorithm is to obtain phase information by deformed fringes with shifting phase, which can then calculate phase pixel by pixel [123]. The straightforward approach is to generate a series of sinusoidal fringe patterns with phase shifting. The analysis was developed from phase-shifting Interferometry (PSI) introduced in the 1980s [124], also known as phase measurement profilometry (PMP). In this thesis, the author mainly utilizes sinusoidal fringes as the sample patterns and uses a phase-shifting algorithm to obtain the wrapped phase.

In the present case, the sinusoidal fringe patterns are captured by a CCD camera, which are utilised to calculate the intensity values as illustrated in Equation 2.5. The sinusoidal fringe patterns are shown in Figure 2.15.

$$I_i(x,y) = I_0(x,y) + M_d \cos\left(\frac{2\pi x}{P_0} + \delta_i\right) \qquad 2.5$$

Where i indicates the ith image, I_i is the captured fringe pattern intensity, I_0 is the background intensity, M_d is the modulation of the fringe patterns, P_0 is the period of the projected fringe pattern, δ_i is phase shifting which is represented as follows:

$$\delta_i = \frac{i-1}{N} 2\pi, i = 1,\ldots,N \qquad 2.6$$

Where N is the number of shifting steps.

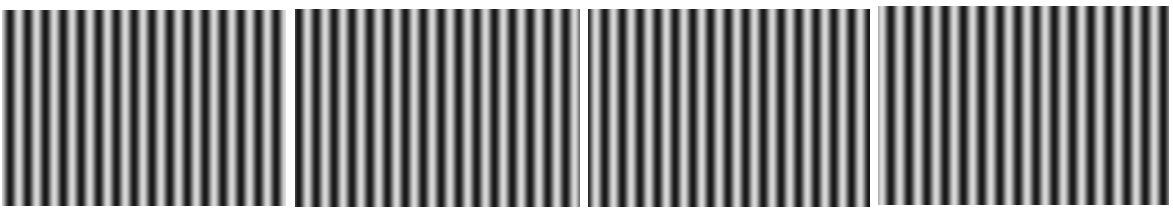

(a) (b) (c) (d)

Figure 2. 15 Sinusoidal fringe patterns after phase shifting (a) i=1;(b)i=2;(c)i=3;(d)i=4

Therefore, a wrapped phase (as shown in Figure 2.16(a)) can be represented by the following equation:

$$W(\phi) = -\arctan\left(\frac{\sum_{i=1}^{N} I_i(x,y)\sin(\delta_i)}{\sum_{i=1}^{N} I_i(x,y)\cos(\delta_i)}\right) \qquad 2.7$$

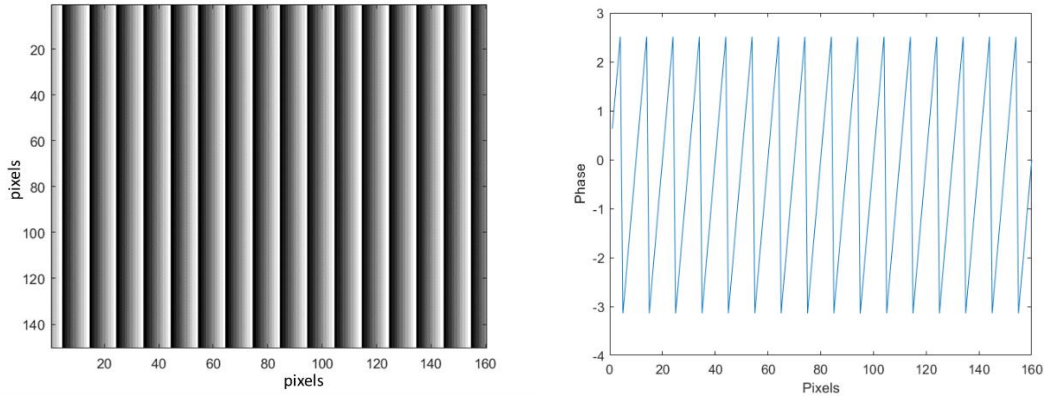

(a) (b)

Figure 2. 16 Wrapped phase map by phase-shifting algorithm (a)wrapped phase map (b) the profile image of the wrapped phase that crosses line 70

The phase-shifting algorithm can calculate wrapped phase more accurately compared with single-shot phase algorithms. When increasing the frames, the measurement results have smaller phase errors which are caused by nonlinear effects [125]. Therefore, phase-shifting algorithms have been extensively employed in surface metrology because of high calculation speed, high accuracy, high resolution, and good robustness.

2.3.2 Phase unwrapping algorithms

The obtained wrapped phase map distributes within [$-\pi$,$+\pi$) with a 2π modus as shown in figure 2.16(b). The process of changing this limit of [$-\pi$, $+\pi$) to obtain an unwrapped phase map from the wrapped phase is called phase unwrapping as shown in Figure 2.17. The unwrapped phase data can be obtained by using two main methods, spatial phase unwrapping methods and temporal phase unwrapping methods [126][127].

Spatial phase unwrapping is a method which is compares the wrapped phase at the neighbour pixels to determine the fringe orders in space [128]. For the ideal wrapped phase map, the procedure of phase unwrapping is simple and path dependent. This algorithm requires the measured surface to be spatially continuous and simple in shape However, in real measurement, hiding/shadows, bad fringe modulation, uneven intensity, fringe discontinuities and so on are quite common problems. Consequently it is difficult to get good unwrapped phase results with the above problems, especially for measuring complex surfaces. On the other hand, the phase in the author's fringe projection system and deflectometry system needs to use absolute phase, while spatial phase unwrapping algorithm only can obtain relative phase since it establishes the relation between neighbouring pixels, which lacks an absolute initial point.

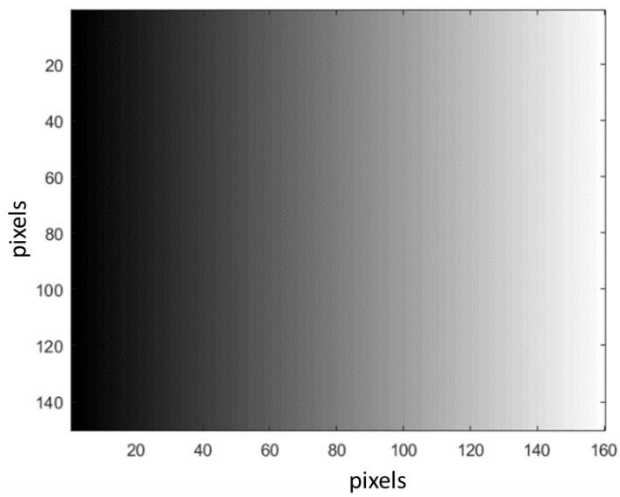

Figure 2. 17 Unwrapped phase by optimum frequency selection phase unwrapping algorithm

In some industrial products such as building surfaces by AM, the shape of the surface has features with complex, discontinuous, large gradients, shadows, and poor contrast. Therefore, it is particularly important to find a phase unwrapping algorithm to solve these problems. Temporal phase unwrapping methods calculate the sinusoidal

fringe patterns with different fringe pitches to determine fringe orders pixel by pixel along the time axis, which can solve the problems of fringe discontinuity, shadows, and large gradient, etc. Some typical temporal phase unwrapping methods have been developed for several years. Huntley, Saldner [129] proposed a one-dimensional unwrapping method that could be applied in an important subclass of interferometry, and constrained phase errors in the high-noise region [130]. Based on their previous work, they then proposed an exponential phase unwrapping algorithm [131] and reversed exponential phase unwrapping algorithm [132]. In this thesis, a temporal phase unwrapping method “the optimum frequency selection heterodyne phase unwrapping algorithm” is employed to obtain the absolute phase data [133][134][135].

The principle of the heterodyne phase unwrapping algorithm is to obtain phase Φ from two different frequency phase ϕ_1 and ϕ_2 over the field of view shown in as Figure 2.18 [**Error! Bookmark not defined.**].

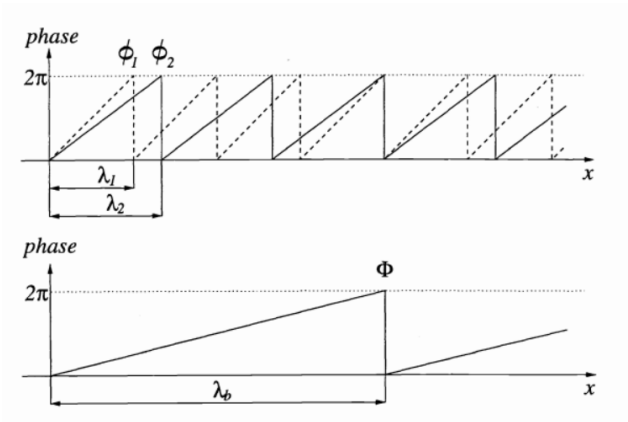

Figure 2. 18 The principle of heterodyne phase unwrapping [147]

As the examples showing here, the wavelength λ_1 and the wavelength λ_2 are used to calculate the superposition wavelength λ_b. The superposition wavelength can be

represented as Equation 2.8. The relationship between the two wavelength and the corresponding absolute phase is represented as in Equation 2.9.

$$\frac{1}{\lambda_b} = \frac{1}{\lambda_1} - \frac{1}{\lambda_2} \qquad 2.8$$

$$\lambda_1 \Phi_1 = \lambda_2 \Phi_2 \qquad 2.9$$

Therefore, the unwrapped phase Φ can be obtained by Equation 2.10

$$\Phi_1 = \phi_1 + 2\pi O_1 \qquad 2.10$$

The order of $\phi_1(x)$ can be represented as shown in Equation 2.11,

$$O_1(x) = Round\left(\frac{\Phi_1 - \phi_1(x)}{2\pi}\right) \qquad 2.11$$

where $O_1(x)$ is the order of phase $\phi_1(x)$ as shown in Figure 2.19.

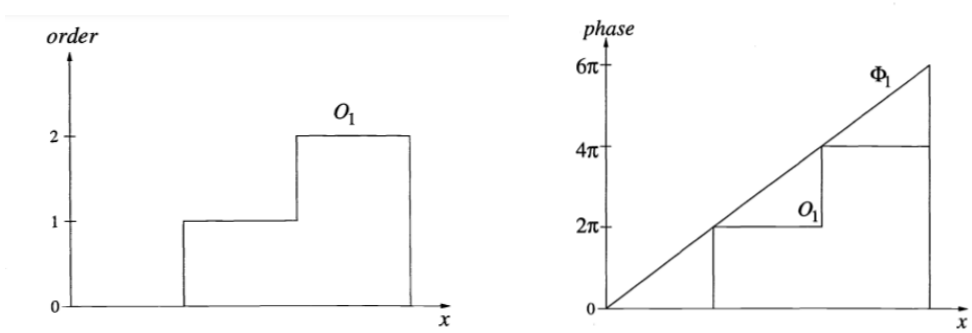

Figure 2. 19 Fringe order $O_1(x)$ and unwrapped phase $\Phi_1(x)$

The initial phase function $\phi_2(x)$ can be unwrapped similarly.

Based on the general heterodyne algorithm, Towers CE [136] and Zhang [137] proposed an optimum frequency selection phase unwrapping algorithm to determine

fringe order for obtaining the absolute phase map. Sets of sequential sinusoidal fringe patterns are projected onto tested surface, the number of fringes is defined by the following equation:

$$N_{fi} = N_{f0} - \left(N_{f0}\right)^{(i-1)/(n-1)}, i = 1,2,\ldots,n-1, \qquad 2.12$$

where N_{f0} is the maximum number of fringes which is determined by the actual requirements and the equipment (pixels of projector), N_{fi} is the number of fringes in the ith fringe set, and n is the frequency number. In this thesis, n is three, the number of fringes can be represented as Equation 2.13.

$$\begin{cases} N_{f0} = N_{f0} \\ N_{f1} = N_{f0} - 1 \\ N_{f2} = N_{f0} - \sqrt{N_{f0}} \end{cases} \qquad 2.13$$

For example, the maximum number of fringes is 100, and therefore N_{f1} is 99 and N_{f2} is 90. This approach resolves fringe order ambiguity as the beat obtained between N_{f0} and N_{f1} is a single fringe over the full field of view.

2.4 Other inspection methods in additive manufacture

The UK AM special interest group (SIG) reported the challenges and limitations of AM. One of the key factors to impact manufacturing quality is limited control, monitoring of processes and metrology of post-process[138]. In this section, other in-situ inspection techniques are reviewed and post process metrology techniques are introduced.

2.4.1 In-process inspection techniques

Many researchers and research institutes have investigated a number of metrology techniques for in-situ AM inspection which can improve manufacturing quality. Some

of these metrology techniques also are employed in commercial applications. These in-situ techniques can be divided into three categories. First, one is 2D images–based inspection techniques. This is the most simple and effective method to achieve in-situ inspection during the manufacturing. Arcam EBM® applies optical cameras to detect porosity. The AM machine manufacturer DEMCON manufactured AM machine and added cameras for testing melt pool. Berumen et al.[139] inspected pores and balling by capturing 2D images with an in-line camera . The camera can detect the scratches, position deviation and other problems through monitoring of the powder bed and surface in process, but it cannot realize the measurement of depth and 3D data. The second in-situ method is thermal camera inspection. This method mainly uses a thermal imager (IR camera) to detect the surface temperature in process, and can detect the surface form changes caused by manufacturing temperature changes. IR cameras were utilised by Krauss et al.[140] to investigate the limits of detecting pores and other irregularities caused by insufficient heat dissipation during L-PBF processing. Hu et al. employed a near-infrared (NIR) camera in combination with a powder delivery rate sensor for pool monitoring during powder DED (Directed Energy Deposition) processing. A two-wavelength imaging pyrometer is used to test melt pool temperature, which is employed in an AM machine manufactured by Stratonics [141]. These thermal inspection methods, while monitoring the processing temperature, can show the influence of temperature on the manufacturing quality and can feed back information to the AM control system. The third method is multi-sensor inspection. In this case, a multi-sensor is applied to evaluate in process surfaces. Dual-colour pyrometer and three high-speed CCD cameras are used to monitor melt pool and build height, which are used in a commercial AM machine [4]. Thermocouples and high-speed cameras are employed to monitor manufacturing process in the PrintRite3D® machine[142].

Inline coherent imaging and white-light interferometer [143] are used for depth inspection and Zhang et al.[144] inspected the powder bed of a Laser Powder Bed Fusion (L-PBF) system over a relatively small 28 x15 mm inspection area with 0.47 μm repeatability by using a fringe projection system. All of these multi sensor systems can realize form inspection by adding more sensors however the majority are uncalibrated. By measuring the 3D data, more reliable feedback information is provided for AM machine control, both in terms of detection accuracy and information integrity.

2.4.2 Post-process inspection techniques

Another challenge of AM is post-process metrology, which includes the measurement of surface form, texture and internal features [145]. After manufacturing is completed, the accuracy and quality of manufacturing can be evaluated by testing and analysing the printed parts. First of all, the machined surface form needs to be measured. At present, one of the general methods is contact measurement, such as coordinate measuring machines (CMM), etc., which can obtain traceable surface depth with high precision. However, the measurement time is slow because of point-by-point measurement and the surface can be damaged by the probe additionally due to the re-entrant nature of the AM surfaces there are issues with the probe filtering the measurement. Second inspection method for surface form is optical method. The appropriate measurement method can be selected according to the size of the measured surface and the measurement requirements. The specific method can be referred to sub-section 2.2.1. Such as interferometry [146], which is optimized surface measurement by using coherence scanning interferometry. Bartllett, Croom and Li [147][148][149][150] investigated the relationship between the residual stresses and

printed surface shape and obtained reasonable residual stresses results by using stereo-vision method. Southon N et al.[151] developed a system incorporating fringe projection to monitor the powder bed of a polyamide-12 in a laser sintering machine and demonstrated the ability to identify a number of defects, the system is suitable for dynamic process control. Figure 2.20 shows the measurement accuracy that can be achieved by each optical method Work by Townsend et al [121] showed that Focus Variation techniques are the most widely employed for surface form assessment post process. A third technique that can be used to measure surface form is X-ray computed tomography (CT), which is also suitable for texture and internal structure inspection. Tammas-Walliams et al. [152] used X-ray computed tomography (XCT) to scan printed parts to get 3D information of the size, volume fraction and spatial distribution of the internal pores, when building Ti-6AL-4V structures by electron beam PBF. Zanini [153] measured the external thread measurement of a dental implant printed by laser sintering of Ti6Al4V. In such cases, when the printed surface was measured by XCT, it overcomes the limitations of AM parts with small features, large form errors and complex surface texture.

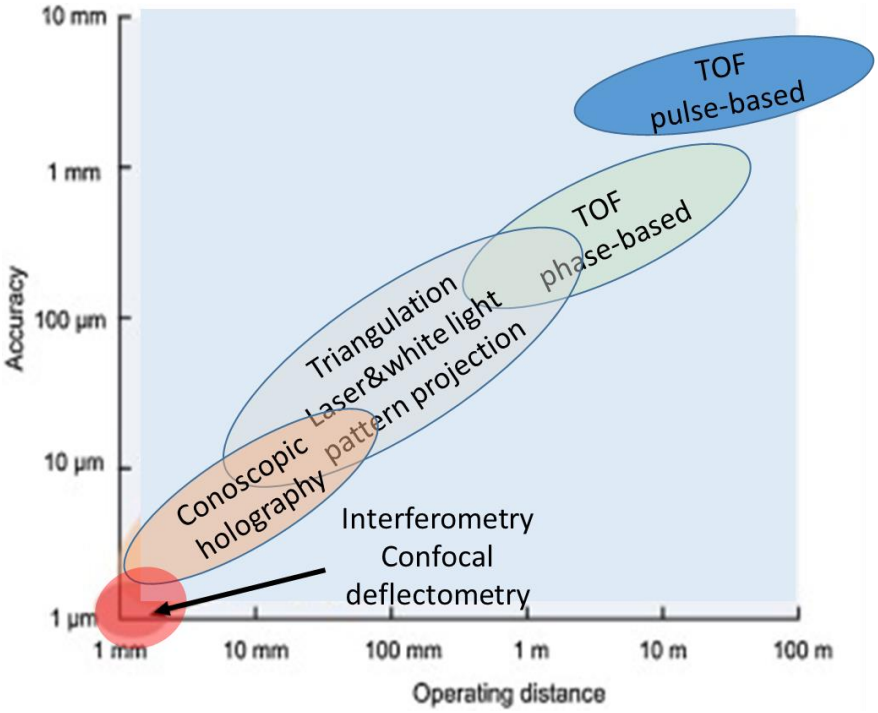

Figure 2. 20 Classification of some optical methods according to their accuracy and working distance [154]

Post-process metrology also including texture inspection, because printed AM surfaces are often highly complex and irregular [155]. Texture measurements can provide a significant feedback that compared with different measurement technologies. The typical equipment is scanning technique (coherence scanning interferometer [156] and XCT system) and optical microscope (confocal microscope and focus variation microscope), which can obtain high resolution texture images [1].

Another post-process metrology challenge is internal inspection. Internal defect detection is an essential evaluation for manufacturing quality. Internal defects such as holes and scratches can affect the component structure, stress and stability. At present, XCT is the only available non-destructively technique which can inspect both material and dimensional quality of internal structures. The working principle of XCT is that an X-ray that only partially decays when it passes through an object. Therefore,

according to this property, radiographic images taken from multiple angles around an axis of rotation can be used to reconstruct three-dimensional data, including internal and external features, and even material defects. Kim [157] presented a paper which is using XCT to inspect different internal features like cube and holes. Samples with internal features were built by L-PBF were scanned by XCT. The results compared with the CAD and the errors in the range of ±0.1 mm. Kerckhofs [158] used XCT data to map strain at different loads in porous Ti–6Al–4V structures, which is correlate component structure and mechanical characteristics.

XCT has the ability to obtain 3D data for characterization of component surface, texture and internal features. It is a technique to study complex structures produced by the additive manufacturing process and can help to find out inner or hidden structures in a non-destructive manner. XCT however of not yet traceable as a measurement technology and is limited by X-ray power to lower density materials for larger parts.

2.5 Summary

This chapter reviews two typical additive manufacturing systems, laser-based additive manufacturing, and electron beam-based additive manufacturing. For AM systems, one of the key challenges is the in-situ process inspection, in-situ inspection can provide effective feedback to reduce the rejection rate to improve the machining efficiency. Post-processing metrology can obtain surface form, texture, and the internal structure of printed parts, which can effectively evaluate the manufacturing accuracy as well as providing an improvement guidance of AM materials and process.

3D optical measurement technology has advantages of non-contact, high - precision and non – destructive. For additive manufacturing processes, the powder bed, the

melted metal surface, and the finished parts all need 3D optical technology inspection. Suitable optical measurement technology can be selected according to different measurement requirements and manufacturing phrase.

Among these techniques, the fringe projection technology has the advantages of full field, high-speed measurement and in-situ measurement, which can provide timely feedback to the processing, and has a good performance in technical stability, compatibility, accuracy and price. However, limitations of calibration dynamic range and measurement speed remain. Deflectometry is the most popular method for full field specular surface measurement. After finishing a printed layer, PMD can inspect highly reflective surfaces. Phase data analysis is introduced as a key process in both fringe projection system and deflectometry systems. The phase calculation algorithms (by Fourier transform and phase shifting) and phase unwrapping algorithms (three-frequency heterodyne selection) are introduced to retrieve the absolute phase information. In this thesis, these two techniques will be mainly investigated to obtain 3D data of AM surfaces and the research aim and objectives are outlined in section 1.3.

Chapter 3 Theoretical and experimental investigation of structure light system for rough surface

This chapter provides a theoretical and experimental investigation of the fringe projection technique, with the focus on system calibration and rough surface inspection within an AM environment. The chapter is divided into eight sections. Section 3.1 is an introduction of the fringe projection technique applied within an EBM machine. Section 3.2 sets out the 3D measurement principle of the fringe projection technique. Section 3.3 covers system calibration methods. Section 3.4 is a simulation experiment. Section 3.5 is the phase error correction methods. Section 3.6 is the development of the prototype inspection systems. Section 3.7 is system evaluation. Section 3.8 is experimental verification of functionality, and section 3.9 is a summary.

3.1 Introduction

Additive manufacturing (AM) techniques provide significant advantages over conventional subtractive manufacturing techniques in terms of a wider range of part geometry that can be obtained. In this thesis, an inspection system is embedded within a powder-based EBeam AM machine. In chapter 1 and chapter 2, the machine structure, composition and basic working principle of powder-based AM machine have been introduced. For this type of machine, powder delivery is a process that occurs many thousands of times during AM build process; consequently, assessment of delivery quality would be advantageous in the process and provide feedback for process control. If the powder delivery process is dysfunctional then during the melting and resolidification process, cracks and pores can occur within the printed objects due to the low quality or inconsistency of the powder delivery [159]. Hence implementation of an effective in-situ detection approach for assessment of delivery quality is essential

to improve manufacturing precision and to enhance product quality [160]. Typical powder delivery defects include (as shown in Figure 3.1): powder flicking due to rake blade spring-back, scores and ridges parallel to the powder rake blade orientation are due to vibrations in the blade, scores or ridges orthogonal to the rake blade are indicative of rake damage or trapped particles, these can result in excessive powder delivery or insufficient powder delivery due to too low powder dosage.

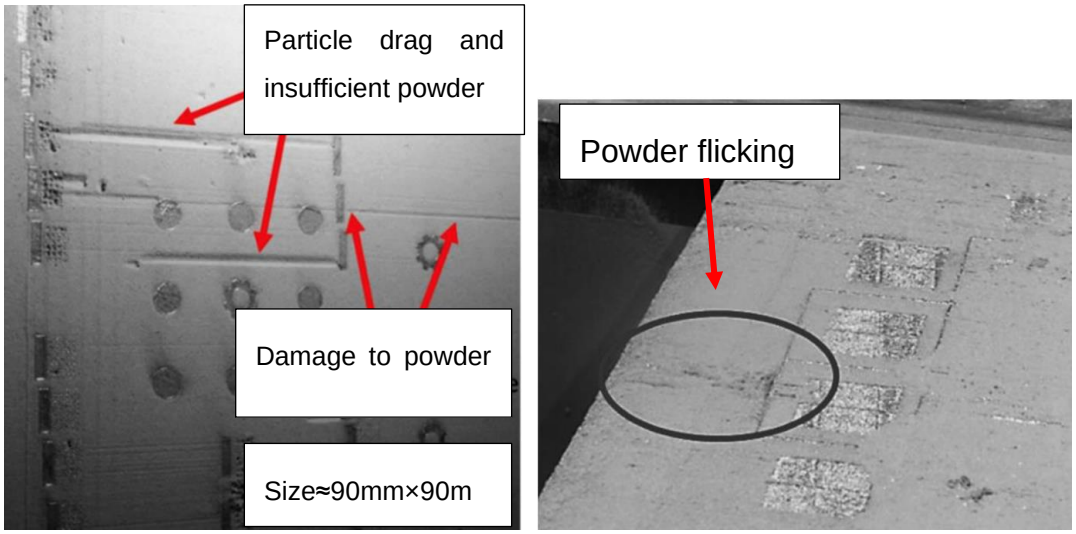

Figure 3. 1 Typical powder bed defects [9]

To avoid difficulties arising from poor powder delivery it is necessary to accurately obtain the geometric information across the whole powder bed or melting surface. For each layer this information needs to be generated after powder delivery and before powder melting is initiated, where this period is of the order of several seconds. Therefore, it is essential to investigate an inspection method that is i) full-field ii) high speed, iii) high accuracy, and iv) has a large field of view (FOV). The fringe projection system employed in this thesis enables the 3D full-field measurement of the powder bed and the thermal expansion. Additionally, it is advantageous if the method can be extended to other monitoring approaches like flaw inspection on the printed part, out of plane part defects or part boundary and could be combined with other in-process

monitoring techniques. Consequently, the application, demonstration, and deployment of fringe projection techniques to in-process inspection during AM manufacture are reported in this chapter.

3.2 3D measurement principle of structured light system based on sinusoidal patterns

3.2.1 Inspection system for AM

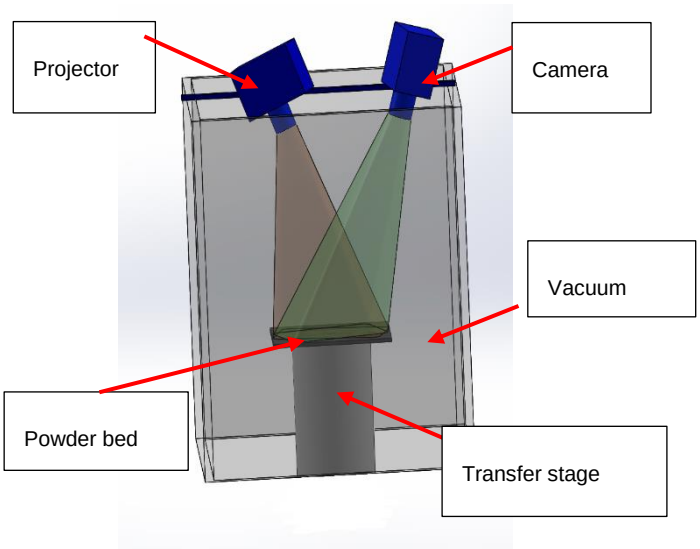

Figure 3. 2 A conceptual set up of the fringe projection inspection system

A conceptual illustration of the in-situ measurement system applied to an EBM machine is shown in Figure 3.2. The final implementation will be within a new prototype EBM machine comprising an electron beam melting source, a powder delivery system, a powder bed transfer stage, and the fringe projection inspection system. The machine itself is a newly launched commercial machine (Wayland Neubeam Calibur3 https://www.waylandadditive.com/). It can exhibit the in-process out-of-plane defects that are common across all AM machines in this category: rake damage, delamination, swelling, porosity, lack of powder. Several technical adaptions to the process have been developed one of which allows a lower pre-heating temperature of 400 °C with the final printing temperature being 1400 °C. The internal environment of the machine

is held under a vacuum. Consequently, the inspection system is fixed on top of the machine outside of the vacuum and the powder bed is “viewed” through leaded glass windows, the windows are protected during the powder melting phase by Kapton film. The fringe projection system consists of a CCD (charge-coupled device) camera and a DLP (digital light processing) projector. The position of the projector and the camera were fixed with the angle between the optical axes of circa 30°. The inspected powder surface is at the intersection of the axes. After powder delivery, the fringe projection system inspects the powder bed quality to assess if the surface is smooth enough to carry on with the process. If the result seems good, the system will carry on with the build, namely powder fusion. Otherwise, the power delivery will be repeated until the surface is smooth enough. After part melting and solidification the part area is scanned to assess out of planar defects and part boundary. Consequently, for a complete build layer the system measures powder delivery and the solidified layer the measurement process flow is shown in Figure 3.3. Between powder delivery and melting and the next powder delivery there are 4 to 5 seconds which is a gap to inspect the powder bed by the fringe projection system.

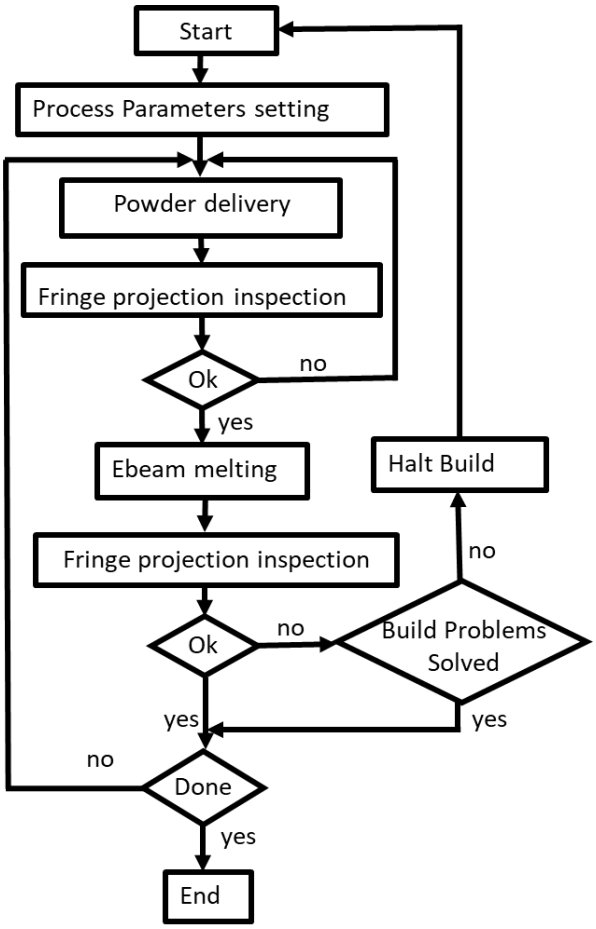

Figure 3. 3 A flow chart of build process

3.2.2 Measurement principle of the fringe projection technique

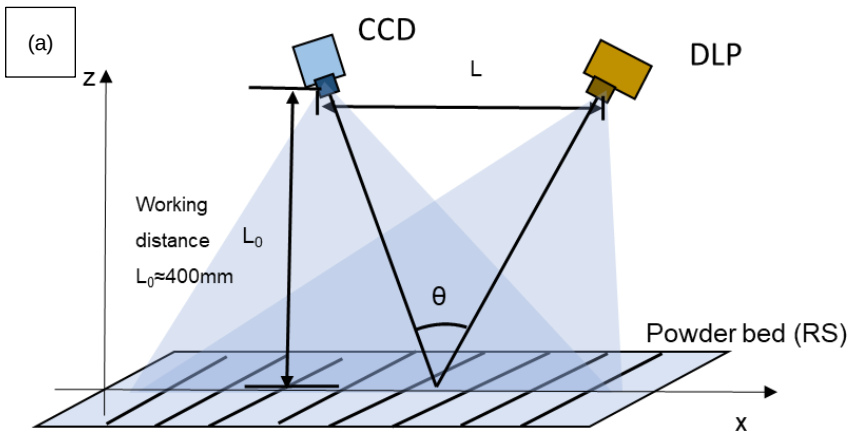

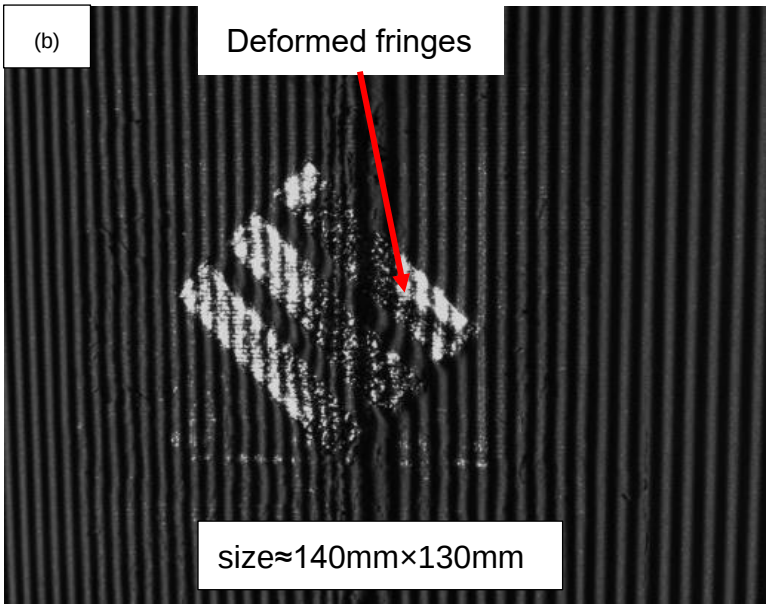

Figure 3. 4 (a) Schematic of fringe projection set up and (b) Camera image of deformed fringes

The principle of the fringe projection technique is based on triangulation [161]. To obtain shape information, the geometric relationship of the DLP projector and the CCD camera should be determined, as illustrated in Figure 3.4. The sinusoidal fringe patterns are projected onto the test surface (powder bed) where, the fringe patterns are deformed due to surface form, and the deformed fringes are captured by the camera. Phase information is computed from the captured deformed fringe patterns. The relationship between the absolute phase data and x is linear. After system calibration, 3D shape data can be obtained using the phase information. Based on triangulation principle in Figure 3.4(a), the geometric relationship of the projector and the camera can be represented by a mathematical relationship between the absolute phase map and depth data [162] as follows:

$$Z = \frac{L_0}{\dfrac{2\pi L_0^2 L\cos\theta}{P_0 \Delta\varphi(x,y)(L_0 + x\cos\theta\sin\theta)^2} - \dfrac{L\cos\theta\sin\theta}{L_0 + x\cos\theta\sin\theta} + 1} \qquad 3.1$$

where Z is the height value relative to reference plane RS. L is the distance between the CCD camera and the DLP projector. Δφ is the absolute unwrapped phase difference between the measured surface and the reference surface RS. L_0 is the working distance from the camera to the reference surface RS. θ is the angle between the optical axes of the projector and the camera and P_0 is the period of the projected fringe pattern on a virtual plane. Therefore, the height values across the surface can be calculated with the phase information and system parameters.

3.3 System calibration

System calibration is a significant process of optical instruments. The precision of calibration results determines the measurement precision. The system calibration of the proposed fringe projection system can be roughly divided into three parts: camera calibration, depth calibration, and transverse calibration.

3.3.1 Camera calibration

The first step is camera calibration which is to establish the relationship between the camera coordinate system and the world coordinate system (or the measurement coordinate system). The camera image system is assumed a pinhole-imaging model as shown in Figure 3.5. (X_c, Y_c, Z_c) is the camera coordinate system. (X_w, Y_w, Z_w) is the world coordinate system. (x, y) is the image coordinate value in the image coordinate system. (u, v) is the pixel coordinate value in the pixel coordinate system. Through geometric transformation between different coordinates, the camera coordinate system is transformed into the world coordinate system [163]. The principle is a simple model to calculate camera parameters that includes internal parameters, external parameters, and lens distortion parameters, etc. Internal parameters are used to describe the transformation relationship between the image coordinate system and

the camera coordinate system, including focal length, main point pixel coordinate, and distortion factor. External parameters are used to describe the transformation relationship between the camera coordinate system and the world coordinate system, including the translation matrix and rotation matrix. The distortion parameters include the radial and tangential distortion parameters of the camera lens.

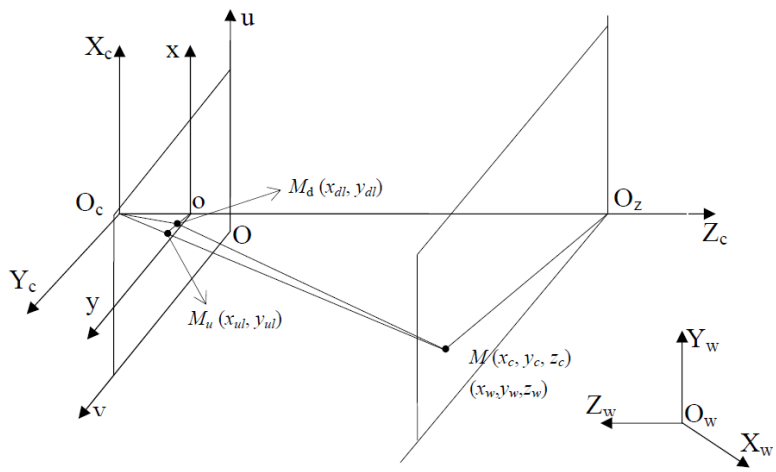

Figure 3. 5 A pinhole-imaging model [164]

In a pinhole-imaging model as shown in Figure 3.5, object point M can be transformed to the corresponding image point M_d by establishing a relationship between four coordinate systems of the world coordinate system, the camera coordinate system, the image coordinate system, and the pixel coordinate system. Equation 3.2 demonstrates the relationship between the camera coordinate system and the world coordinate system.

$$\begin{bmatrix} X_C \\ Y_C \\ Z_C \\ 1 \end{bmatrix} = \begin{bmatrix} R & t \\ 0 & 1 \end{bmatrix} \begin{bmatrix} X_w \\ Y_w \\ Z_w \\ 1 \end{bmatrix} \qquad 3.2$$

where X_c, Y_c, Z_c are the coordinate values in the camera coordinate system and X_w, Y_w, Z_w are the coordinate values in the world coordinate system. R is a 3 by 3 rotation matrix. t is a 3 by 1 translation matrix. Equation 3.3 demonstrates the relationship between the image coordinate system and the camera coordinate system.

$$\begin{bmatrix} x_{ul} \\ y_{ul} \\ 1 \end{bmatrix} = \frac{1}{z_c} \begin{bmatrix} f & 0 & 0 & 0 \\ 0 & f & 0 & 0 \\ 0 & 0 & 1 & 0 \end{bmatrix} \begin{bmatrix} x_c \\ y_c \\ z_c \\ 1 \end{bmatrix} \quad 3.3$$

where X_{ul}, Y_{ul} are the coordinate value in the image coordinate system and f is the focal length. Equation 3.4 demonstrates the relationship between the pixel coordinate system and the image coordinate system.

$$\begin{bmatrix} u \\ v \\ 1 \end{bmatrix} = \begin{bmatrix} \frac{1}{dx} & 0 & u_0 \\ 0 & \frac{1}{dy} & v_0 \\ 0 & 0 & 1 \end{bmatrix} \begin{bmatrix} x_{ul} \\ y_{ul} \\ 1 \end{bmatrix} \quad 3.4$$

where u, v are pixel coordinate value in the pixel coordinate system. According to Equation 3.2 to Equation 3.4, the final transformation relationship between the pixel coordinate system and the world coordinate system can be acquired as:

$$\begin{bmatrix} u \\ v \\ 1 \end{bmatrix} = \frac{1}{z_c} \begin{bmatrix} \frac{f}{dx} & 0 & u_0 \\ 0 & \frac{f}{dy} & v_0 \\ 0 & 0 & 1 \end{bmatrix} \begin{bmatrix} R & T \end{bmatrix} \begin{bmatrix} x_w \\ y_w \\ z_w \\ 1 \end{bmatrix} \quad 3.5$$

The Equation 3.5 can be simplified to Equation 3.6,

$$Z_c \begin{bmatrix} u \\ v \\ 1 \end{bmatrix} = M_1 M_2 A_w \qquad 3.6$$

where M_1 is internal parameters matrix and M_2 is external parameters matrix. There are many methods to calculate the above parameters, the core of which is the use of a flat plate with markers, where the markers are used to record the pixel position and the true spatial size. In this thesis, a chessboard is applied to obtain internal and external parameters for camera calibration as shown in Figure 3.6.

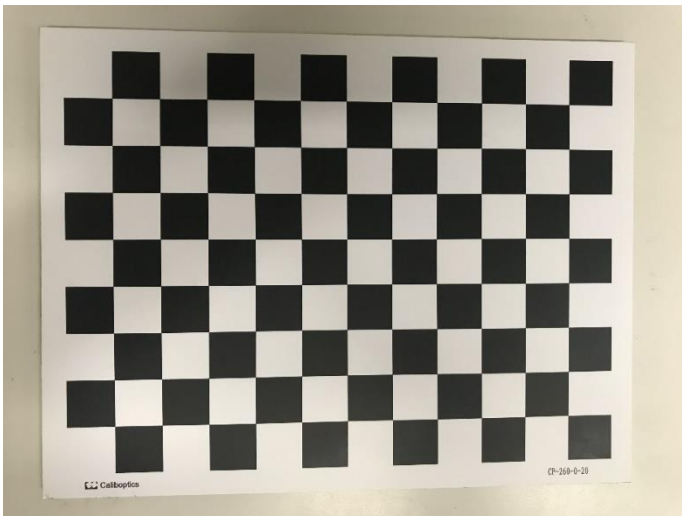

Figure 3. 6 A chessboard for camera calibration

The material of the chessboard is stiff PVC. The dimensions of each grid are 2mm and the accuracy is around 0.01mm. The chessboard is placed in the depth of field of the camera and to “pose” in different angles and positions as shown in Figure 3.7. The camera captures the images that are including all corner points and in different angles as shown in Figure 3.8 (a). Based on all captured images, the corner points are extracted which are marked with red crosses as shown in Figure 3.8(b). The corner points are used to record the pixel positions.

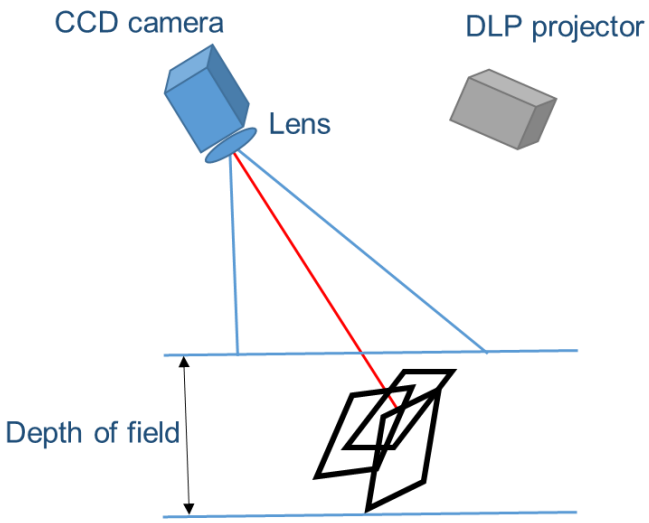

Figure 3. 7 The position of the chessboard in the camera coordinate system

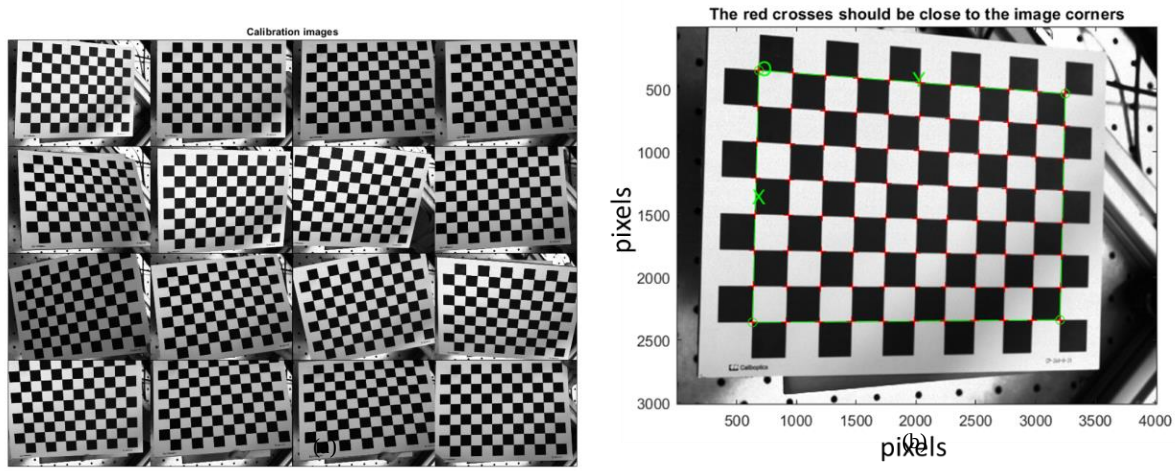

Figure 3. 8 Camera captured chessboard images (a) All captured images (b) Extracted corner points

After extracting corner points and calculating by Equation 3.2 to Equation 3.6, the internal parameters of the camera can be obtained. Table 3.1 is the main internal parameters of the camera. The reprojection errors based on the captured images are around 0.26 pixels in the two directions. The reprojection images are shown in Figure 3.9. The posed chessboards are drawn in the camera coordinate system where the working distance is about 400 mm.

Table 3. 1 Internal parameters of the camera

Focal Length	[8422.6987 8427.1023] +/-[4.5129 4.6054]
Principal point	[1990.3572 1499.646]+/-[4.0554 2.8055]
Reprojection error	[0.2616 0.2370]

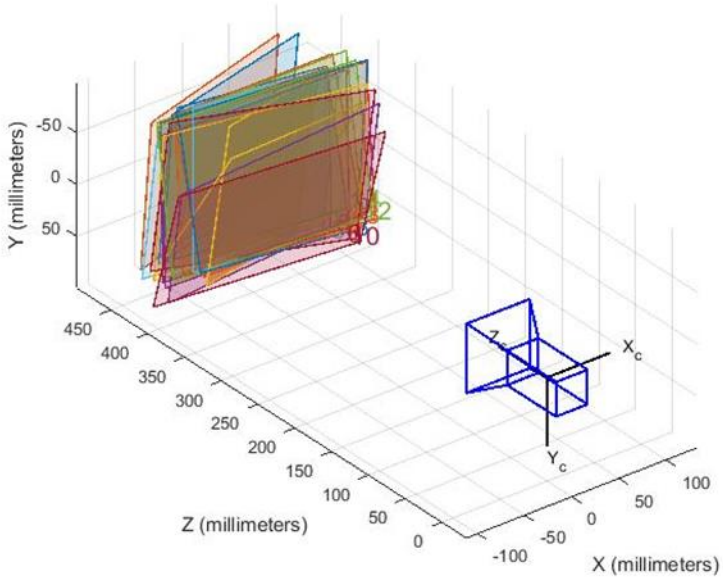

Figure 3. 9 Camera calibration results

3.3.2 Depth calibration

A significant step for an in situ optical imaging system is calibration. Calibration is a process of determining the geometrical relationship between a camera and a projector, as well as the relationship between the world coordinate and the camera image coordinate, which affects the measurement resolution and repeatability. Existing calibration methods for 3D inspection systems have been introduced in chapter 2. In this chapter, based on a phase-depth calibration model, two novel calibration methods are reported to reduce phase error and random noise and eliminate the calibration induced “circle mark” effect. The proposed calibration methods can be used in an AM machine environment with a calibration procedure using a certified calibration board.

System calibration establishes the relationship between the depth information and phase data, and the relationship between the spatial position of a selected point in a real-world coordinate system and the corresponding pixel position in the camera coordinate system, these are termed depth calibration and transverse calibration, respectively. It is difficult to directly obtain the system parameters L, L0, P0 for depth calibration (Equation 3.1). However, by using a Taylor series expansion [162], Equation 3.1 can be transformed into a polynomial function.

$$Z_r(x, y) = \sum_{n=0}^{N} a_n(x, y)\Delta\varphi(x, y)^n \qquad 3.7$$

where a_n, a_{n-1}, a_2, a_1 are sets of coefficients containing the depth parameters. Z_r is measurement height in reference coordinate system. The coefficients will have different values for every pixel and can be stored in a look-up table (LUT). Therefore, the complex geometrical relationship (Equation 3.1) is transformed into the simple polynomial function (Equation 3.7). The main task of depth calibration becomes the optimization of the coefficients of Equation 3.7. If the phase information and the corresponding height information are known, the polynomial coefficients can be determined.

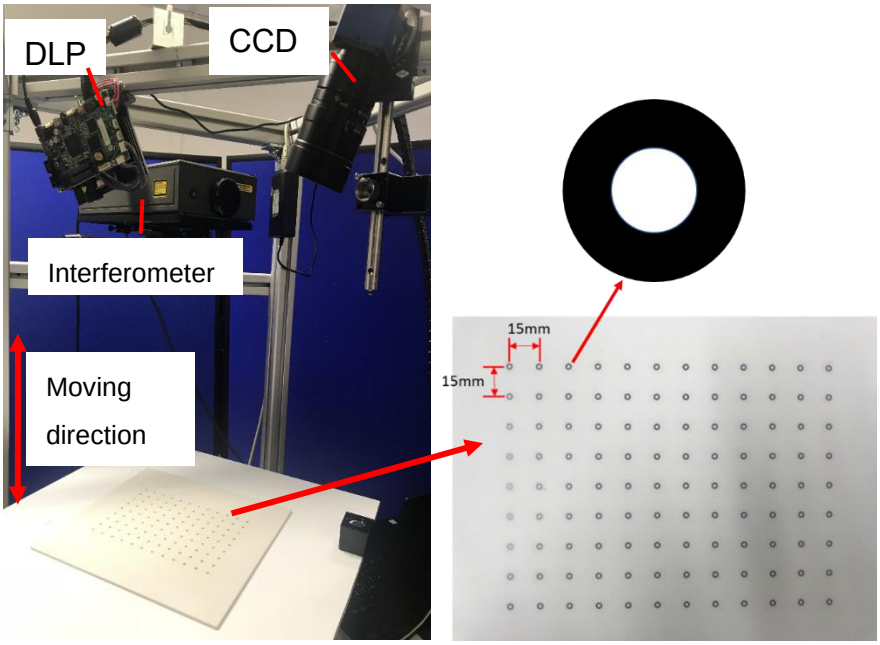

Figure 3. 10 Fringe projection system and ceramic calibration board with concentric circles

Since any black surface texture will affect the phase accuracy, the calibration should choose a diffuse reflection plate with a large blank area and can accurately locate the pixel position. Therefore, a white ceramic diffuse plate with certified concentric circles markings is employed in the calibration procedure as shown in Figure 3.10. The circle board was accompanied by a calibration certificate guaranteeing the tolerance range of the centre positions within +/-0.002mm. The circle ring board and the chessboard work on the same principle: they both use marker points to record pixel positions. The checkerboard is used to extract the black and white corner points as markers, and the circle ring board is used to calculate the centre of the concentric circle as markers.

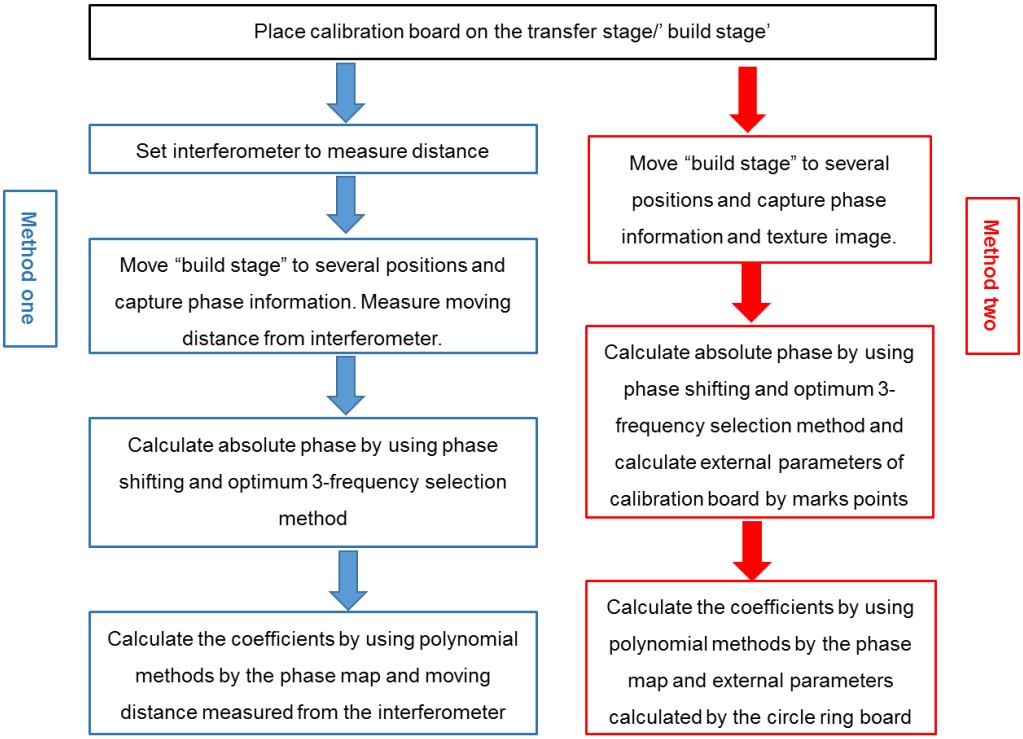

Figure 3. 11 The procedure of depth calibration

There are two methods to calibrate depth. The procedure of calibration is shown in Figure 3.11. Method one is shown at the left part, an independent absolute distance measurement interferometer (Renishaw Model: ML10) is used in the method one. The circle ring board is placed on a transfer stage and moved to a series of positions in the measurement range. Based on the position of the calibration board, the middle position is taken as a reference surface. Based on the reference surface, a reference coordinate system (represents world coordinate system) can be constructed. At each position, the movement distance can be recorded by a length measurement traceable interferometer (as shown in Figure 3.10). At each position, the fringe patterns are projected onto the calibration board. The phase information from the projected fringe patterns of the calibration board is collected. After obtained phase data and depth data, a least-squares algorithm is employed to optimize the coefficient values based on Equation 3.7. Consequently, the geometric relationship between the camera and the

projector can be determined. The second method is shown on the right of Figure 3.11, which calculates depth data from ring marks using the internal AM machine build table movement system feedback form the machine control parmeters. This second method is employed “in the field” iinstead of measuring the moving distance via the interferometer. The circle ring board is placed on the transfer stage. A series of fringe patterns and blank intensity images are projected on the board. The camera captures these fringe patterns and a texture image and then moves to the next position. This process is repeated until all data are collected. The phase information can be obtained by calculating the fringe patterns. By extracting the centre of the ring to record the pixel positions, the relative depth of each moving position, namely the moving distance, can be obtained by using the camera calibration results. After obtaining texture images, the images are processed by binarization. The centre points of the concentric circles are then extracted with an ellipse fitting algorithm[165] to record pixel positions in the camera coordinate system as shown in Figure 3.12. External parameters of the calibration board, namely rotation and translation matrix, can be calculated by marked points and internal parameters of the camera. Therefore, the moving distance can be obtained by the calibration board positions. The coefficients of Equation 3.7 can be calculated by the depth data and the phase data. All phase data are calculated by using phase-shifting and optimum three frequency selection algorithms which are introduced in chapter 2.3.

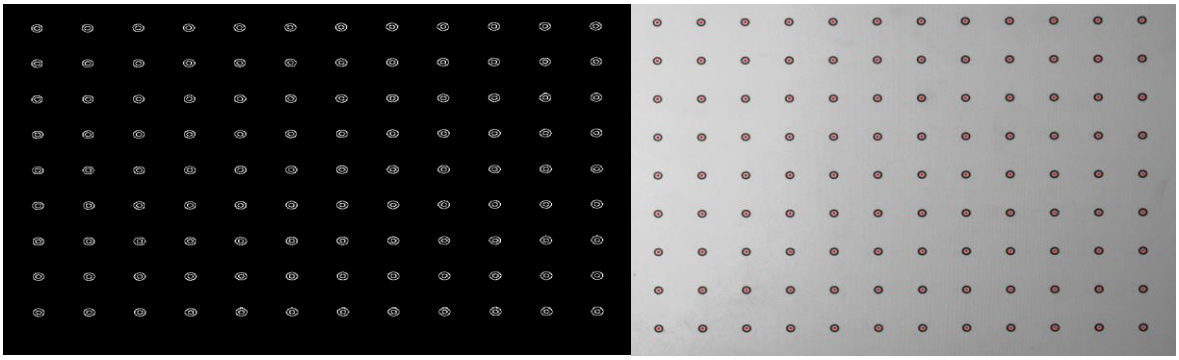

Figure 3. 12 Binarization and centre extraction of circle ring

By calculating the positions of the calibration plate through the rings, the moving distance is obtained and compared with the moving distance measured by the interferometer as shown in Figure 3.13. Figure 3.13(a) shows the position of the calibration plate at a depth of 1mm in the reference coordinate system in AM system as shown in Figure 3.14(a), i.e., the plane is 1 mm from the reference plane. The blue line is the depth result of the board by Method two, while the red line is the measured depth result of the board by the interferometer. There is a certain error of calculation depth from the ring marks, namely method two. One important reason is that the camera views the calibration plate to take pictures at a certain angle due to the AM system structure as shown in Figure 3.14(a). Because of the angle between the optical axis of the camera and the normal line of the calibration plate, a perfect circle becomes an ellipse in the camera view as shown in Figure 3.14(c). Therefore, the centre point extraction is inaccurate which involves calculation errors as shown in Figure 3.14 (c). The black point is the extraction centre of the ellipse, while the red cross mark is the real centre in the camera view. Δx is an extraction error. Figure 3.13(b) shows the position of the calibration plate at the depth of 5 mm in the reference coordinate system, and the error is more obvious when the distance is larger.

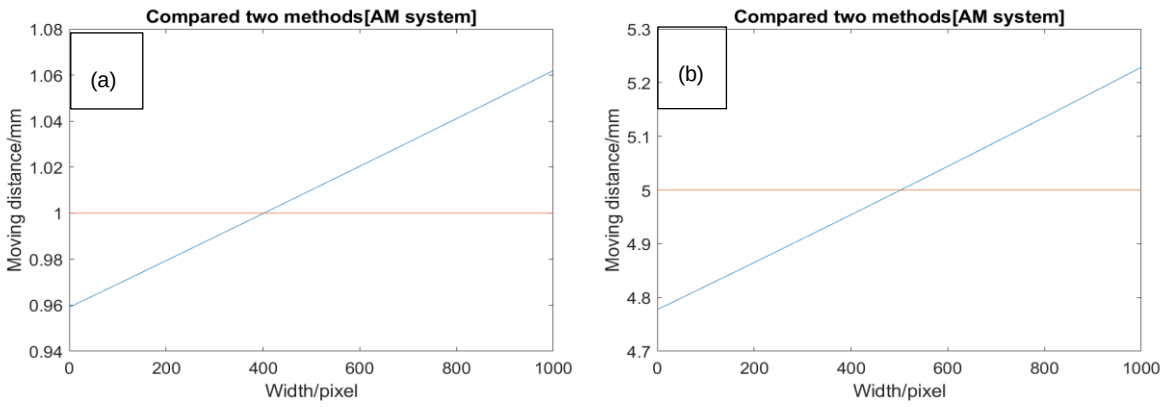

Figure 3. 13 Compared with two obtaining depth data methods in AM system

Figure 3.14 shows two different structure fringe projection systems. Figure 3.14(a) shows the fringe projection system embedded in the AM system. Due to the existence of an Ebeam source in the centre, the both optical axis of the camera and the projection have a certain angle with the reference plane. Figure 3.14(b) shows the fringe projection system with the camera facing the reference plane. As mentioned above, there is an error in the extraction of the center of the concentric circle when there is an angle between the optical axis of the camera and the calibration plate as shown in Figure 3.14(c). For the fringe projection system without structure limitation, higher calibration accuracy can be obtained when the position of the camera is facing the calibration board directly in both two calibration methods. In this case, the centre extraction of the concentric circle is more accurate as shown in Figure 3.14(b) than that of the rings collected by the camera with a certain angle. Figure 3.15(a) shows the position of the calibration plate at a depth of 1mm in the reference coordinate system in the system Figure 3.14(b), which reduces error from 0.04mm to 0.01mm. The blue line is the calculation depth result of the ring marking points, while the red line is the measurement result of the interferometer. Figure 3.15(b) shows the position of the calibration plate at the depth of 5 mm in the reference coordinate system, which

reduces error from 0.2m down to 0.01mm. Therefore, in this thesis and to demonstrate proof of principle, the interferometer is employed to measure the depth to obtain higher calibration and measurement accuracy.

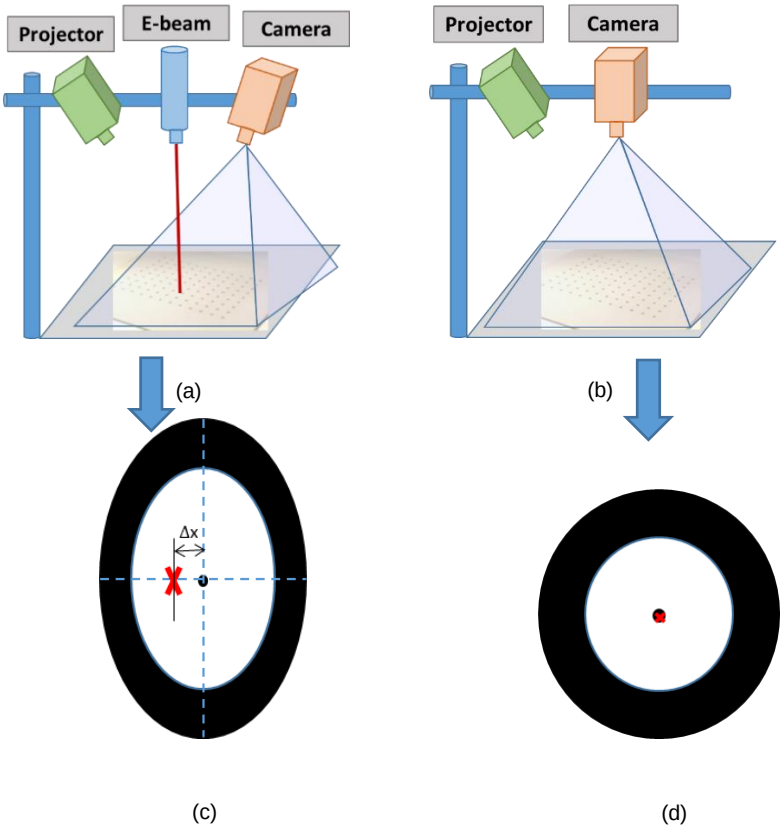

Figure 3. 14 Two fringe projection system with different view angles and the centre extraction errors(a)AM fringe projection system (b) The camera face to the calibration board (c) centre extraction error in ellipse centre (d) extraction in circle ring

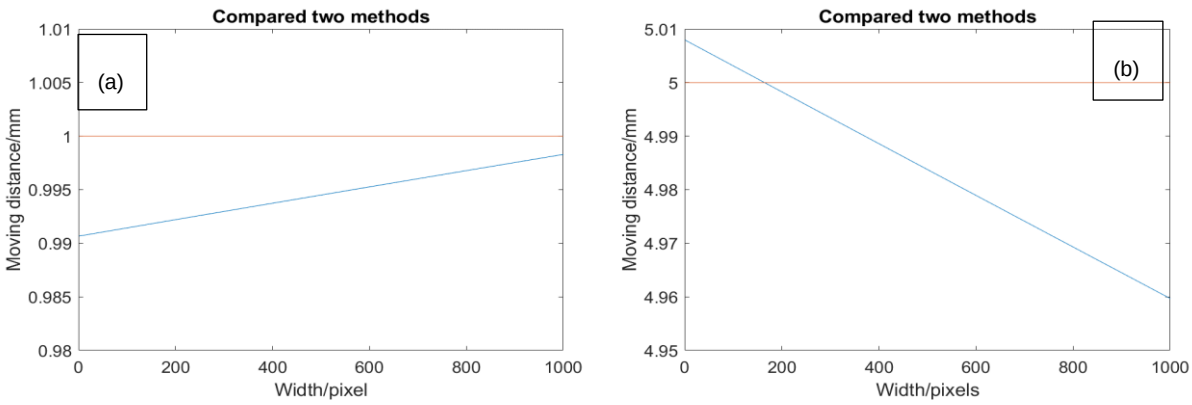

Figure 3. 15 Two obtaining depth method when the camera directly face to the calibration board

3.3.3 Transverse calibration

The extracted centre of the concentric circle can not only calculate the depth position of the calibration plate but also calculate the transverse coordinate value of the calibration plate by using the transformation relationship between the image coordinate system and the pixel coordinate system. Figure 3.16 shows a schematic view of the transverse calibration. In general, for an optical imaging system, there is a nonlinear effect because of the distortion of the optical lens. Although camera calibration can correct the distortion from the CCD camera to some extent, when using the optical system, it is difficult to achieve a perfect pinhole image. When the calibration board is moved in the vertical plane using a translating stage, the path of the marked points is a curve in the camera coordinate system.

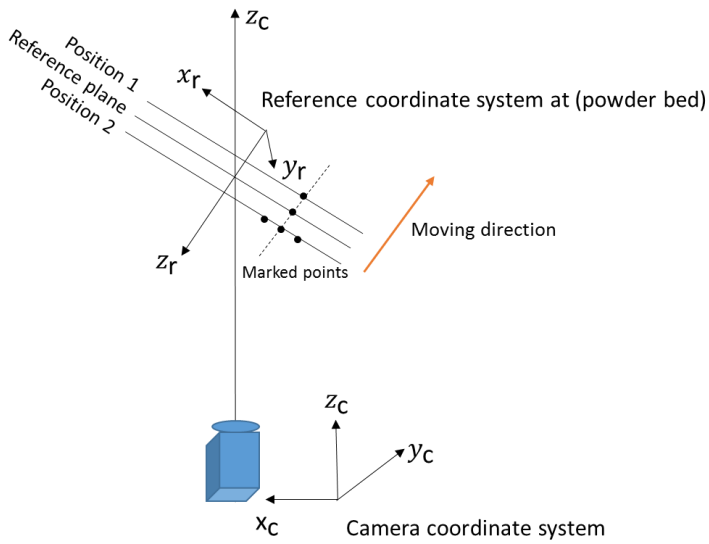

Figure 3. 16 Schematic of transverse calibration

Therefore, the relationship between X and Z, Y and Z can be expressed as quadric functions,

$$X_r(x,y) = b_1 Z_r(x,y)^2 + b_2 Z_r(x,y) + b_3 \quad 3.8$$

$$Y_r(x,y) = c_1 Z_r(x,y)^2 + c_2 Z_r(x,y) + c_3 \quad 3.9$$

where b_1, b_1, b_2, c_1, c_2, c_3 are the coefficients of the quadric in the reference coordinate system. X_r and Y_r are the coordinate values in the reference coordinate system which is transferred by a homography matrix from the corresponding pixel positions in the camera coordinate system [**Error! Bookmark not defined.**]. Z_r is the calibration board position in the reference coordinate system, where the calculation methods are introduced in section 3.3.2. In this thesis, Z_r is the average of the distance between each calibration position measured by the interferometer and repeated 20 times. The calibration procedure flowchart is shown in Figure 3.17. After recording a series of known distances, X_r and Y_r are the coordinate values on the calibration board, the polynomial coefficients of Equations 3.8 and 3.9 can be calculated by a least-squares algorithm.

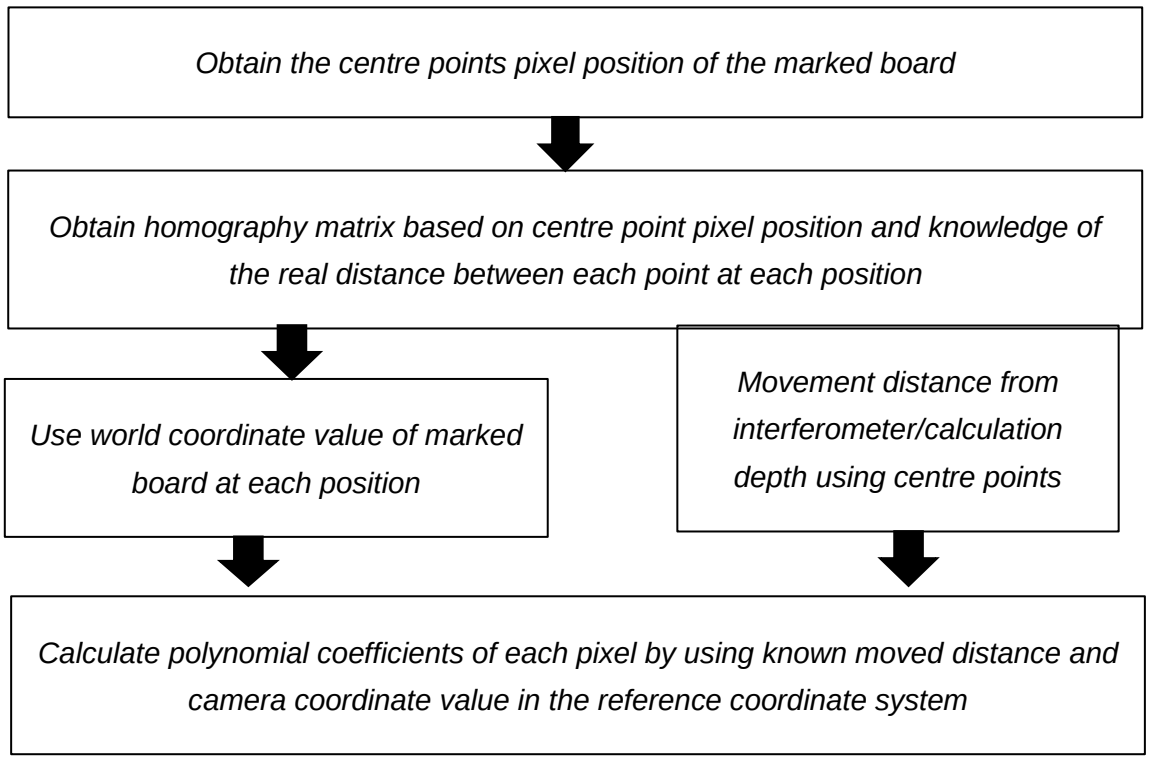

Figure 3. 17 The transvers calibration procedure flowchart

3.4 Simulation

To test the proposed inspection system and calibration methods, simulation was carried out to verify the feasibility and validity of the proposed technique.

The least-squares calibration algorithm was employed during both depth calibration and transverse calibration, which uses a set of known captured depth positions to optimize system parameters. Therefore, a simulation is conducted to verify the feasibility of the calibration method. Equation 3.10 represents the relationship between the absolute phase difference and the height in different depth positions.

$$\begin{pmatrix} Z_{r1}(x,y) \\ Z_{r2}(x,y) \\ Z_{r3}(x,y) \\ \cdots \\ Z_{rk}(x,y) \end{pmatrix} = \sum_{n=0}^{N} \begin{pmatrix} a_{r1}(x,y) \\ a_{r2}(x,y) \\ a_{r3}(x,y) \\ \cdots \\ a_{rk}(x,y) \end{pmatrix} \begin{pmatrix} \Delta\varphi_{r1}(x,y)^n \\ \Delta\varphi_{r2}(x,y)^n \\ \Delta\varphi_{r3}(x,y)^n \\ \ldots \\ \Delta\varphi_{rk}(x,y)^n \end{pmatrix} \quad 3.10$$

Where Z_{rk} is a known distance along vertical direction, a_{rk} is the coefficient of depth-phase calibration, $\Delta\varphi_{rk}$ is the phase difference between the calibration positions and the reference position RS, (x,y) represents the pixel positions of the camera, n is the polynomial order , k is the calibration position number and its minimum value is n+1. The aim of the simulation is to verify k, which can influence measurement accuracy. Therefore, the simulated different depth values and the corresponding phase values optimise the coefficients by adding random noise into phase values. The simulated depth values separate into six to eighty-four sets, which means k equals six to eighty-four within a given depth range. In other words, in the actual process of calibration, the movement positions of the calibration board are changed from six to eighty-four times in increments of 2 positions within a given depth range. According to the actual camera noise level, 2% random noise is added into the phase difference to calculate the coefficients value based on Equation 3.10. The standard deviation of depth error at each position is shown in Figure 3.18, whose variation is from 0.0163mm to 0.004mm.

The simulation results show that when the calibration position is more than 20, i.e. K is larger than 20, the standard deviation of the measured depth oscillates at 0.006mm. Therefore, considering the calibration time and measurement accuracy comprehensively, 21 calibration positions were selected as the most appropriate in the actual calibration process. The simulation shows that the least-squares calibration algorithm can suppress random noise by increasing calibration positions. The random noise can be reduced by increasing the calibration positions within a given calibration depth range.

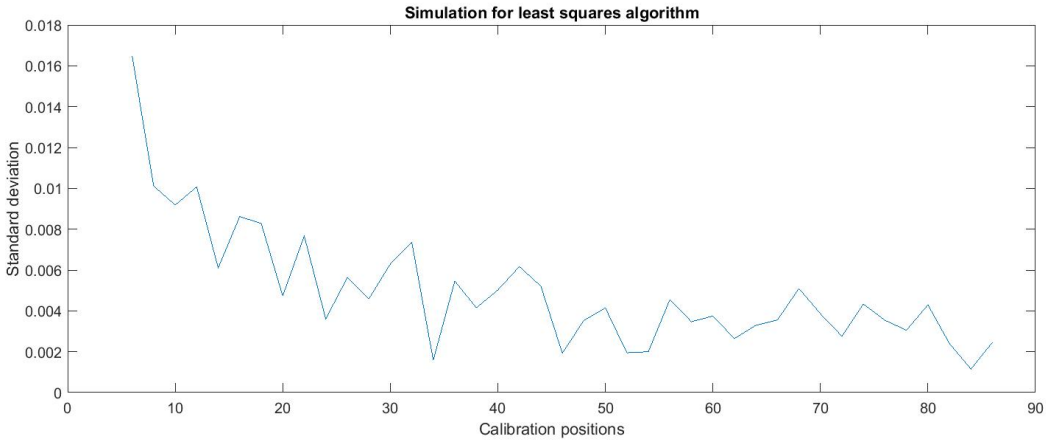

Figure 3. 18 Simulation of measurement accuracy for the proposed method

3.5 Phase error corrections

In the calibration process, it is necessary to use the marked calibration board to record pixel positions and phase information, namely the checkerboard and the ring calibration board. The colour of the markers affects the phase accuracy causing phase noise. This section proposes two novel methods to eliminate phase errors and improve measurement accuracy.

3.5.1 Surface fitting calibration

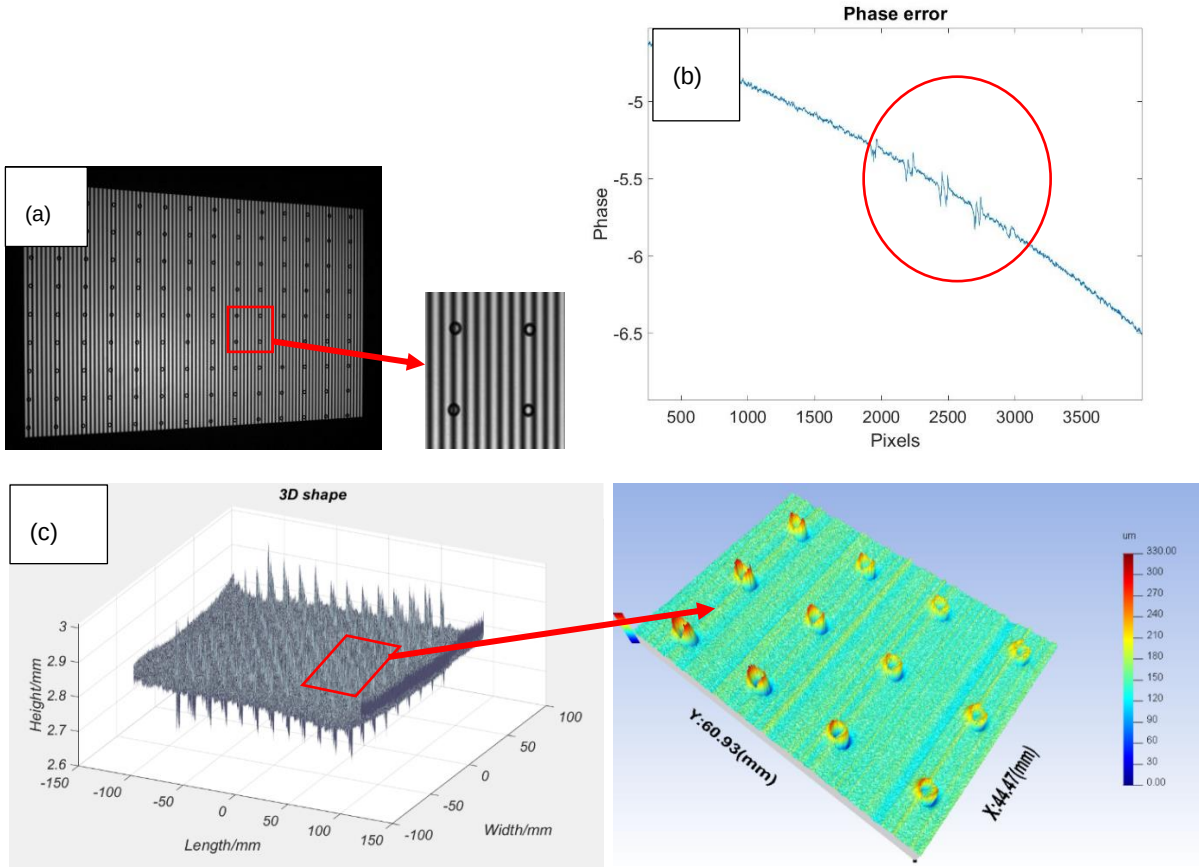

Figure 3. 19 Phase error and measurement error (a) The impact of calibration board black circle rings on captured phase data (b) The measurement results due to the effects of the black circle rings on the calibration board (c) The zoomed area of the measurement results

Due to the presence of the black circle rings on the calibration board, the captured fringe patterns have low fringe contrast, which results in phase error and measurement error, as demonstrated in Figure 3.19. Figure 3.19(a) is a fringe image on the circle ring board. The circle ring areas are black and absorb the projected light, and the profile image of the absolute phase that crosses the circle ring area is shown in Figure 3.19(b). Figure 3.19(b) is the 3D result of the calibration board due to the effects of the black circle rings. Figure 3.19(c) is the zoomed area of the measurement results. A novel calibration approach based on a curve-fitting algorithm was applied to solve this problem. The modulation of the fringe patterns is calculated by Equation 3.11,

which functions as a technique to remove the noisy points. By setting a threshold value, the outliers and the invalid points having low modulation can be identified.

$$M = \frac{2}{N} \times \sqrt{\left[\sum_{n=0}^{N-1} I_n \sin\left(\frac{2\pi n}{N}\right)^2\right] + \left[\sum_{n=0}^{N-1} I_n \cos\left(\frac{2\pi n}{N}\right)^2\right]} \qquad 3.11$$

M is the fringe modulation, N is phase-shifting steps, n is the captured image sequence, I_n is the intensity of the captured images. Therefore, the outliers crossing the circle ring area are removed, as shown in Figure 3.20(a). The unwrapped phase map is calculated from the rest of the wrapped phase data by using the optimum 3-frequency selection algorithm [135], as shown in Figure 3.20(b).

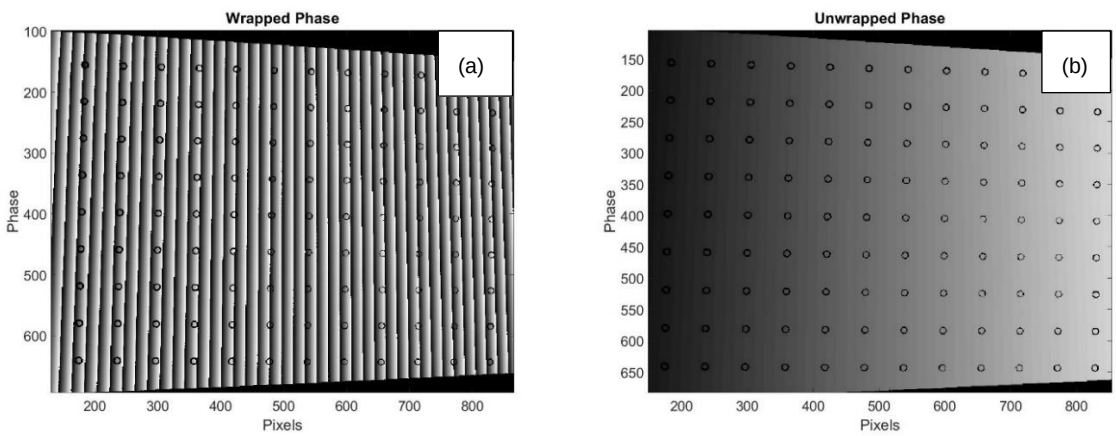

Figure 3. 20 Wrapped phase map and unwrapped phase map after identifying outliers(a) Wrapped phase with the outliers removed (b) Unwrapped phase without the outliers

To fill in the invalid points, a quintic polynomial fitting equation was investigated to match the unwrapped phase data as follows:

$$FittingPhase = P_0 + P_1x + P_2y + P_3x^2 + P_4xy + P_5y^2 + P_6x^3 + P_7x^2y + P_8xy^2 + P_9y^3 + P_{10}x^4 + P_{11}x^3y + P_{12}x^2y^2 + P_{13}xy^3 + P_{14}y^4 + P_{15}x^5 + P_{16}x^4y + P_{17}x^3y^2 + P_{18}x^2y^3 + P_{19}xy^4 + P_{20}y^5 \qquad 3.12$$

where x and y are the positions of the pixel, P_n is the coefficients of the fitting equation. Due to the fact that the calibration board is a flat white ceramic plate, the unwrapped

phase map of the calibration board is ideally a plane. Theoretically, a linear fitting can determine the plane. Despite the effort of eliminating the distortion of the lens and the non-linearity of the system, the uneven fringe projection will still distort the unwrapped phase. Therefore, a relatively high-order fitting (quantic polynomial fitting) was used. The points with the deviation (noise) between the fitted results and the original data over three times the standard deviation was removed and discarded. The dataset was then fitted again. This procedure would be repeated until the fitted data accounts for more than 98% of the pre-fitted data. This procedure was iterated three times that achieved the fitting conditions. The experimental results showed that over 98% fitting accuracy was achieved. Compared with the unwrapped phase, the fitted data not only suppress the influence of random noise but also improves the resolution and accuracy in the vertical direction.

3.5.1.1 calibration results

Due to the influence of the black rings, there are errors in the measurement of the ring area and verification of the novel calibration method, a calibration board was placed on two known positions. At each position, it was measured by the certified independent interferometer with a resolution of 1 nm. The plate was positioned at -2.5 mm and 2.5 mm with respect to the testing plane. The measured profile images of before and after corrections are shown in Figure 3.21. The measured distance obtained by the interferometer was taken as the ideal value. The measured average distance detected by the fringe projection system, the absolute error between the measurement results and the ideal value, the standard deviation before and after corrections across the surface, and the repeatability of before and after corrections are listed in Table 3.2. After the corrections, the maximum absolute error is 6.9 μm and the maximum repeatability is 6.8 μm.

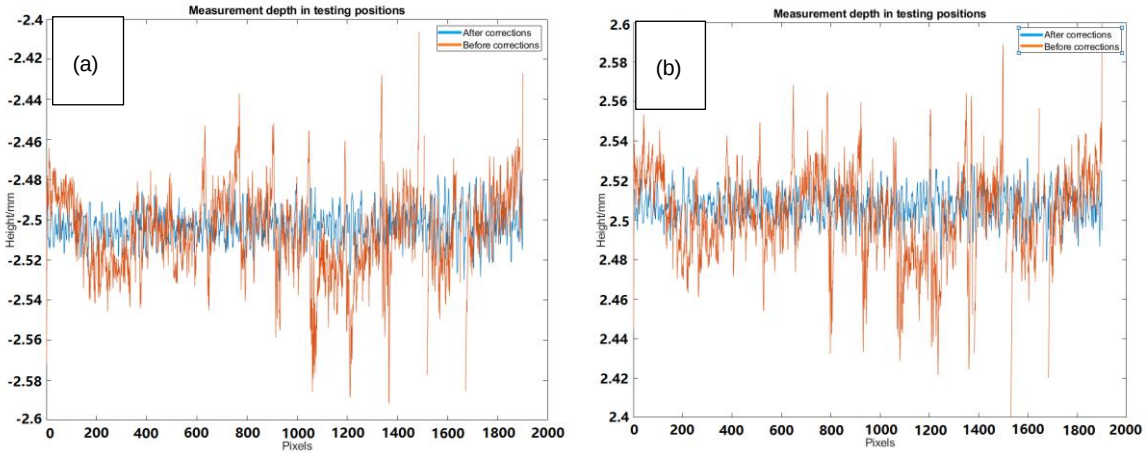

Figure 3. 21 Compared measured distance along one row near the middle of the white plate results between before and after corrections, X axis represents the pixel positions, vertical axis is the reconstructed depth of the surface (a) z=-2.5 mm (b) z=2.5mm

Table 3. 2 Measured distance compared with the interferometer measurement

Interferometer /mm	Measured average distance /mm	Absolute error/mm	Standard deviation/mm (After corrections)	Repeatability /mm (After corrections)	Standard deviation/mm (Before corrections)	Repeatability /mm (Before corrections)
2.5003	2.5072	0.0069	0.0158	0.0041	0.0325	0.0200
-2.5008	-2.5029	0.0021	0.0127	0.0068	0.0296	0.0192

3D results of a flat whiteboard were measured and the proposed fitting calibration algorithm applied is shown in Figure 3.22. These results in Figure 3.22(a) indicate the situation where the impact of the black circle rings is ignored and Figure 3.22 (b) is the improved results by using the novel fitting calibration method. The experimental results show the proposed calibration method solves the impact of black circle ring and suppresses the random noise.

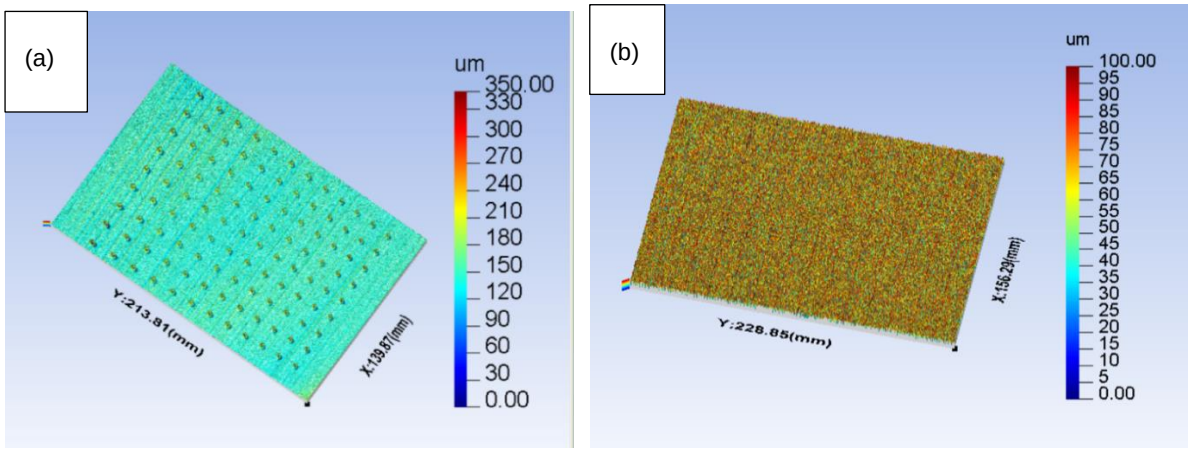

Figure 3. 22 3D shape measurement results of a flat plate (a) 3D shape measurement results with impact of black circle ring (b) 3D shape measurement results with the proposed method

3.5.2 Whiteboard calibration

A surface fitting calibration method was employed in system calibration for eliminating phase error. Another simple calibration method can also be used to solve this issue. It suits the system required high accuracy in the vertical direction and lower accuracy in the transverse direction.

Figure 3.23 shows the procedure of the calibration method. The calibration method needs two parts, depth calibration, and transverse calibration. In the depth calibration, the six coefficients of Equation 3.13 need to be calculated. A white flat calibration board is employed to obtain clear phase data.

$$\Delta H = a_0 + a_1\Delta\varphi + a_2(\Delta\varphi)^2 + a_3(\Delta\varphi)^3 + a_4(\Delta\varphi)^4 + a_5(\Delta\varphi)^5 \qquad 3.13$$

$\Delta\varphi$ is the phase difference between the reference surface and the calibration position surface, which is obtained from the whiteboard. ΔH is the corresponding moving distance between the reference surface and the calibration position.

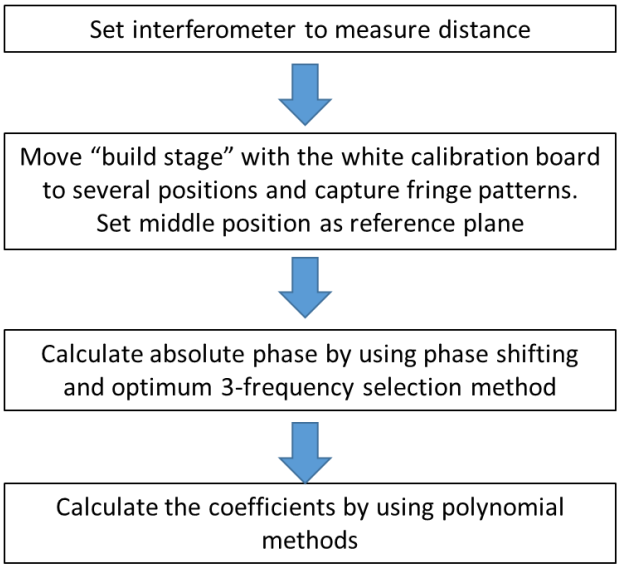

Figure 3. 23 The procedure of the depth calibration

The whiteboard is placed on the 'build stage' and moving to 21 positions. Based on the position of the calibration board, the middle position is as a reference surface. Based on the reference surface, a reference coordinate system (represents world coordinate system) can be constructed. Moving direction is the Z-axis. At each position, the movement distance can be measured by the interferometer. At each position, the fringe patterns are projected onto the white calibration board. The phase information from the projected fringe patterns of the calibration board is collected. After moved to 21 positions, 21 absolute phase maps can be obtained and the corresponding moving distance measured by the interferometer. Based on these obtained phase data and depth data, namely $\Delta\varphi$ and ΔH, a least-squares algorithm is applied to optimize the coefficient values of Equation 3.13. A set of high accuracy coefficients of Equation 3.13 can be calculated pixel by pixel, which results do not have the black ring effect.

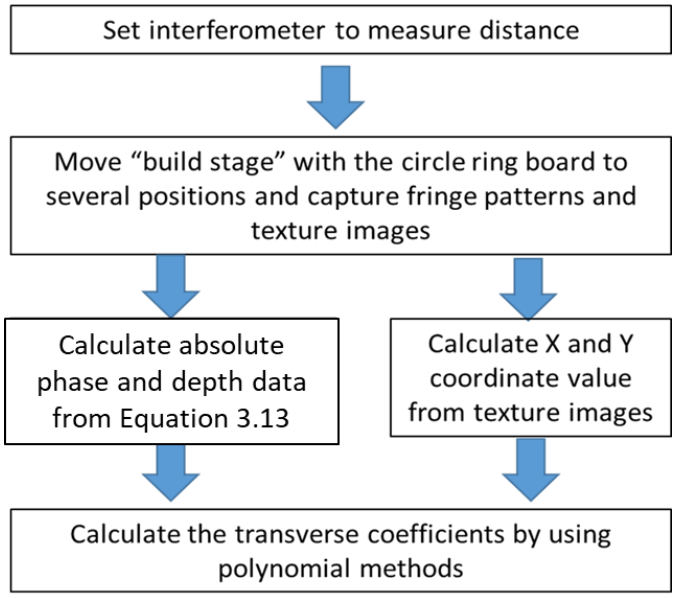

Figure 3. 24 The procedure of transverse calibration

After obtained the coefficients of Equation 3.13, the depth calibration is completed. The whiteboard is replaced by the circle ring board on the 'build stage'. The circle ring board is moved to 10 positions, which are in the field of calibrated depth. The same sinusoidal fringe patterns are projected on the circle ring board. The camera captured them and a texture image at each position. The phase maps and the corresponding marked points images are obtained. The height difference between the moving position of the circle ring board and the reference surface can be calculated by Equation 3.13. A crossline of the calculated height is selected where does not through the ring area, the selected height is fitted by the polynomial equation. The coefficients of Equation 3.14 and Equation 3.15 are optimized by using the fitting height results and the world coordinates of X and Y calculated by the centre of the concentric circle (introduced in Chapter 3.3.3) as parameters. Figure 3.24 shows the procedure. The transverse calibration is completed.

$$X = b_1 + b_2 \Delta H + b_3 (\Delta H)^2 \qquad 3.14$$

$$Y = c_1 + c_2 \Delta H + c_3 (\Delta H)^2 \qquad 3.15$$

Consequently, the geometric relationship between the camera and the projector can be determined.

3.5.2.1 Calibration results

To verify the proposed calibration method, a white plate was measured by two methods. The depth data was calculated from the circle ring plate calibration results, as shown in Figure 3.25(a). The depth data was calculated using the proposed calibration results as shown in Figure 3.25(b). It can be seen that the circle rings effect was eliminated by comparing the two calibration results. It can be concluded the proposed calibration method effectively reduced the marker effect of the ring marks in the calibration process.

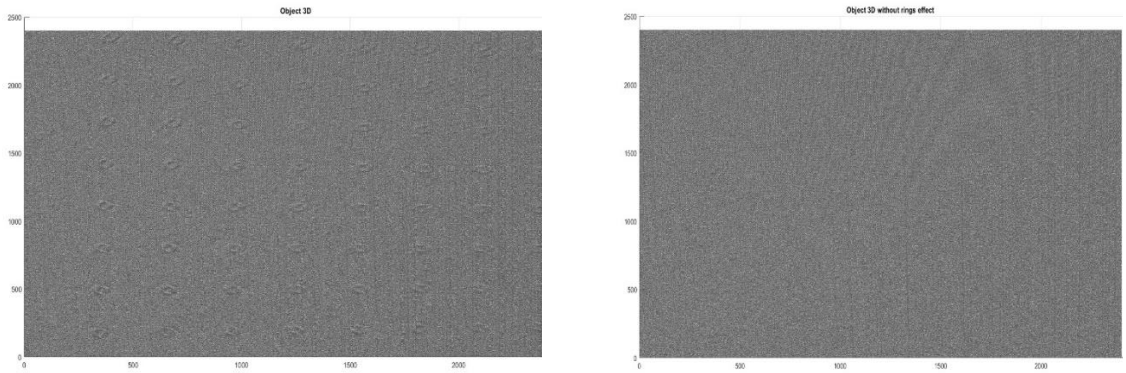

(**a**) (**b**)

Figure 3. 25 Measurement results of a flat plate (a) 3D shape measurement results with impact of black circle ring (b) 3D shape measurement results with the proposed method

In order to verify the measurement accuracy of the system, the calibration board was placed at two known vertical positions. At each position, the board was measured by an independently certified interferometer with a resolution of 1 nm. The plate was positioned at around -5.4 mm and 1.3 mm with respect to the testing plane, as the measured profile images are shown in Figure 3.26. The measured distance obtained by the interferometer was taken as the ideal value and was measured 20 times. The

measured average distance detected by the inspection system, the absolute error between the measurement results and the ideal value and the standard deviation are listed in Table 3.3. The maximum absolute error was 25.9 μm. The standard deviation was around 17 μm.

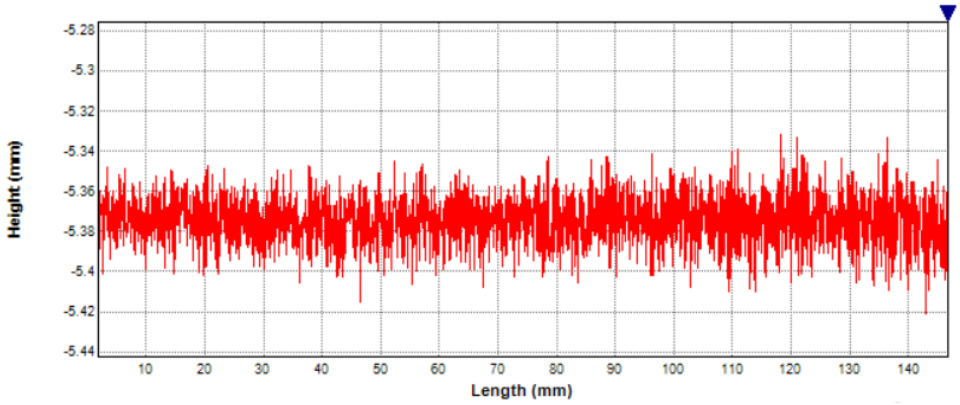

(a)

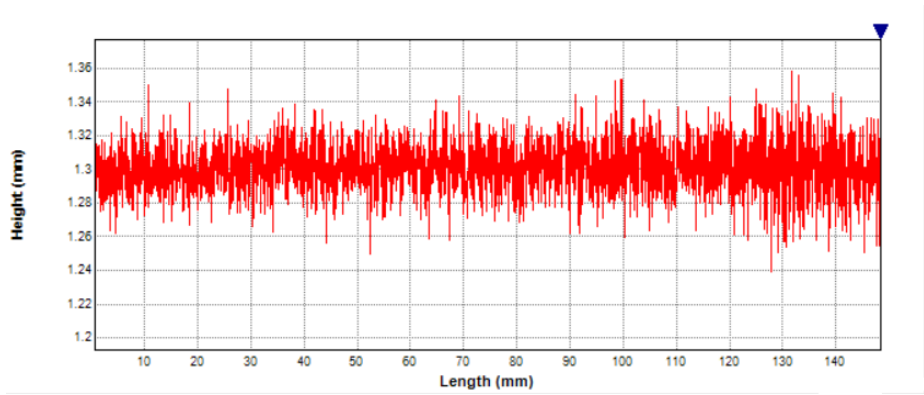

(b)

Figure 3. 26 Compared measured distance along one row near the middle of the white plate results, X axis represents the width, vertical axis is the reconstructed depth of the surface (a) z=-5.4 mm (b) z=1.3mm

Table 3. 3 Details of the accuracy and precision along depth direction

Position(mm)	Mean measured distance (mm)	Mean absolute error(mm) (accuracy)	Standard deviation(mm) (precision)
-5.3987	-5.3728	0.0259	0.0168
1.2982	1.2954	0.0028	0.0126

3D results of proof of concept measurement samples were shown in Figure 3.27, Figure 3.28 and Figure 3.28. Figure 3.27 was a 3D measurement result of a coin. Figure 3.27(a) shows a twenty-cent coin. Figure 3.27(b) shows the 3D measurement results of the coin after corrections by proposed method. Figure 3.27(c) shows the 3D measurement results of the coin before corrections. Figure 3.27(d) was the zoomed error area of 3D measurement results. The proposed calibration method clearly eliminated the effect of the rings. Figure 3.28 illustrates the profile of the zoomed error area. It can be seen that the range of the error is 150 µm to 200 µm in the ring region without correction. If the ring effect were not corrected for, then the ring effect hidden in the calibration coefficient would lead to a measurement error of 200 µm in the ring area.

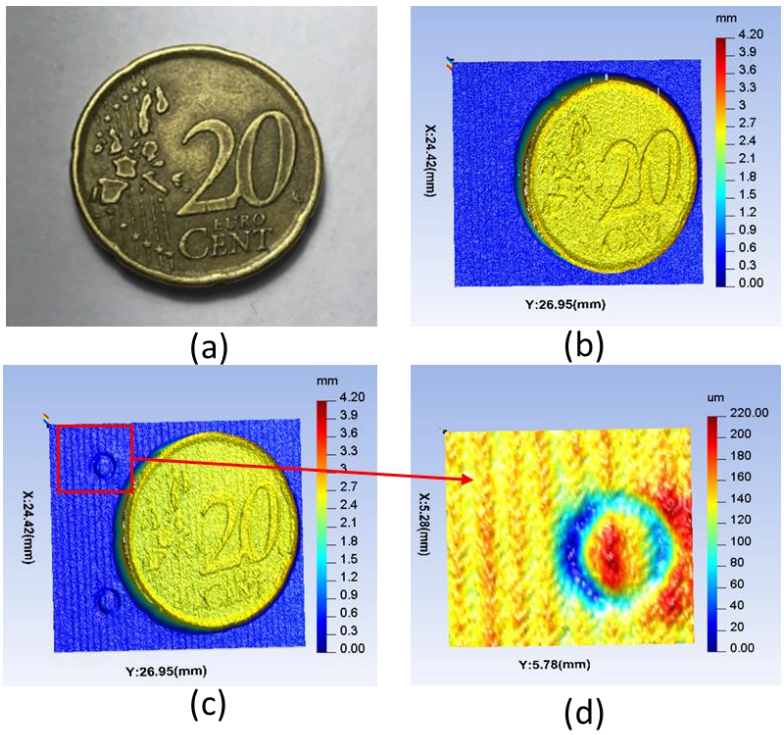

Figure 3. 27 A twenty-cent coin and 3D reconstruction results. (a) Photograph of the coin; (b) 3D measurement results of the coin after corrections. (c) 3D measurement results of the coin before corrections (b) Zoom in the error

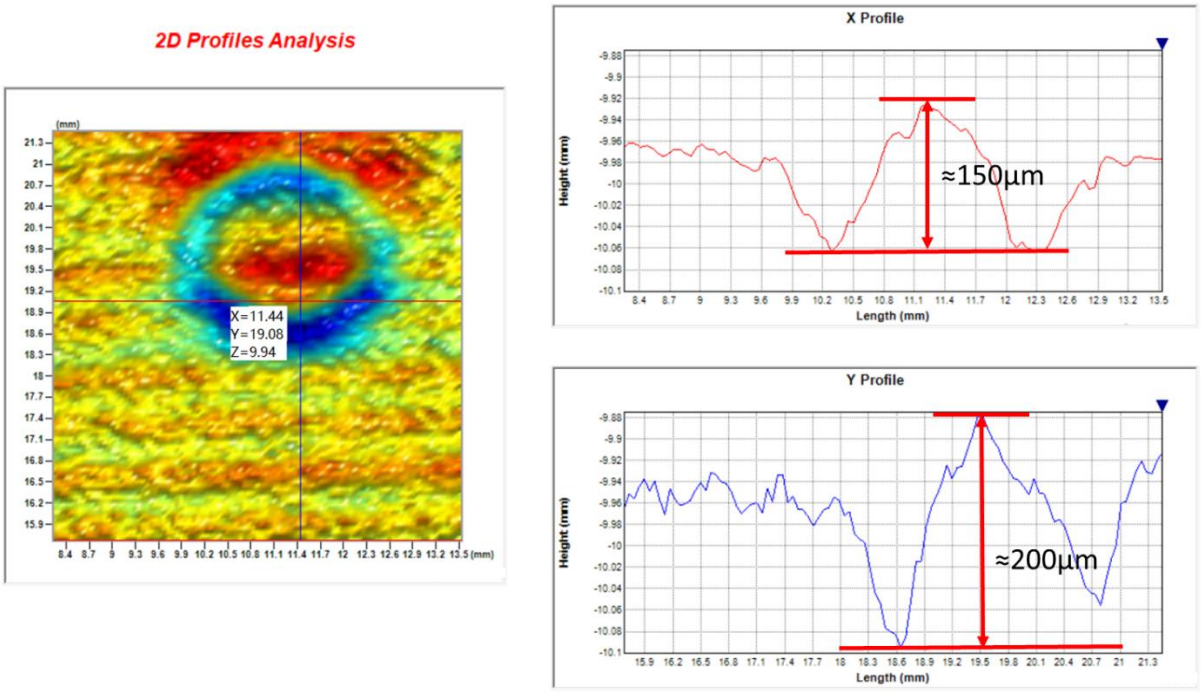

Figure 3. 28 The 2D profile of the measurement error because of ring effect.

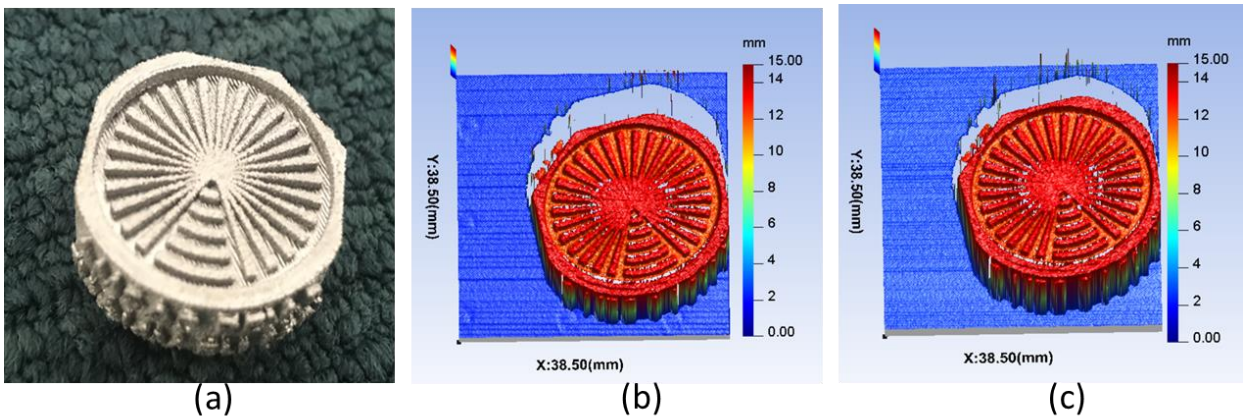

Figure 3. 29 Printed metal sample and 3D reconstruction results. (a) Photograph of tested printed sample (b) Areal map of tested printed sample before corrections (c) Areal map of tested printed sample after corrections

An Ebeam AM printed metal sample was measured by the fringe projection system as shown in Figure 3.29(a). The printed metal part with radial grooves and ridges is used for evaluating the manufacturing resolution. The measured results were consistent

with the manufacturing resolution. Comparing results with the proposed method and without corrections method, shows that the ring effect was eliminated, the measurement error of the rings area has been improved by 150 µm to 200 µm.

3.5.3 Nonlinear effect calibration

Fringe projection system have a nonlinear effect that originates from the digital projector and the camera called the gamma effect. The gamma effect is nonlinear which will bring nonlinear errors and phase errors to the system. It is demonstrated as a high harmonic effect in the fringe projection system. A more than five-step phase-shifting algorithm would reduce this nonlinear effect. However, it will also decrease measurement speed when using more than five steps in the phase-shifting algorithm. Therefore, it is important to calibrate the nonlinear effect.

A projection system uses sinusoidal fringe patterns to calculate phase information. A series of straight fringe patterns with different spatial frequencies are generated by the computer and projected onto an object surface through the DLP projector. Concerning the different heights of the measured object, these straight fringe patterns will be deformed. The CCD camera captures these deformed fringe patterns from an angularly displaced viewpoint compared with the standard fringe patterns and the images are saved for pos-processing. Because of the nonlinear effect, high harmonics occur to the captured fringe patterns. Gamma translation equation is as follows:

$$Y = (x + esp)^{\gamma} \tag{3.16}$$

where the value range of x and y are from 0 to 1. The term of esp is the compensation coefficient. γ is the gamma coefficient. γ can change the contrast ratio of different grey value level. The value of γ determines the mapped relationship between the input intensity and the output intensity.

When $\gamma > 1$, output intensity will enhance the contrast ratio of high light level.

When $\gamma < 1$, output intensity will enhance the contrast ratio of low light level.

The real projection system relationship between input intensity and output intensity is a nonlinear gamma effect and the situation is $\gamma > 1$ as shown in Figure 3.30. Therefore, an inverse compensation is need.

The input intensity can be illustrated with Equation 3.17. The ideal intensity output is illustrated in Equation 3.18. However, the relationship between the input intensity and the real output intensity is illustrated in Equation 3.19. The parameter of gamma-β accounts for system errors and phase errors for the measurement system. The relationship between input intensity and output intensity are shown in Figure 3.30.

$$I_{in}(x,y) = I_{DC}(x,y) + I_m(x,y)cos\,[\varphi(x,y) + \alpha(x,y)] \qquad 3.17$$

$$I_{out}(x,y) = I_{DC}(x,y) + I_m(x,y)cos\,[\varphi(x,y) + \alpha(x,y)] \qquad 3.18$$

$$I_{out}(x,y) = I_{DC}(x,y) + I_m(x,y)cos\,[\varphi(x,y) + \alpha(x,y)]^{\beta} \qquad 3.19$$

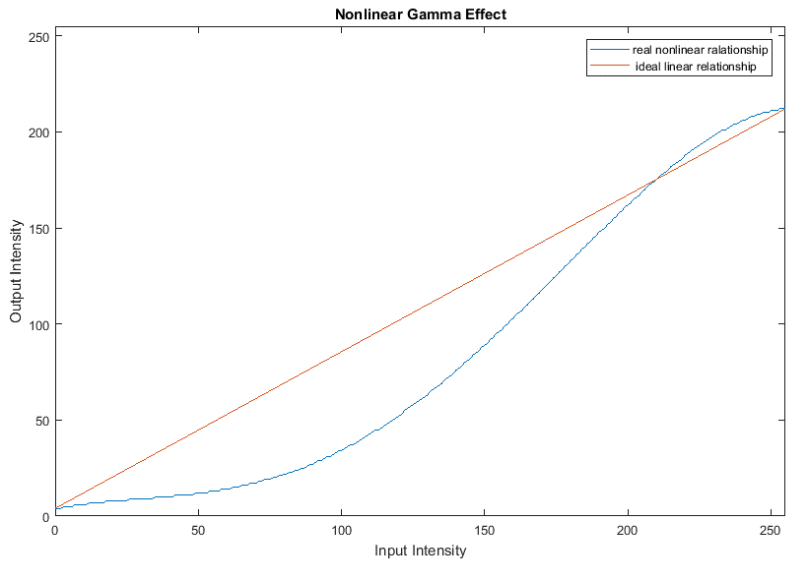

Figure 3. 30 The relationship of input intensity and output intensity

The red line is the ideal linear relationship and the blue line is the real nonlinear relationship between input intensity and output intensity. Before system calibration,

this nonlinear gamma effect should be calibrated and compensated through an intensity lookup table (LUT).

The main idea to solve this problem is to find the real relationship between input intensity and output intensity. Calculating the inverse function of the relationship between input intensity and output intensity generates a LUT to compensate for the nonlinear gamma errors. After system calibration, changing input intensity via LUT yields the corrected intensity to give a linear relationship between input intensity and output intensity.

520 gray map images were generated by Matlab program whose intensity changes from 0 to 255. The projector projects these images onto a calibration board surface and the camera captures the images on the board. The intensity of a selected square area of each captured image is calculated. Then series of the real output intensities are obtained by using Equation 3.19.

3.6 Deployment

3.6.1 Hardware and system

The system consists of a computer, a CCD camera, and a projector. The CCD camera is an industrial camera (model evo12040MBGEB as shown in Figure 3.31(a)) from SVS with a resolution of 3016x4016 pixels. It supports external and internal triggers. The projector is an industrial digital projector (Light Crafter model 4500 as shown in Figure 3.31(b)) with a resolution of 912x1140 micromirror array. The resolution requirement of the AM inspection is 50 µm. The field of view is 200mm by 200mm. The working distance is 400mm. The focal length of the lens can be calculated by using the following equation:

$$\frac{1}{f} = \frac{1}{OD} + \frac{1}{ID} \tag{3.20}$$

where, f is lens focus, OD is object distance and ID is image distance. Therefore, the lens of the camera is chosen 35mm in this experiment.

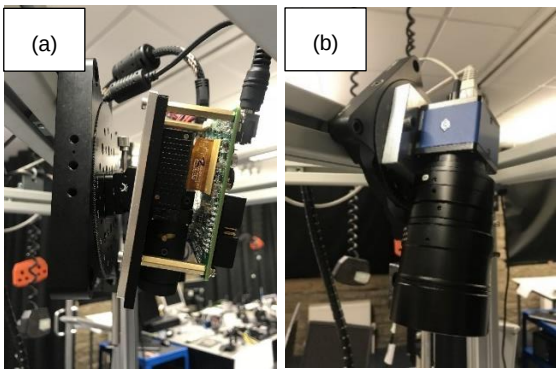

Figure 3. 31 Hardware of fringe projection system (a) DLP projector (b) CCD camera

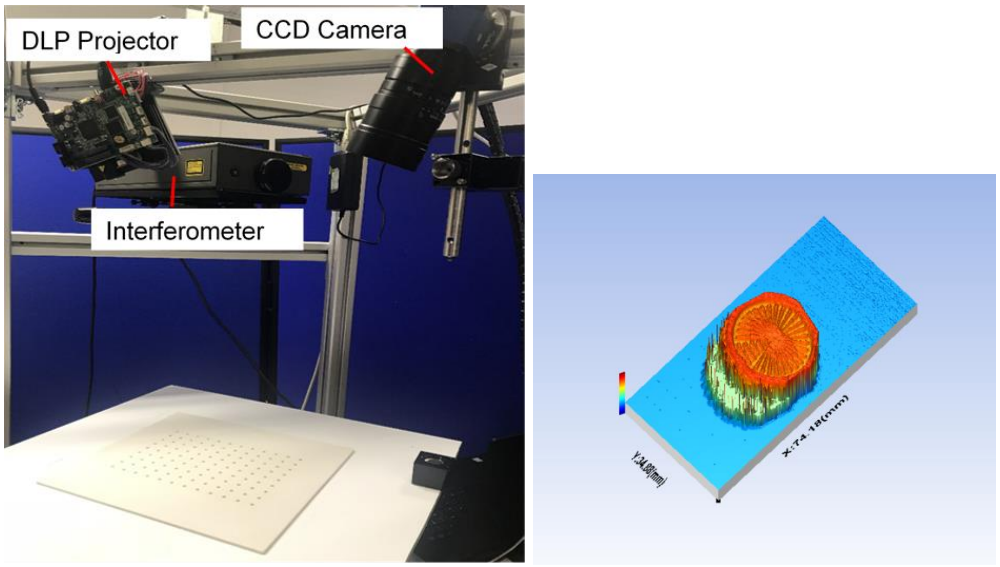

(a) (b)

Figure 3. 32 Fringe projection system with an interferometer (a) Prototype 1 system (b) Measurement result of a 3D-printed part

A fringe projection system (Prototype 1 as shown in Figure 3.32(a)) was built on an aluminum steel frame whose size was the same as AM machine build volume. The interferometer, the camera, and the projector were fixed for system calibration. The system was calibrated and the measurement result of a 3D-printed part is shown in Figure 3.32(b). A 2nd prototype measurement system was then deployed to assess the 3D geometry of a prototype powder delivery system. In this case the fringe projection

system was combined with a separately developed powder delivery system to assess the feasibility of the measurement set up, as illustrated in Figure 3.33(a). Powder bed was inspected by the system and the results were shown in Figure 3.33(b).

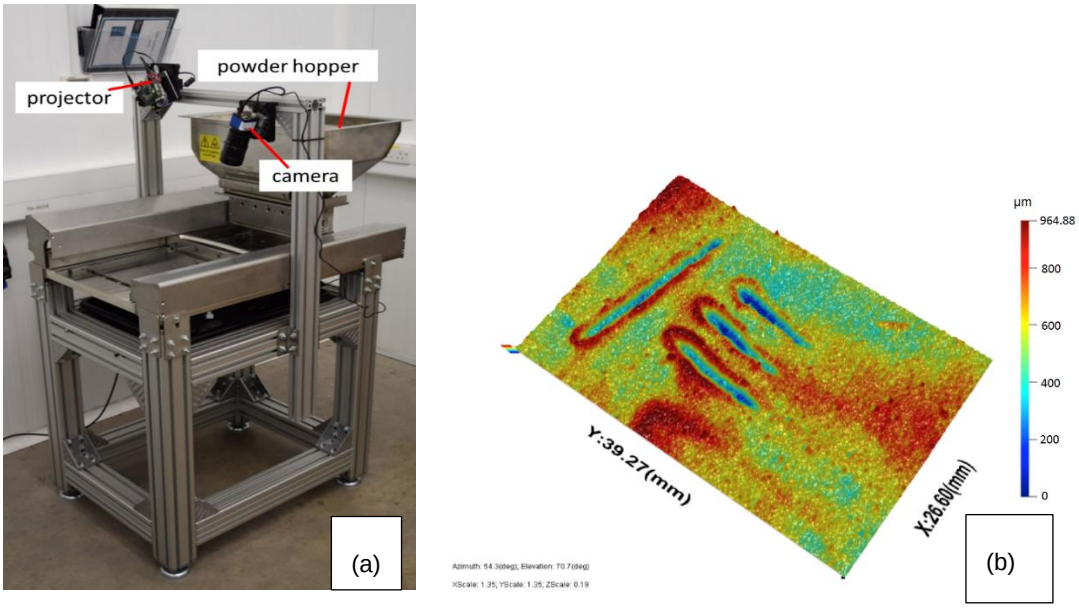

Figure 3. 33 Powder delivery system with fringe projection system (a) Prototype 2- implemented on powder delivery system (b) exemplar measurements

Following successful implementation of prototype 2, a full implementation of the inspection system was carried out on a commercial EBM machine (prototype 3 as shown in Figure 3.34). The position of the camera and projector outside of the vacuum build chamber with the viewing ports underneath the camera and projector are clear in the figure. The AM machine has a vertical translation stage for positioning the powder bed and the finished parts with high moving accuracy using an independent scale, therefore this moving distance is adopted instead of interferometer measurement results of prototype 1 and 2 during depth calibration.

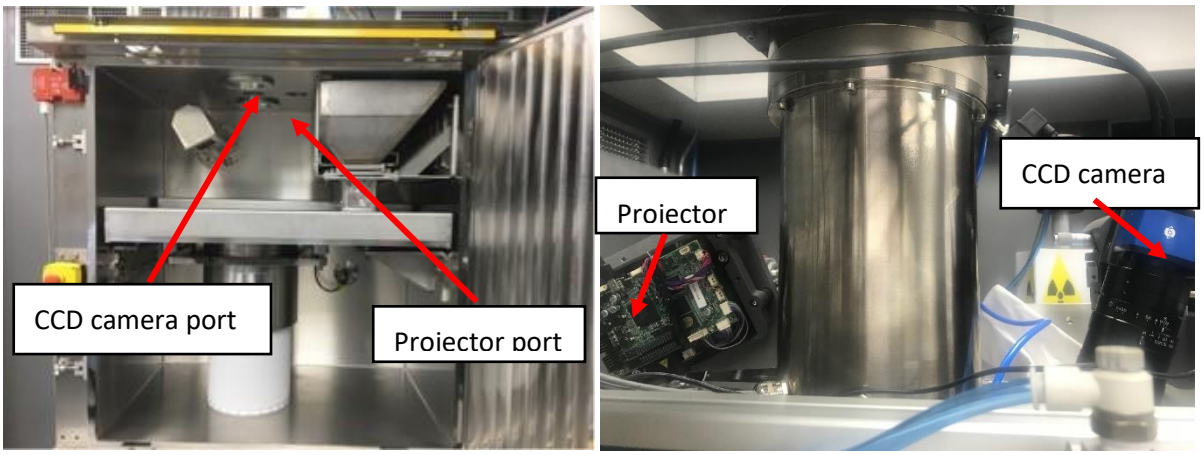

Figure 3. 34 Prototype 3 system with inspection system in a new EBM machine

Prototype 1 was used to simulate and investigated the calibration algorithms. The fringe projection system (prototype 2) detected the state of the simulated powder bed in a powder delivery system without melting. Prototype 2 also verified the reliability and the detection capability of the fringe projection system. Prototype 3 is the prototype EBM machine. The fringe projection system measured the powder bed during a typical build process, (under vacuum and high temperature in a real build cycle).

3.6.2 Software

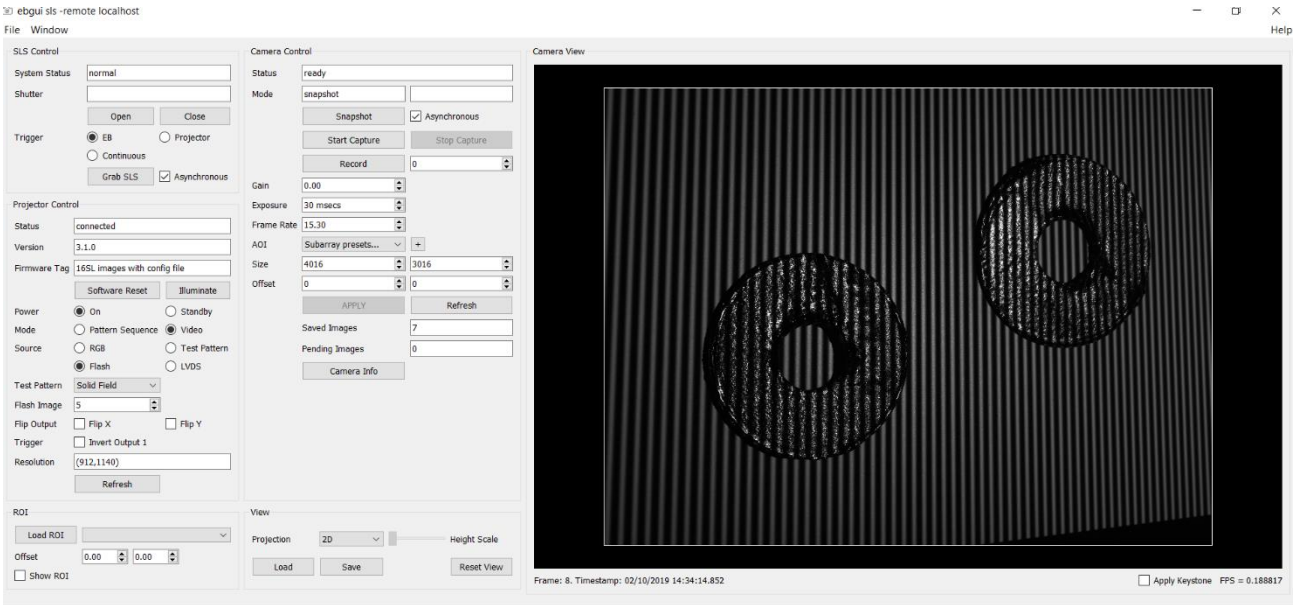

Figure 3. 35 The control software of fringe projection system

Figure 3.35 shows the measurement control software module of the fringe projection system, which is part of the AM operation software. The functions include the system control module, the projector parameters setting module, the camera parameters setting module, and the 3D measurement display module. 3D measurement results can be shown in the display window. The procedure of system calibration is processed by Matlab.

3.7 System evaluation

In order to demonstrate the system performance, parameters including measurement, precision, repeatability reliability, and resolution (the minimum measurement depth), were evaluated.

3.7.1 Precision and resolution along transverse direction

During the calibration process, four test positions were used as known heights which are determined by the interferometer. Based on the four test positions, comparison with the nominal distance between each centre points and the measured distance is the transverse direction accuracy. Table 3.4 shows the results.

Table 3. 4 Details of the accuracy and precision along transverse direction

Directions	Nominal distance between each centre points (mm)	Number of centre to centre measurements	Mean measured distance (mm)	Mean absolute errors (measurement accuracy) (mm)	Standard deviation (Precision) (Units: mm)
X	15.0007	320	15.0228	0.0228	0.0467
Y	15.0009	308	14.9971	0.0029	0.0382

The precision along transverse direction can be represented as follows:

$$\text{Error} = \frac{\sum_{n=1}^{N} M_n}{N} - D_{actual} \qquad 3.21$$

where Error refers to the mean absolute errors, M_n is the measured distance between each centre points, N is the number of the centre point to centre point measurements (N equals 320 in x-direction and 308 in y-direction respectively), D_{actual} is the actual distance between each centre points. Figure 3.36 shows the measurement precision and error range in X and Y directions.

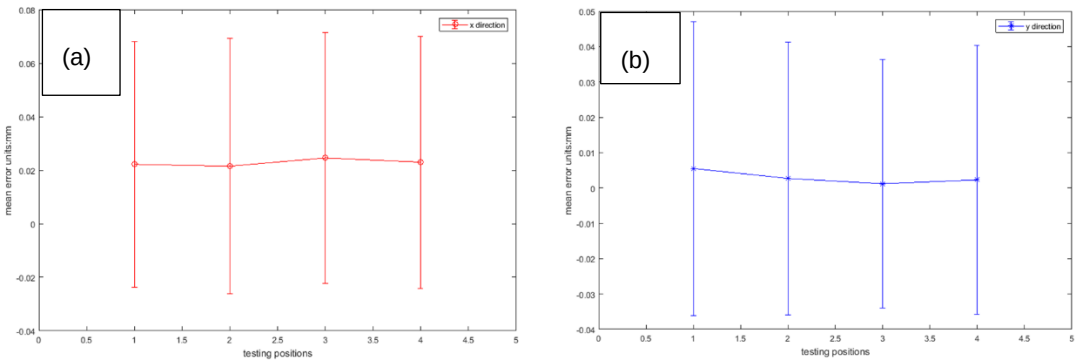

Figure 3. 36 Measurement accuracy and error range in X and Y directions (a) X direction (b) Y direction

The standard deviation is used to evaluate the measurement precision, which can be calculated based on the following equation:

$$\sigma = \sqrt{\frac{1}{N}\sum_{n=1}^{N}(M_n - \frac{\sum_{n=1}^{N} M_n}{N})^2} \qquad 3.22$$

where σ is the standard deviation. The measurement accuracy and repeatability of x-direction are 0.0228mm and 0.0467mm respectively. The measurement accuracy and repeatability of y-direction are 0.0028mm and 0.0387mm respectively. It can be clearly seen that the measurement accuracy in the Y direction is higher than that in the X direction because there was an angle between the optical axis of the camera and the normal line of the calibration plate when the camera operating. Because of the angle between the optical axis of the camera and the normal line of the calibration plate, a perfect circle becomes an ellipse in the camera view. The centre of the ellipse

extracted in the X direction deviated from the true centre of the circle, while the deviation between the extracted centre of the ellipse and the true centre in the Y direction was small, so the accuracy in the Y direction is higher.

The transverse resolution is defined as the ratio of the field of view and the resolution. The resolution of the used camera is 4016 by 3016. Therefore, the transverse resolution is 0.0859mm and 0.0810mm in x and y directions, respectively.

3.7.2 Precision and resolution along z direction

Table 3. 5 Details of the accuracy and precision along depth direction

Position(mm)	Mean measured distance	Mean absolute error (measurement accuracy)	Standard deviation (precision)
-3.4945	-3.5042	0.0097	0.0063
-1.4940	-1.4947	0.0007	0.0070
1. 5030	1.5000	0.0030	0.0072
3.5011	3.4832	0.0179	0.0050
Mean for 20 times measurement	One point for mean 20 times measured distance		

The height value of the powder can be calculated based on Equation 3.7. After depth calibration, the coefficients of a_0, a_1, and a_n can be calculated. The accuracy of the coefficients affects the accuracy of the measuring system. During the calibration process, four testing positions were used as known heights determined by using the independent interferometer. At each position, the camera captured the projected fringe patterns, and calculated the absolute phase. Based on the calibrated coefficients and the absolute phase, the measured height of the object can be acquired. System mean absolute error can be acquired by comparing the value measured from the interferometer with the height measured from the system. The measured distance obtained by the interferometer was taken as the ideal value. System repeatability and

reliability can be evaluated by calculating the standard deviation. After series of experiments, the measurement accuracy and precision of z-direction are 0.0179mm and 0.0072mm, respectively. Table 3.5 shows the results.

Figure 3.37(a) is the measurement relationship between the fringe projection system and the interferometer. Figure 3.37(b) is measurement accuracy and error range in Z-direction, which compared with the measurement results from the interferometer. Figure 3.38 shows the four testing positions measured by the fringe projection system.

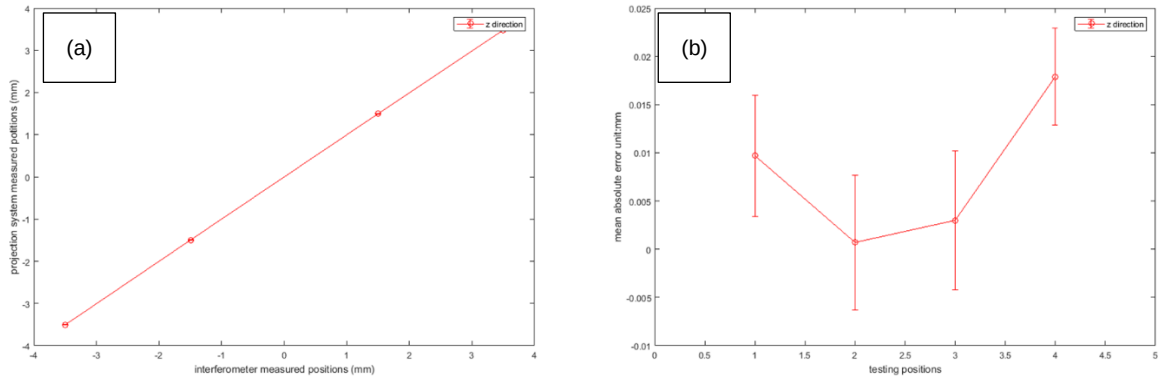

Figure 3. 37 Error range compared with interferometer and depth evaluation results (a) the measurement relationship between the fringe projection system and the interferometer (b) measurement accuracy and error range in Z directions

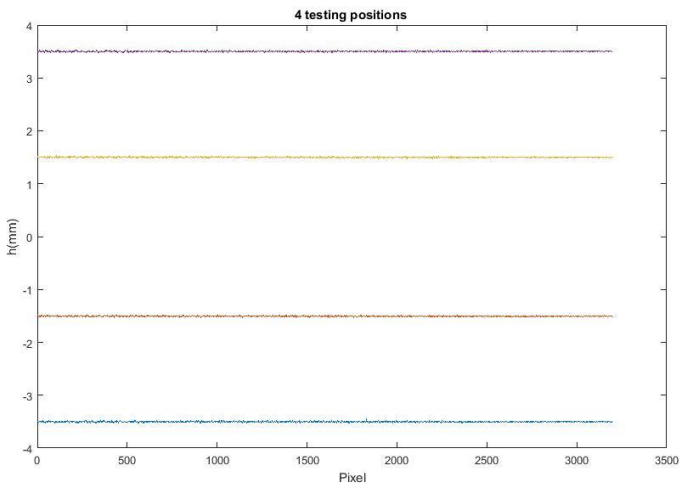

Figure 3. 38 The profile of four testing positions that are measured by fringe projection system

For the present fringe projection system, a series of sinusoidal fringe patterns are utilized to analyse the phase information. One sinusoidal signal with one period is demonstrated in Figure 3.39. λ is the wavelength of a period. The intensity from the highest to the nearby lowest is divided into 2^N grey levels. N of 2^N is the type of pattern that equals to 8 bits. Therefore, the half wavelength can divide into 256 grey levels. The following Equation 3.23 demonstrates the relationship between the wavelength and the depth.

$$\frac{\Delta\phi}{\Delta h} = \frac{2\pi}{\lambda} \qquad 3.23$$

where $\Delta\phi$ is the difference of the absolute phase value between different height levels of an object. Therefore, the minimum resolvable depth can be calculated based on Equation 3.24

$$\mathrm{Min}h \geq \frac{\lambda}{2\times 2^N} \qquad 3.24$$

where λ is the real wavelength along the depth direction which can be calculated from Equation 3.23. The theoretical minimum resolution of the present system is 0.0129 mm which represents the minimum resolvable vertical distance.

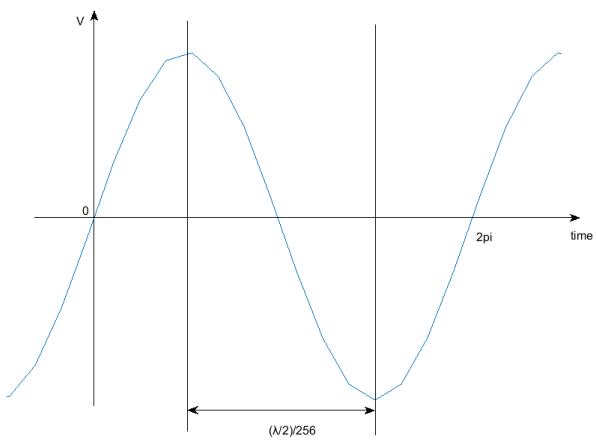

Figure 3. 39 The profile of one sinusoidal signal with one period

A set of standard ceramic steps gauges as shown in Figure 3.40(a) was measured with the proposed measurement system as illustrated in Figure 3.40(b). The measured results obtained by the inspection system were compared to the standard step gauge values, as listed in Table 3.6. The values listed in the first row are the distance between each step surface. The maximum absolute error is 10.2 μm. Therefore, it was assumed that the system can achieve a vertical resolution below 20 micrometers and a standard deviation around 15.8 μm on a flat plane when results were obtained from 10 capturing positions to optimize system parameters, and these results are consistent with the simulation results. The accuracy of the inspection system is improved from 32.5 μm to 15.8 μm by the improved calibration method in the circle ring area.

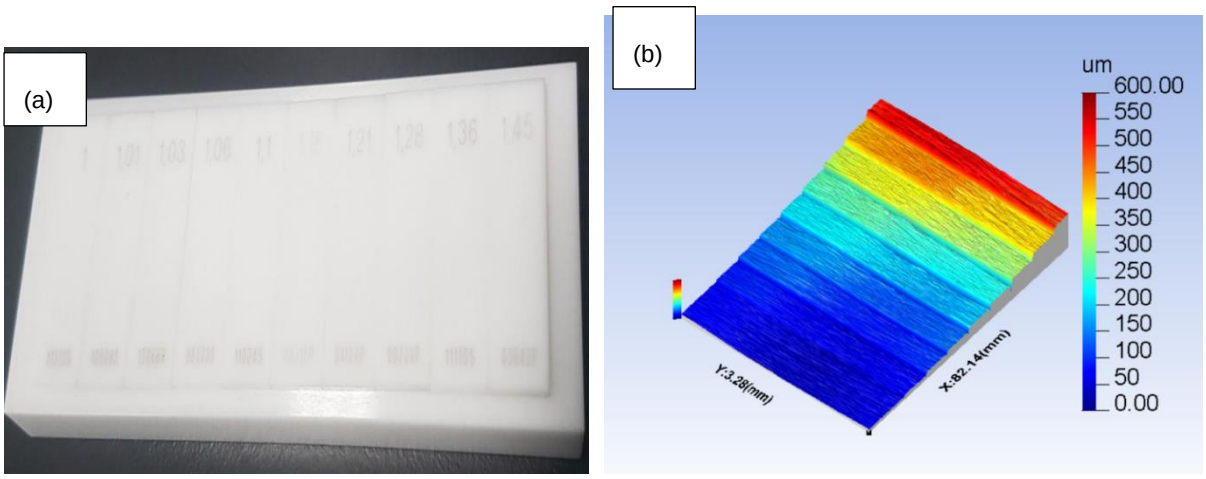

Figure 3. 40 Illustration of the standard ceramic step and measured 3D shape data prototype 2 (a) Photograph of the standard ceramic step (b) the measured 3D shape

Table 3. 6 The experimental results on the measured step (Unit: μm)

Standard distance/μm	90	80	70	60	50	40	30	20	10
Measurement distance/μm	102.0	86.9	75.1	62.7	50.5	37.6	31.7	19.3	8.1
Absolute error/μm	10.2	6.9	5.1	2.7	0.5	2.4	1.7	0.7	1.9

3.8 Experimental

Twenty-four sinusoidal fringe patterns having optimum fringe numbers of 100, 99, and 90 were generated by the software and sequentially projected onto the inspected surface. Patterns on the powder were modulated by the geometric form of the powder surfaces and then captured by the camera. Positions of the camera and the projector were fixed, which means the parameters of the system would not be changed. After the vertical parameters of a_n and transverse parameters of a_0, b_0, c_0, a_1, b_1, c_1 were calibrated by using the method described above, the 3D surface form of the powder surface could be assessed by the developed system.

Exemplar results from the new EBM machine are shown in Figure 3.41 and Figure 3.42. Figure 3.41 shows a set of partially built rectangular tensile test parts within the powder bed where edge thermal swelling is clear, also evident is the edge of the pre-sintered powder region. Figure 3.42 shows an example of excessive powder delivered due to powder rake damage. All these images were recorded on the EBM machine during a typical build. Figure 3.43 shows the orthogonal 2D extracted profiles across the excessive powder delivery region. In this case, the height of the edge is several millimeters above the base powder layer. All these measurements are used as feedback to control the build process.

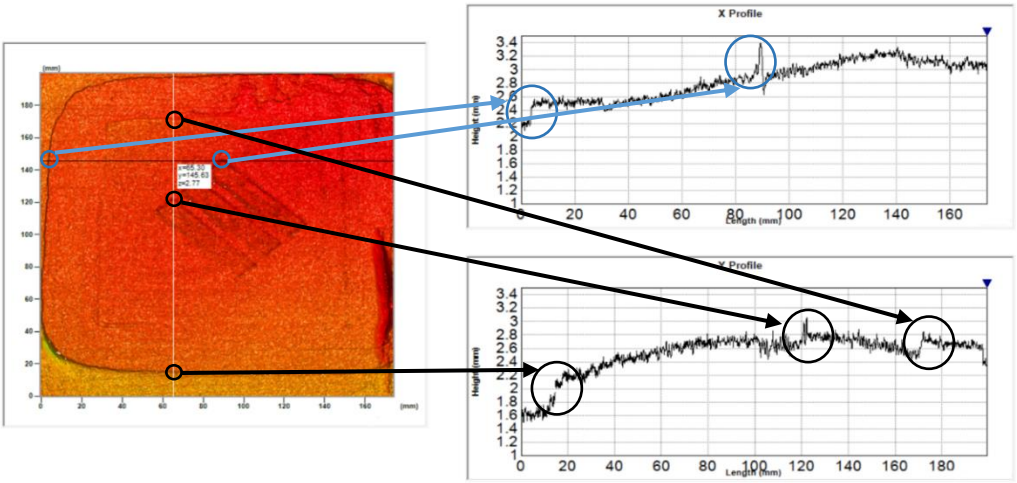

Figure 3. 41 Partially built parts within powder bed post a single build cycle

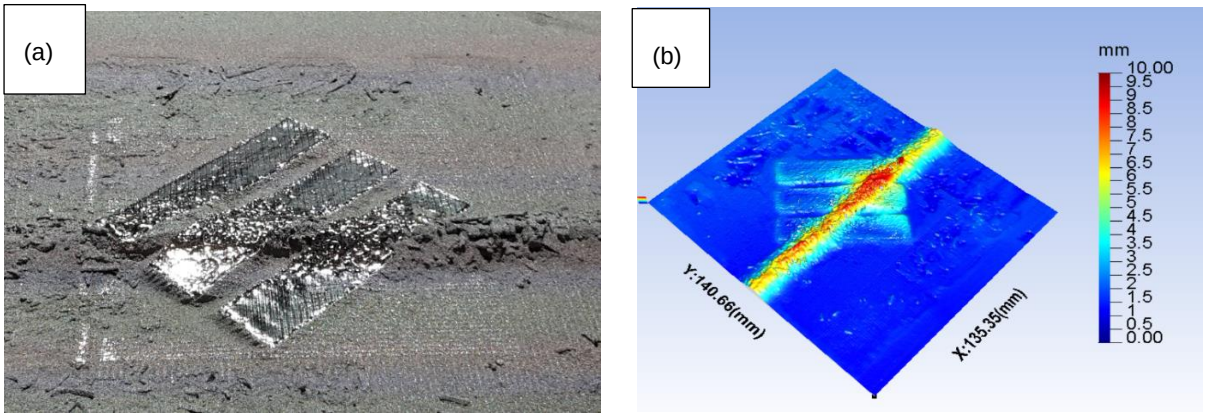

Figure 3. 42 Excessive powder delivery on top of partially build parts (a) Photograph of tested powder bed (b) Areal map of tested powder bed

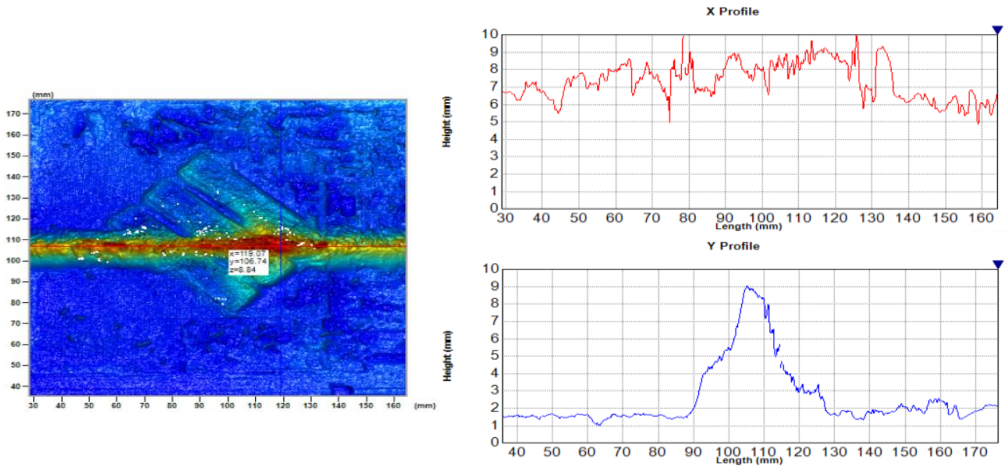

Figure 3. 43 Areal map and extracted profiles of the excessive powder delivery (due to rake damaged) on top of partially build parts

In terms of process control, when the detected powder height value is over a defined threshold, the building process can be stopped and the machine operator notified. The height level to trigger the process stop can be determined as part of a process control study. Figure 3.44 shows a series of in-situ measurement results during a part build process. The fringe projection system regularly inspected the powder bed every 15 layers and then adjusted the process according to the measurement results. Figure 3.44 shows the measurement results after powder delivery of layers 45(a), 60(b), 75(c), 90(d), 105(e) and 120(f), respectively. Figure 3.44(a) (d) (f) show the powder delivery after was smooth enough to carry on with the build. While Figure 3.44(b) (c) (e) show that there was lack of powder due wake effect of the part swelling, the build would not carry on until the powder bed surface was smooth enough after powder redelivery. The results show the fringe projection system has the capabilities to detect part thermal swelling, excessive powder delivery and other powder bed defects/effects.

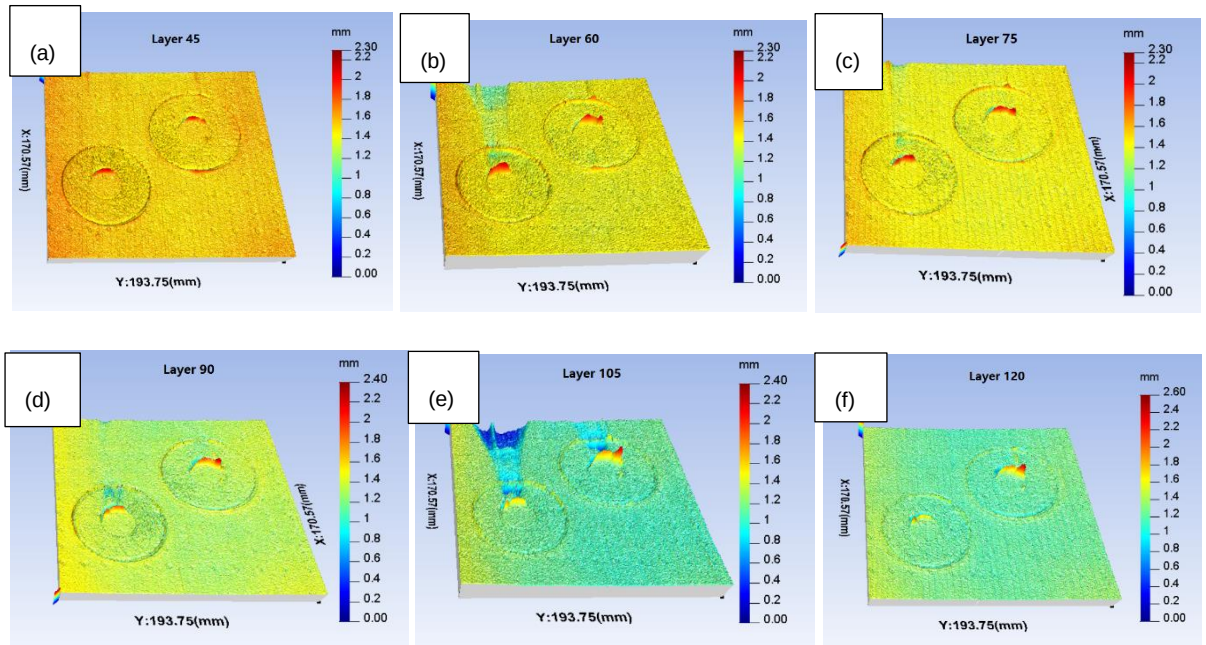

Figure 3. 441 3D measurement results of the building process

A set of low-quality finished parts manufactured by the AM machine are shown in Figure 3.45(a) these are the same parts as shown in Figure 3.44. A contact measurement result captured using a Romer Absolute Arm as shown in Figure 3.45 (b) and is shown in comparison to one of the final in-process layer measurements as shown in Figure 3.45(c). The measurement is not taken in the same location but highlights the capability of the in-process system in detecting geometrical elements of the AM surfaces.

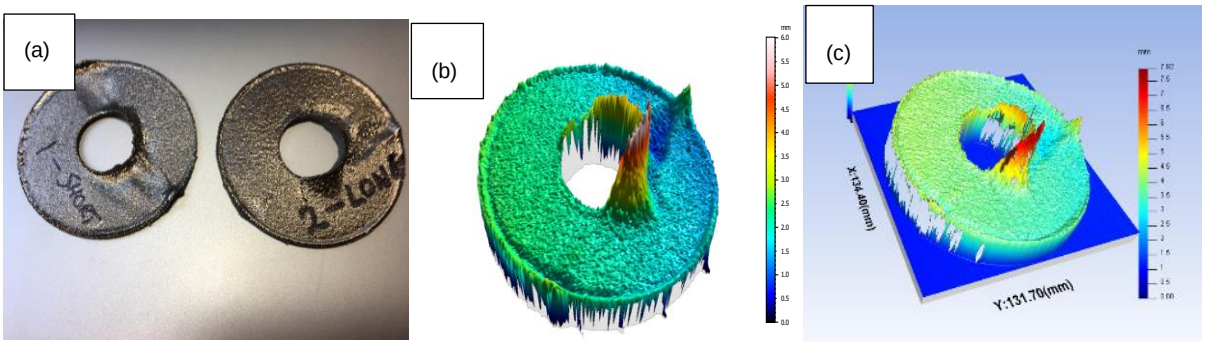

Figure 3. 45 A finished part measurement result

3.9 Summary

In this chapter, an in-situ monitoring technique was developed to facilitate inspection of the powder bed of an EBM machine by using a fringe projection technique. 3D measurement of powder delivery feedback signals that can ensure the accuracy of powder bed before melting and part geometry post melting, should improve process knowledge and facilitates process control. A novel surface fitting algorithm was developed in the system calibration protocol to improve measurement accuracy and vertical resolution, this reduced the influence of phase error and random noise. Another novel system calibration method was investigated. The reference coordinate system was established by using the whiteboard in the depth calibration process. By comparing the results before and after the correction, the phase error caused by the ring is eliminated, and more accurate depth calibration results are obtained by this

method. The simulated and actual experimental data have shown the validity and feasibility of the proposed inspection technique. After the calibration of the fringe projection system, the state of the powder bed before melting and part geometry after manufacturing can be detected more realistically. Experimental results show the fringe projection system has the capabilities to detect part thermal swelling, excessive powder delivery, lack of powder, and other powder bed defects/effects, which offers improved manufacturing accuracy and control during the manufacturing process. The system has been fully deployed on a commercial AM machine and control software integrated with the AM machine control. The measurement speed is around 2 secs during each measurement cycle. The presented system is fully integrated into the build cycles of the AM machine providing a “closed door”, high-speed measurement process. It is accompanied by a set of simple and economical hardware elements and is integrated into the machine control software. Compared to an expensive commercial 3D scanner such as a Zeiss or GOM scanner the system described here is fully adopted for continuous layer by layer measurement, does not require the built environment to be pumped down from vacuum, has a fast acquisition time, and has a fully integrated calibration protocol. The cost of the system presented in this thesis is a fraction of the cost of standard commercial scanner equipment.

Overall it is considered that the present in-situ measurement system could be implemented commercially on both EBM and SLM systems and could be integrated with the machine control to act as a go/no go gauge for powder delivery or to modify powder dosage and dispensing blade control.

Chapter 4 Developed structure light system for high dynamic range surface based on machine learning

This chapter provides a novel method of the fringe projection technique for inspecting shiny surface or surfaces with a high dynamic range (HDR). This would be essential for measuring printed surfaces after melting/solidification. This chapter investigates a solution to the need by applying machine learning technique to the measurement task as applied to AM parts. The chapter is divided into five sections: section 4.1 is an introduction of HDR measurement by fringe projection technique in AM. Section 4.2 is the 3D measurement principle of the HDR fringe projection technique. Section 4.3 is the training and classification method. Section 4.4 is the measurement result. Section 4.5 is a summary.

4.1 Introduction

Chapter 4 introduced the EBAM system and the fringe projection system for powder delivery inspection. The process proceeds by layer-by-layer melting and re-solidification of metal powder utilising an electron beam energy source. Following solidification of the build layer, the surface becomes “shiny” with high reflectivity which makes in-process inspection of the surface of the build layer using fringe projection, difficult. To address this issue, a modification of the fringe projection technique needs to be investigated to measure the 3D topography of high dynamic range surfaces on a layer-by-layer basis within the EBAM machine. Some researchers have conducted a series of studies on this issue and the solutions are based on three categories. The first category is the multi-exposure method. The second category is to eliminate the reflective effect, which is essentially equipment-based techniques facilitated by adjusting parameters or using special devices. The third category is based on RGB

colour channels to separate saturated pixels from images. These approaches are reviewed in chapter 2. Following the first category, HDR measurement based on machine learning is investigated.

In this chapter, a new method to solve the problem of HDR measurement in AM processing using a Machine Learning algorithm is investigated. Machine learning algorithms can be roughly divided into three categories: supervised algorithms, unsupervised algorithms, and reinforcement algorithms [166]. There are some basic machine learning algorithms like: Linear Regression[167], Support Vector Machine (SVM)[168], K-Nearest Neighbors (KNN)[169], Logistic Regression[170], Decision Tree[171], K-means[172], Random Forest[173], Naive Bayes[174], Dimensionality reduction [175], Gradient Boosting[176]. Among them, SVM, Naive Bayes, Decision Tree belong to supervised learning. This thesis studies a classification method SVM. Some typical classification algorithms can be summarized as following. Logistic regression is a binary classification method, and the basic algorithm is derived from linear regression. Logistic regression maps the prediction result between 0 and 1 by the Logistic function (the Sigmoid function), therefore, the predicted value can be seen as the probability of a certain category. The advantage of Logistic regression is that the output has a good probability interpretation, and the algorithm can be regularized to avoid overfitting. Another classification method is the decision tree. A decision tree is a prediction model. Each node in the tree represents an object, and each bifurcation path represents a possible attribute value. Each leaf represents the value of the object represented by the path from the root node to that leaf node. The decision tree has a single output. For example, a typical algorithm is random forest. Its advantage is that it has considerable robustness and scalability to abnormal data. The disadvantage is

that it is unconstrained and a single tree tends to overfit. Deep learning is one of the artificial neural network algorithms, which is often used to solve classification problems. Deep learning algorithms are the development of artificial neural networks. Many deep learning algorithms are semi-supervised learning algorithms, which are used to deal with large data sets with a small amount of unidentified data. Common deep learning algorithms include Restricted Boltzmann Machine (RBN), Deep Belief Networks, Convolutional networks, Stacked auto-encoders[177]. The disadvantage is that the deep neural network approach needs a lot of data to train. The k-Nearest-Neighbours (KNN) algorithm can be used for classification. The principle is using the nearest neighbour (k) to predict the unknown points. K value is a key factor in the prediction accuracy, therefore, it is very important to measure the weight of the neighbours. The weight of the near neighbours is more important than that of the distant neighbours. The disadvantage of KNN algorithm is that it is very sensitive to the local data. It needs large the amount of calculation, and it is necessary to normalize the data so that each data point is in the same range. In this chapter, the support vector machine (SVM) algorithm is investigated. In the present study, the SVM algorithm is used to classify and predict the inspection surface set up parameters, which increases the intelligence of the inspection system. SVM can model nonlinear decision boundaries using various nonlinear kernel functions. SVM also has considerable robustness against overfitting. After system calibration, the fringe projection system inspects the printed surface layer by adapting camera exposure time during AM surface inspection. The SVM algorithm is employed to reduce the measurement time compared with traditional methods. Only one grey level pattern is projected onto the test surface in order to predict the surface category and suitable exposure time. The fringe projection system realizes high-precision inspection, automatically identifies the measured surface category and

completes optimised in-situ high-speed measurement. The system has been implemented in a commercial EBAM machine. The correct recognition rate of the inspection system was high. The results showed that the system had the ability to simultaneously measure both powder bed and metal surfaces.

4.1.1 Saturation issue in AM inspection

With the recent advancements in powerful computers, mobile devices, and cloud computing, structured-light three-dimensional (3D) shape measurement technology has been applied in an increasing number of fields, including 3D video games, high-speed inspection, reverse engineering, quality control, and others [178], [179]. AM, as an advanced processing technology, has been widely adopted in recent years. Optical inspection techniques are widely employed for providing effective feedback in order to control the manufacturing process, which greatly improved the product quality during AM [1]. However effective implementation of structured light to in-process measurement within the AM process presents some difficulties. The primary challenge is based around the fact that the solidified metallic "built" surface is "shiny and highly reflective" whereas the surrounding unmelted powder is unreflective and diffuse. [**Error! Bookmark not defined.**]. The solidified shiny surface and diffuse powder bed need to be measured simultaneously using fringe projection technology, which usually results in intensity saturation (shiny surfaces) and data loss (dark surfaces) from the captured images as shown in Figure 4.1. Hence implementation of an effective in-situ simultaneous measurement approach for assessment of powder delivery and solidified "shiny" part quality is essential to improve manufacturing accuracy, enhance product quality and provide key information for process control. The intensity saturation is problematic whenever optical inspection technology especially structured light is used for measuring shiny surfaces, such as smooth metal surfaces or ceramic surfaces [180].

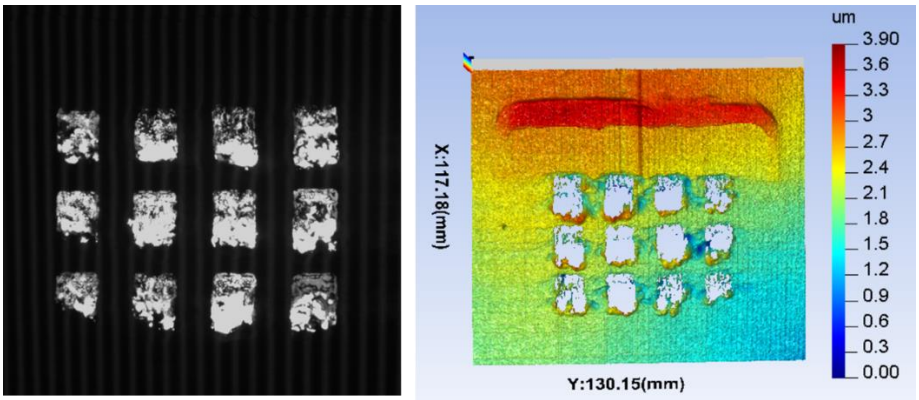

(a) (b)

Figure 4. 1 The saturation issue appears when the Ebeam melts the metal powder and the surface becomes shiny (a) Fringe pattern with saturation pixels (b) 3D data with saturation issue

An EBAM manufacturing/ inspection process flow diagram is shown in Figure 4.2, for full implementation of this approach it is a challenge for the optical fringe projection system to detect the state of the powder bed and the reflective metal surface simultaneously. The AM process is divided into two parts, as shown in the figure, in-situ detection, and post-processing inspection. During in-situ inspection, after process parameters are set, a layer of powder is delivered from a hopper. Then the fringe projection system inspects the powder bed to assess the powder surface if the surface is flat enough to carry on with the process. If the result seems “good”, the AM machine will continue with the build cycle, namely Ebeam melting. Otherwise, the power delivery will be repeated until the surface is smooth enough or the process is abandoned.

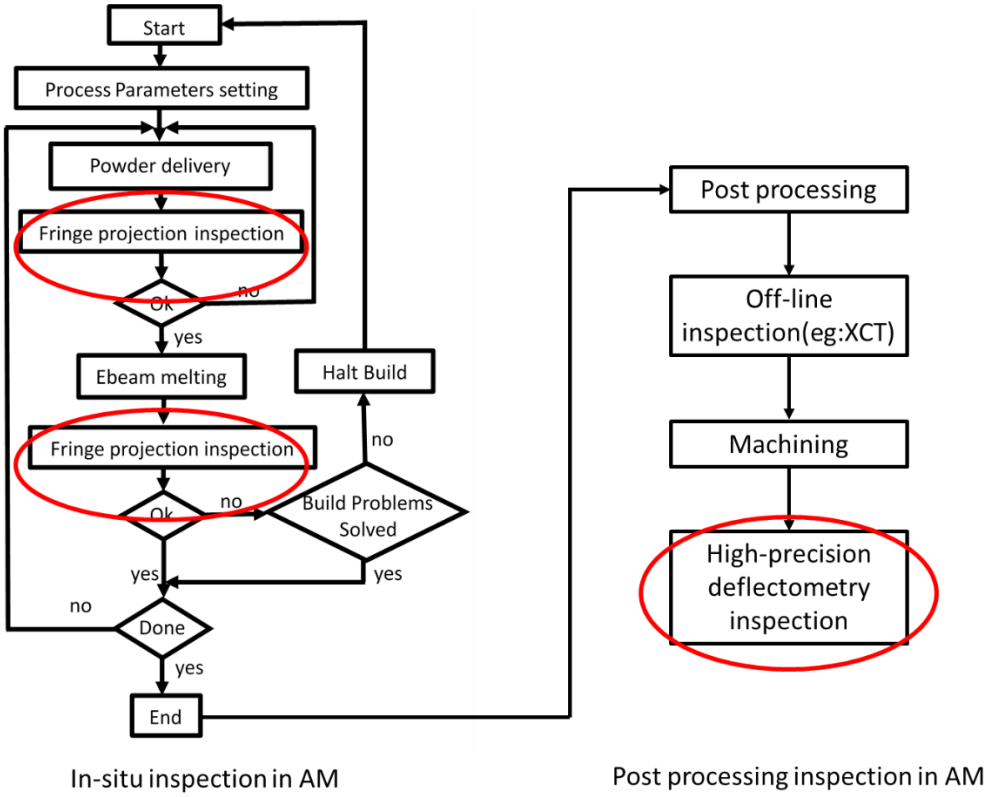

Figure 4. 2 A typical EBAM Manufacture and inspection flow chart of additive manufacturing system

After the powder fusion, the fringe projection system will inspect the printed part to detect planar and out of plane error. If no problems are detected or the problem can be resolved by changing build parameters the build will carry on, if a significant problem is detected i.e. the part build deviation is beyond a given threshold then the

build is halted. This whole process is repeated throughout the build cycle until the build is complete. Between powder delivery and melting, there are 4–5 seconds preparation time for preheating of powder on the build bed, the fringe projection system makes use of this time gap to inspect the powder bed so this will not increase the total time cost. After the EBAM melting cycle, the metal powder is solidified and the reflective characteristic of the solidified surface changes from diffuse to highly reflective. If the inspection parameters are as same as parameters of the powder bed, some data will be lost because of image saturation. This phenomenon results in the AM processing bed having a high dynamic measurement range requirement and hence poses issues when the system tests the powder bed surface and the resolidified metal. Such combined surface measurement is needed when establishing with precision the boundary of the resolidified layer.

4.1.2 Traditional HDR methods

A typical method for measuring high dynamic surfaces is the multiple exposure method. During measurement, the measured surface is captured using different exposures. After the fusion of multiple sets of data, the complete form data can be obtained. Figure 4.3 shows the different reflective properties of an EBAM manufactured “cross” shaped surface.

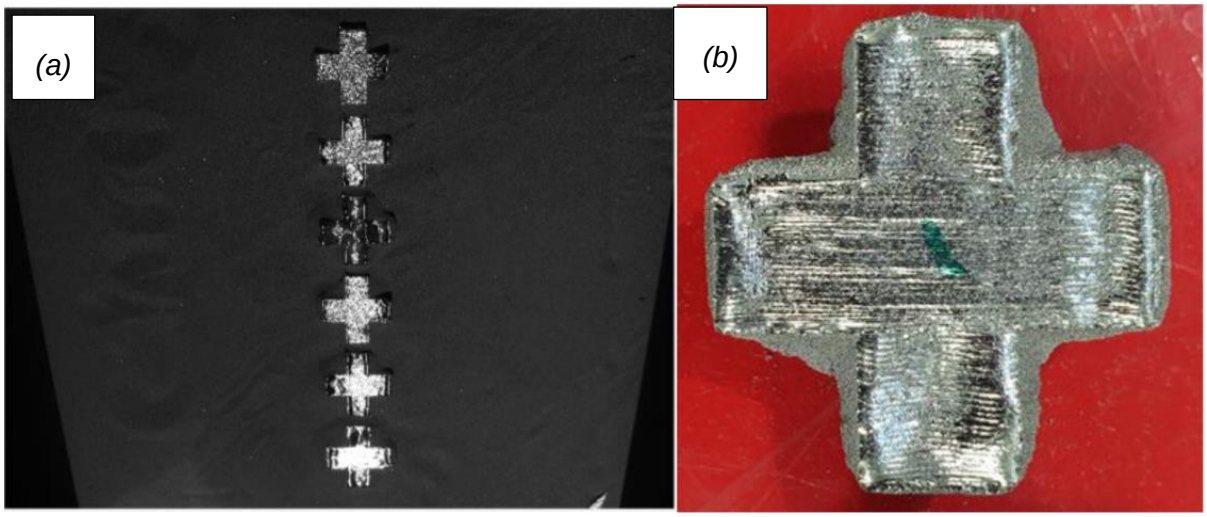

Figure 4. 3 The reflective properties of the metal surface

One of the manufactured ‘cross’ surfaces was photographed as shown in Figure 4.3 (b). The sinusoidal fringe patterns are projected to the surface and the camera captures the projected fringes 10 times with different exposure times, ranging from 5

ms to 100 ms. After multiple exposures, the results were collected. Then the 3D results were constructed as shown in Figure 4.4. Eight exposures were randomly selected: 5 ms, 7.5 ms, 10 ms, 15 ms, 20 ms, 25 ms, 50 ms, and 100ms. The inspection accuracy of the fringe projection system using multi exposures is used to capture this data can be found in [**Error! Bookmark not defined.**].

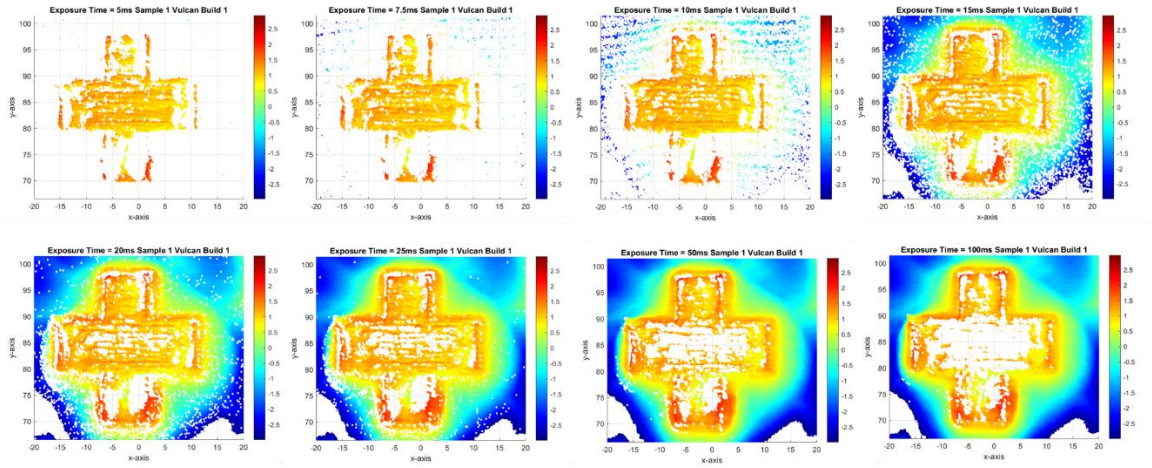

Figure 4. 4 Multi exposures measurement results

This method increases the measurement time and the amount of data in the measurement process. The whole measurement time for this multi-exposure method is over 16 seconds. If multiple exposure measurements are applied for each layer, the measurement results can be obtained, but the manufacturing time is also increased significantly for a build cycle containing 1000's of layers. Through the analysis of the results of eight measurements, the data of 5 ms and 100 ms exposure were fused to obtain the maximum surface data. Figure 4.5(c) shows the fused results of two measurements with the exposure times of 5 ms (Figure 4.5a) and 100ms (Figure 4.5b). The height results are merged which consumes time and can still produce low-quality surface information. Therefore, an inspection method that can automatically predict suitable exposure time based on each printed surface is essential.

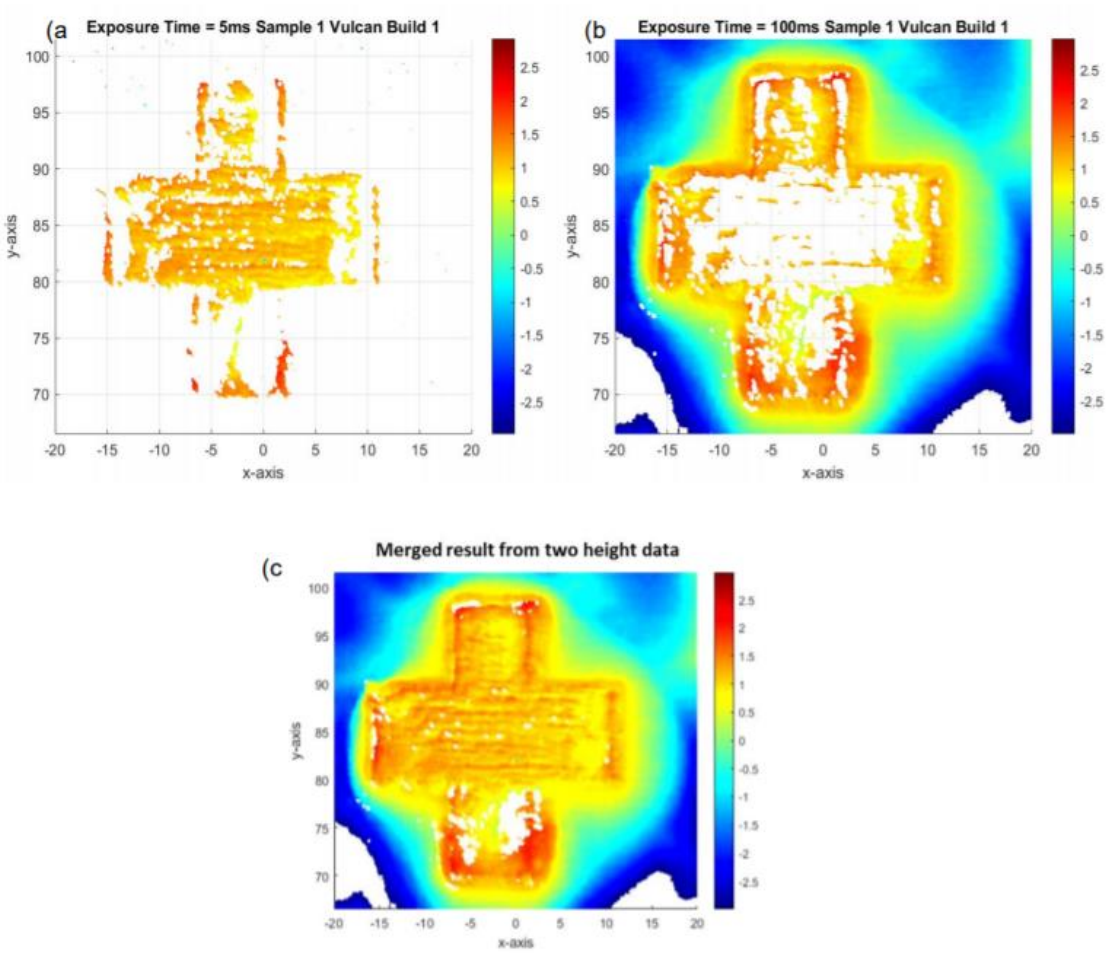

Figure 4. 5 The two separate exposure measurement results merged

4.2 The measurement principle of HDR system

4.2.1 HDR method principle in AM

The principle of the fringe projection system, which consists of a CCD camera and a fringe projector is triangulation measurement. The measurement takes place after the geometrical relationship between the camera and the projector is established. The projector projects sinusoidal fringe patterns onto the sample surface, and the camera captures these deformed fringes. The absolute height value can be calculated from the phase map based on the geometrical relationship model. Therefore, high-precision phase algorithms need to be investigated. The methods to obtain absolute phase information are generally divided into two categories, phase wrapping algorithms, and phase unwrapping algorithms. These methods have been introduced in chapter 2 and chapter 3.

Phase-shifting methods were introduced in section 2.3. If a multi-step phase-shifting algorithm with a phase shift of δn is adopted, the intensity distributions for the ideal sinusoidal fringes can be described as,

$$I_n(x,y) = A(x,y) + B(x,y)\cos(\varphi + \delta_n), n = 1,2,3,...,N \quad 4.1$$

where A(x, y) is the average intensity, B(x, y) is the intensity modulation, and Φ(x, y) the phase need to be solved for. The captured intensity with different reflective rate can be expressed as,

$$I_c(x,y) = Ep \times Rf(x,y) \times I_n(x,y) \quad 4.2$$

where Ep is exposure time, $Rf(x,y)$ is the reflective rate. Therefore, a powder bed with a low reflective rate and a long exposure time can be represent as,

$$I_{c-powder}(x,y) = Ep_{long} \times Rf_{low}(x,y) \times I_n(x,y) \quad 4.3$$

where $I_{c-powder}(x,y)$ is under 255 grey levels. When the surface becomes “shiny” with an increased reflective rate, the exposure time is reduced. The solidified metal surface with a high reflective rate and a short exposure time can be expressed as,

$$I_{c-metal}(x,y) = Ep_{short} \times Rf_{high}(x,y) \times I_n(x,y) \quad 4.4$$

where $I_{c-metal}(x,y)$ is under 255 grey levels with a suitable exposure time Ep_{short}. After obtaining the unsaturated fringe pattern, it is necessary to identify effective pixels that will be selected from the two sets of fringe patterns respectively.

After projecting 12 fringe patterns, a background intensity is projected.

$$M_c = A(x,y) + B(x,y) \quad 4.5$$

where M_c is the captured background intensity. Therefore, the effective area can be selected as,

$$Mask = \begin{cases} 1 & M_c \geq 250 \\ 0 & M_c < 250 \end{cases} \quad 4.6$$

After the effective pixel area is determined, a series of composite fringe patterns can be merged by two sets of the fringe patterns $I_{c-powder}$ and $I_{c-metal}$. The composite fringe pattern can be expressed as following,

$$I_{composite} = I_{c-metal} \times Mask + I_{c-powder} \times (\mathrm{U} - Mask) \quad 4.7$$

where U is a matrix with one element. Therefore, a wrapped phase can be represented by using phase shifting as shown,

$$W(\varphi) = -\arctan\left(\frac{\sum_{i=1}^{N} I_{composite}(x,y)\sin(\delta_i)}{\sum_{i=1}^{N} I_{composite}(x,y)\cos(\delta_i)}\right) \quad 4.8$$

where i indicates the ith image. The phase-shift algorithm can calculate wrapped phase accurately, when increasing the frames, the measurement results have smaller phase errors which are caused by nonlinear effects [**Error! Bookmark not defined.**]. After calculating the wrapped phase, the absolute phase data can be obtained by a temporal phase unwrapping method (optimum frequency selection algorithm). Sets of sequential sinusoidal fringe patterns are projected onto test surface, the number of fringes is defined by the following equation [**Error! Bookmark not defined.**]:

$$N_{max} = (N)^2$$

$$N_{max-1} = (N)^2 - 1$$

$$N_{max-2} = (N)^2 - N \quad 4.9$$

where N_{max} is the maximum number of fringes, If N=9, the maximum number of fringes is 81, therefore N_{max-1} =80 and N_{max-2} =80.

After the above calculation, the fused phase map can be obtained. The relationship between the absolute phase and depth of the polynomial is introduced in chapter 3.3.2. In addition, the relationship between x and z, y and z is introduced in chapter 3.3.3. The depth information can be obtained by the phase value determined. Therefore, 3D data can be obtained after system calibration.

4.2.2 Classification principle of Support vector machines (SVM)

SVM is a two-class classification model [181]. The basic model is a linear classifier with the largest interval defined in the feature space. The algorithm creates a line or a hyperplane which separates the data into classes [182]. When the different kernel functions are used for classification, SVM can become a nonlinear classifier. The learning strategy of SVM is to maximize the interval, which can be formalized as a problem of solving convex quadratic optimisation, so there is a unique optimal solution.

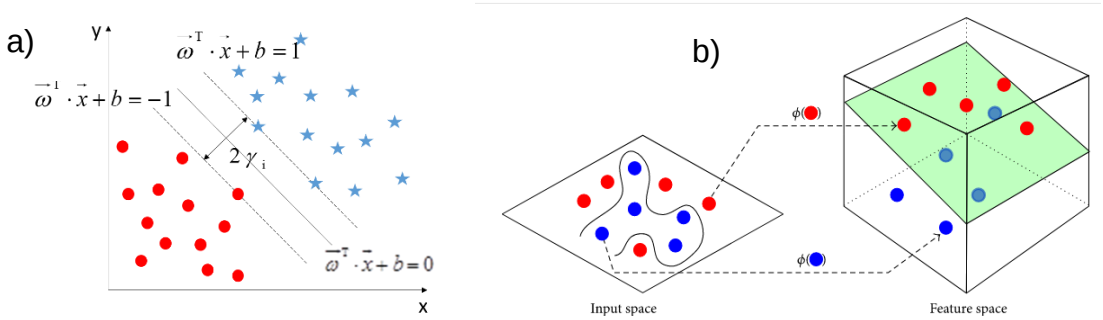

Figure 4. 6 The classification principle of SVM (a) Support vectors delimiting the margin between classes. (b) Samples mapping from input space into feature space [183]

As Figure 4.6 shows, the separation hyperplane is $\vec{\omega}^{T} \cdot \vec{x} + b = 0$, sample point is $(\vec{x}_i, y_i)$.

Therefore, the distance from the hyperplane to the sample set is $\gamma_i = y_i(\frac{\vec{\omega}^{T}}{\|\vec{\omega}\|} \cdot \vec{x}_i + \frac{b}{\|\vec{\omega}\|})$.

By maximizing the margin ($2\gamma_i$), the SVM model is used to solve the segmentation hyperplane problem. In order to simplify the calculation, the constraint problem is transformed into a Lagrangian optimization problem, and the simplified equation is as follows,

$$L(\alpha) = -\frac{1}{2}\sum_{i=1}^{N}\sum_{j=1}^{N}\alpha_i\alpha_j y_i y_j \vec{x}_i^{T}\vec{x}_j + \sum_{i=1}^{N}\alpha_i \quad , \quad \alpha_i \geq 0 \quad and \quad \sum_{i=1}^{N}\alpha_i y_i = 0 \qquad 4.10$$

After obtaining the coefficients of the segmentation hyperplane, the optimal classification function can be expressed as Equation 4.11,

$$f(\vec{x}) = \mathrm{sgn}(\vec{\omega}^{*}\square\vec{x} + b^{*}) = \mathrm{sgn}(\sum_{i=1}^{n}\alpha_i^{*} y_i(\vec{x}_i\vec{x}) + b^{*}) \qquad 4.11$$

where $\vec{\omega}^{*}$, b^{*}, α_i^{*} are the coefficients of the optimal hyperplane. Therefore, the sample data can be marked, one class is marked by 1 and the other is -1. For the linearly indivisible sample data, after the kernel function is determined, the optimization equation becomes:

$$L(\alpha) = -\frac{1}{2}\sum_{i=1}^{N}\sum_{j=1}^{N}\alpha_i\alpha_j y_i y_j K(x_i, x_j) + \sum_{i=1}^{N}\alpha_i \qquad 4.12$$

where $K(x_i, x_j)$ is the kernel function. Radial basis function is applied as kernel function. Generally, multi-categories need to be classified. The method of one-versus-rest (OVR) is adopted to address multi-classification. During the training, based on the

categories, the samples are classified into one category successively which is labelled by 1, and the rest of samples into another class which is labelled by -1. In other words, if there are K categories in the sample set, K classifiers will be obtained after classification training. The unknown sample is classified into the category with the maximum classification function value as the shown in Figure 4.7.

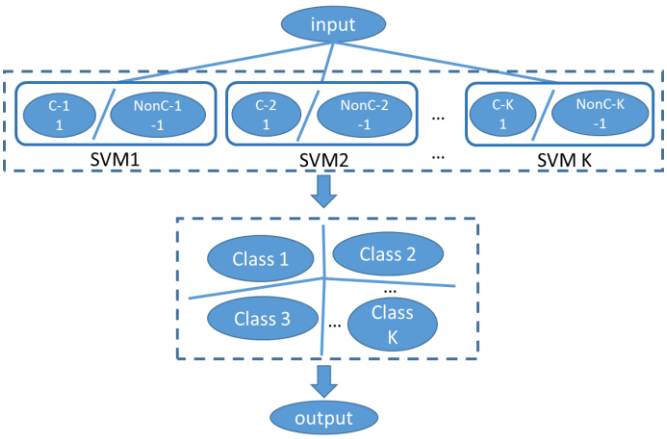

Figure 4. 7 Schematic diagram of SVM multi-classification method

4.3 SVM training and testing

4.3.1 Binary classification

Based on the principle of SVM classification, the dichotomous classification is firstly carried out. A standard part engineering surface manufactured by turning was selected to be classified as shown in Figure 4.8. Three surfaces with different roughness were selected for classification as shown in Figure 4.8. A fringe pattern was projected on the surfaces and the camera captured them with different exposure times. In the SVM model, the saturated pixels and exposure time are the input parameter for classification.

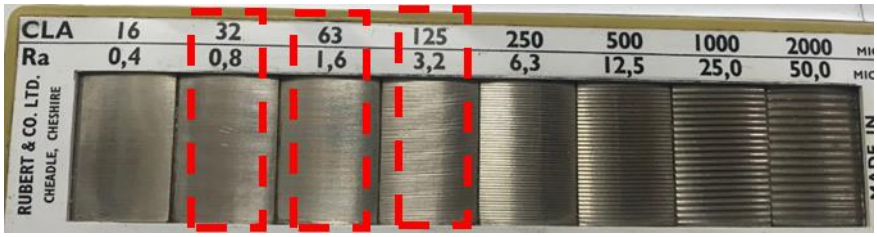

Figure 4. 8 Standard part manufacturing by turning for dichotomous classification

Some of the images are used for classification as shown in Figure 4.9. The surface roughness of Ra 0.8, Ra 1.2, and Ra 3.2 are classified respectively. It is obvious that the number of over-exposed pixels increases with the increase of exposure time.

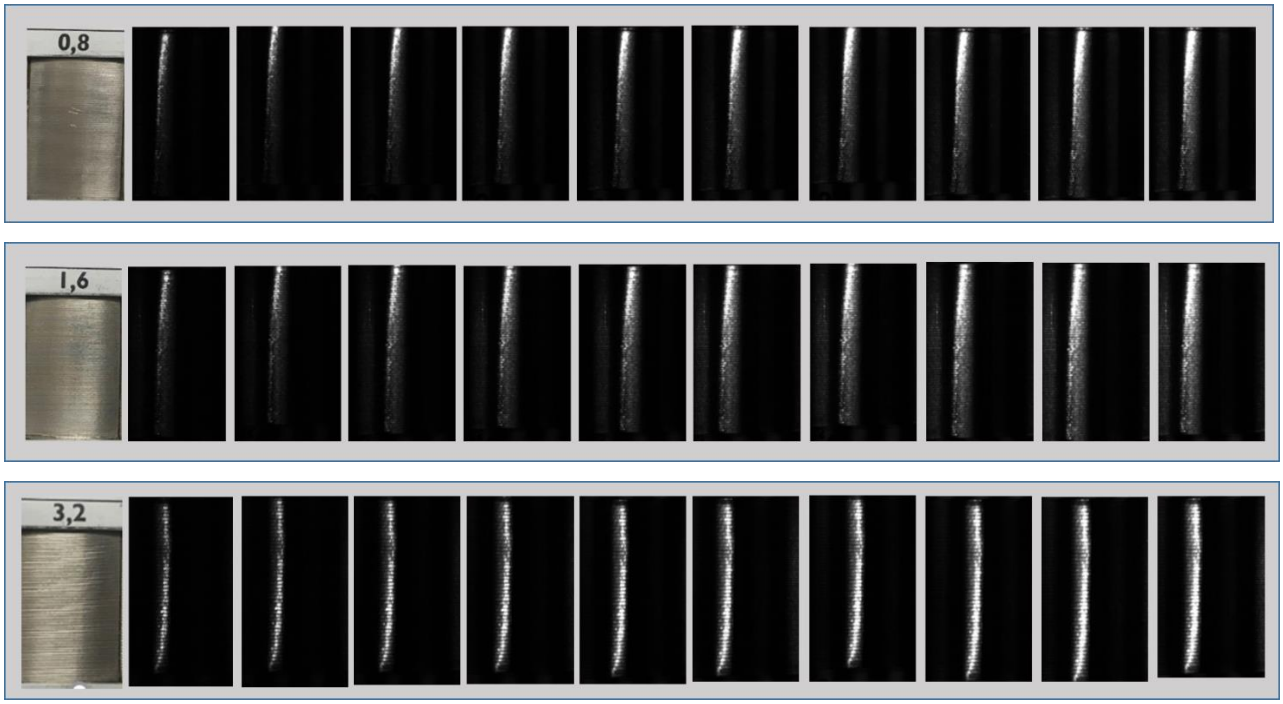

Figure 4. 9 Dichotomous classification imaged for training

The above three surfaces are pairwise classified and the classification results are shown in Figure 4.10. The X-axis is the exposure time and the Y-axis is the number of over-exposed pixels. After SVM classification, the roughness of Ra 0.8 and Ra 3.2, as well as Ra 1.6 and Ra 3.2 can be better distinguished, and the similarity between Ra 0.8 and Ra 1.6 is higher. Experimental results show that this method can be used to classify different surface roughness.

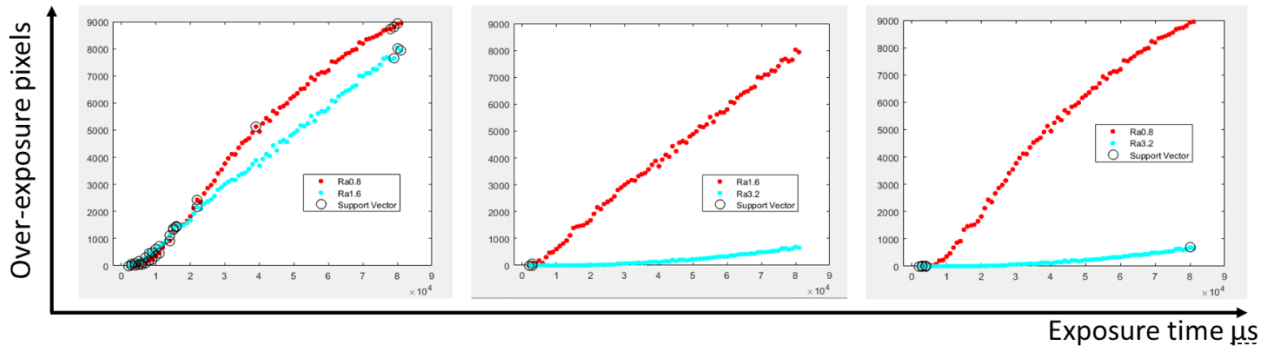

Figure 4. 10 SVM Dichotomous classification results

4.3.2 SVM training

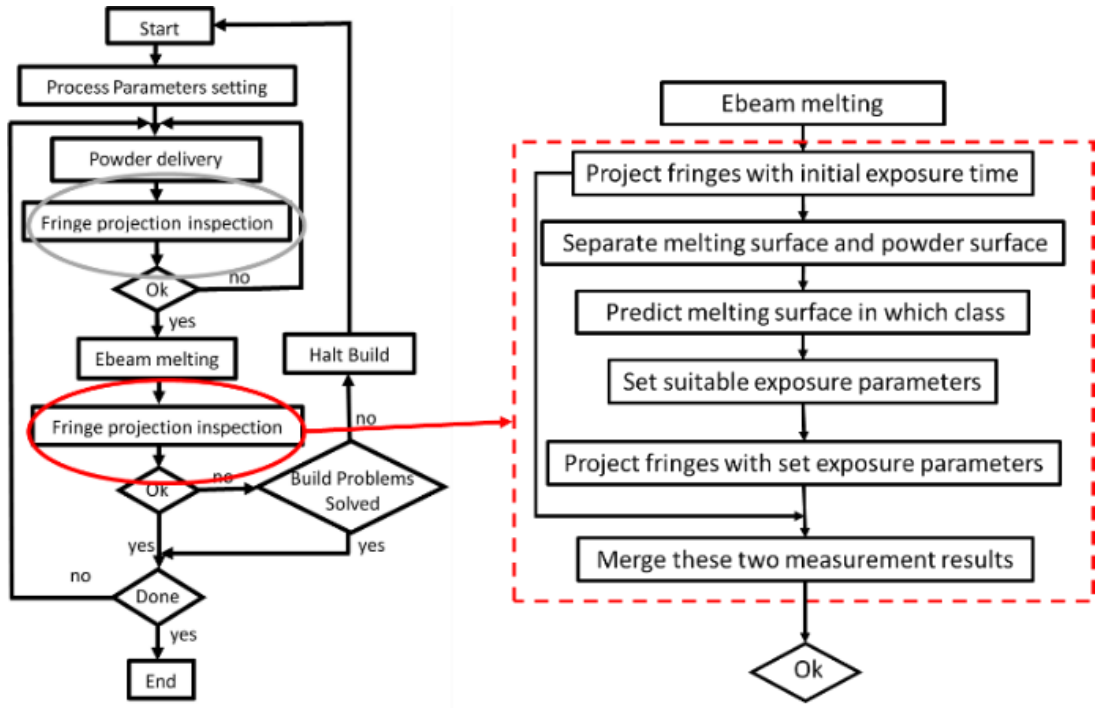

Figure 4. 11 The process of "shiny" surface inspection

The process flow of printed surface inspection is shown in Figure 4.11, after Ebeam melting, the projector projects fringe patterns on to surface with an initial exposure time. The projected patterns include a set of sinusoidal patterns and a blank background intensity pattern(Equation 4.5). The sample surface is captured by the initial exposure time and projection intensity. A Canny operator was used to separate the printed reflective surface and powder, the unit overexposure pixel number in the reflective area was calculated as the input parameter 1, and the initial exposure time was the input parameter 2. To ensure that the number of input exposure pixels is not affected by the size of the object during training and measurement, the method uses a fixed window to select the same number of pixels to calculate the number of exposure pixels. For the measurement of larger specimens, the ratio between saturated and total pixels could be considered during the training phase. The SVM classifier can then predict the printed surface classification and its suitable exposure parameters based on these two input parameters. The system then projects a set of fringe patterns and the camera captures them with predicted exposure time for the second measurement. Finally, the results of the two measurements (background

powder and “shiny” printed layer) are merged to determine whether the measured surface is qualified.

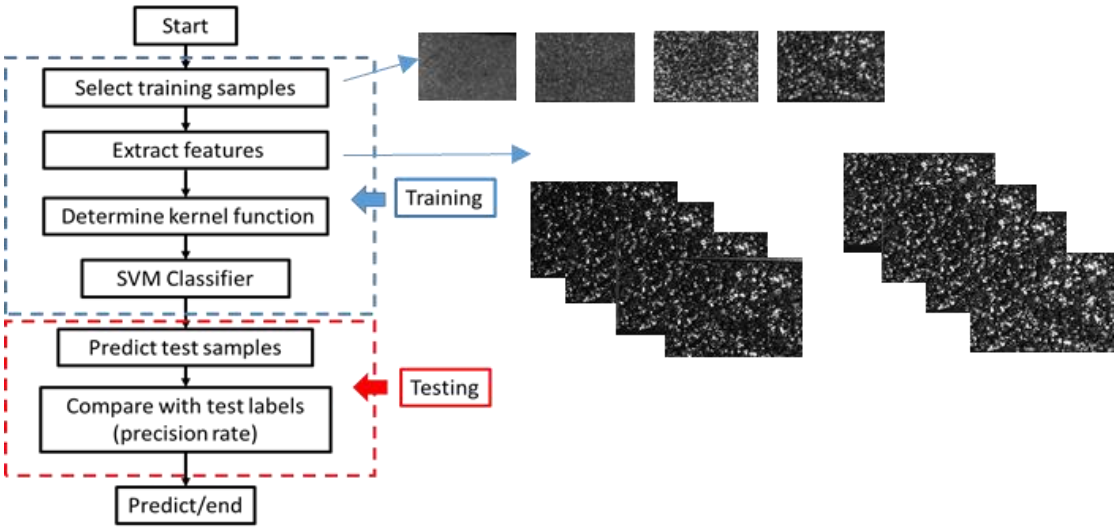

Figure 4. 12 Training and verification flow chart of SVM classifier

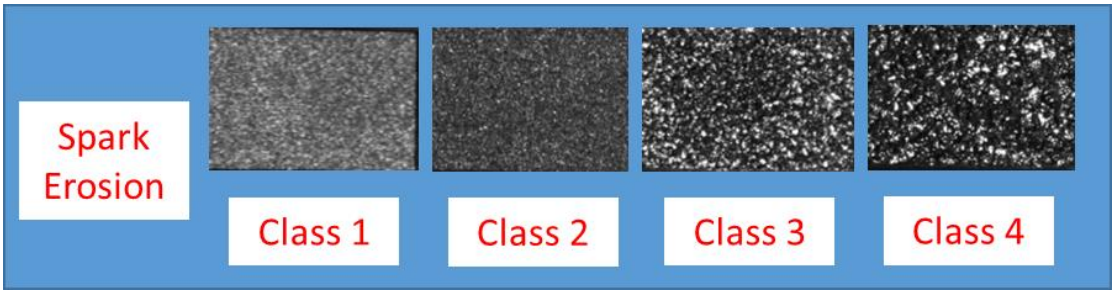

Figure 4. 13 The training surfaces which manufactured by spark erosion

In the process of SVM training, as shown in Figure 4.12, several manufactured surfaces as samples were selected as shown in Figure 4.12. The projector projected a background pattern to the spark eroded samples and the camera captured these texture images with a set of different exposure times. The average saturated pixel number of each surface was calculated as a classification feature and the corresponding exposure time as another classification feature. The Radial basis function as a kernel function was applied to determine the hyperplane. To verify the proposed method, four levels or roughness of test surfaces were classified and trained as shown in Figure 4.13. According to the proposed classification method, four SVM classifiers can be obtained. The selected surfaces used for classification were standard spark erosion parts (Rubert specimens), covering the dynamic reflective range of roughness from Ra 6.3 µm to Ra 50 µm. According to the exposure time and

saturated pixel number of each training surface sample, the scatter diagram is shown in Figure 4.14.

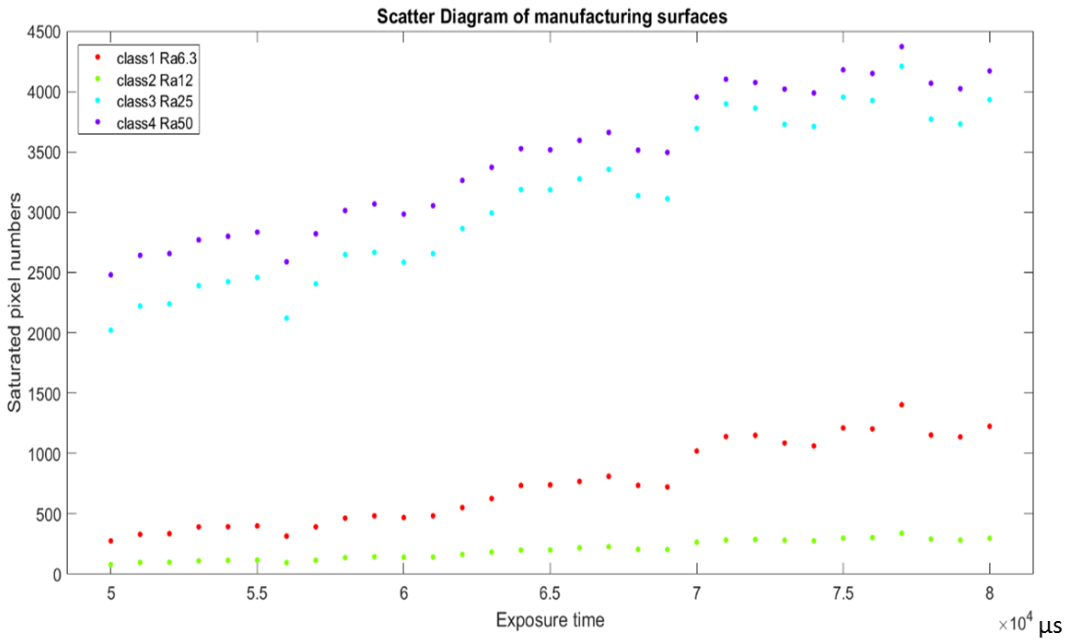

Figure 4. 14 The scatter diagram of manufacturing surfaces

4.3.3 SVM testing

To verify the accuracy of the SVM multi-classifier, the samples with different input parameters were classified as shown in Figure 4.15 and Table 4.1. Each known sample is put into the obtained classifiers, and the classification results with the highest value are the right category. By comparing the predicted results with the actual classification labels, the correct recognition rate is over 86%. After training, samples can be predicted by SVM as shown in Figure 4.15. As can be clearly seen from Figure 4.15, there are some prediction errors from similar points, but the prediction rate is better than 86%.

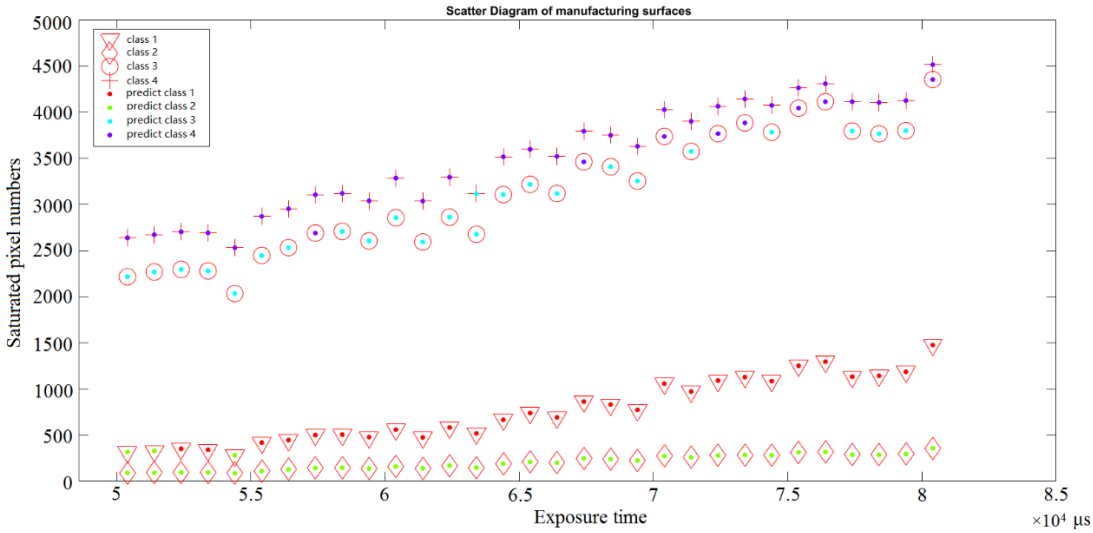

Figure 4. 15 The test samples compared with predict samples

Table 4. 1 The prediction results

Class	Class1(red)	Class2(green)	Class3(blue)	Class4(purple)
Cross validation error	0.0887	0.05645	0.2016	0.1855
Precision rate	0.8629			
False alarm rate	0.0645			

Table 4.1 shows the testing results of SVM classifier, cross validation error of each training surface is 0.0887, 0.0565, 0.2016, and 0.1855 respectively. The correct prediction rate is 0.8629 (86%), and the false alarm rate is 0.0645.

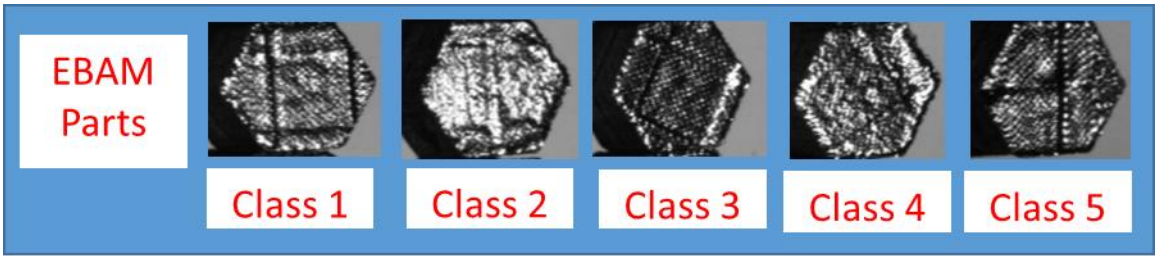

Figure 4. 16 The training surfaces which manufactured by EBAM

To verify the feasibility of the proposed method to various surfaces, specially manufactured surface by electron beam, five EBAM printed components (training samples) were classified as shown in Figure 4.16. The measured surfaces are manufactured at similar Ebeam power and cover most of the surface characteristics

("shininess") produced by the EBAM system. In the future, the surface may be manufactured by different power levels to adjust for features such as part overhang, this will be further classified, and the classification characteristics and categories will be expanded to cover the whole manufacturing surfaces for the range of different Ebeam powers.

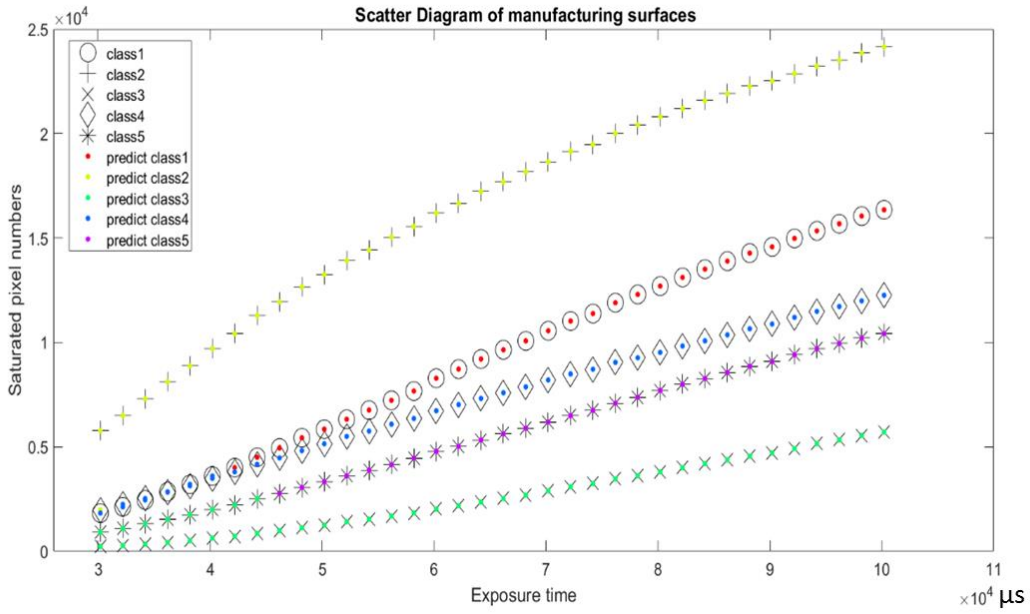

Figure 4. 17 The test samples compared with predict samples

The recognition accuracy was verified by changing the exposure time on these five samples as shown in Figure 4.17 and the correct prediction rate was 91.67%. Although SVM has not been used in similar measurement situations, prediction rates in other applications such as facial emotion recognition [184], which have recognition rates around 80%. In this experiment, over 86% and 91% recognition rate are higher than traditional SVM applications. The training results showed that the proposed method could identify the measured surface well and greatly improve the measurement efficiency of high dynamic range surfaces.

4.4 Experiments

The structure of the utilised AM machine is shown in Figure 4.18. The fringe projection system is fixed on top of AM machine. The position of the camera and projector outside of the vacuum build chamber with the viewing ports underneath the camera and projector are clear in the figure.

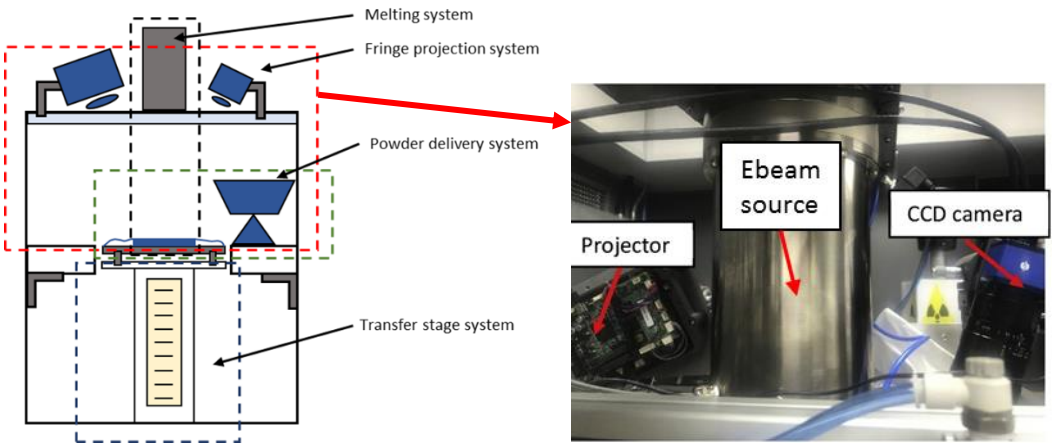

Figure 4. 18 Prototype system with fringe projection system in a new EBM machine

The projector projected 12 sinusoidal fringe patterns with fringe number 81 80 72 and the background pattern with 240 grey level intensity is projected onto the surface under test. The projected fringes were deformed due to the shape of the sample surface. The intensity of the background pattern was captured by the camera, which was changed by the different reflective rates of the surface. The camera captured these deformed fringes and the blank texture background image with the initial long exposure time. The deformed fringe patterns were divided into the effective region and saturated region by the corresponding mask as shown in Figure 4.19 (b). After SVM classification, the sample under test belongs to printed parts training category 2. Then, the corresponding exposure time of category 2 was reset, the system then carried out the second set of measurements. The captured fringe patterns with the low exposure time were cropped to select the effective region by the mask. Therefore, 12 unsaturated intensity patterns were merged by two measurements in Figure 4.19 (c). Figure 4.19(a) is the photograph of the sample under test, figure 4.19(b) is the effect region mask. After the process of four step phase-shifting and three-frequency selection phase unwrapping, the merged absolute phase map can be calculated as shown in Figure 4.20.

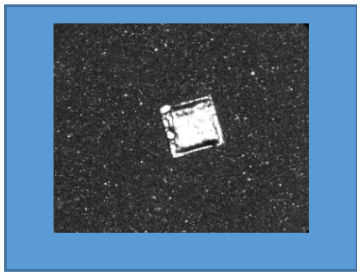

(a) Photograph of test sample

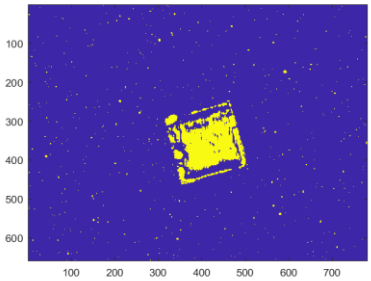

(b) Effective region mask

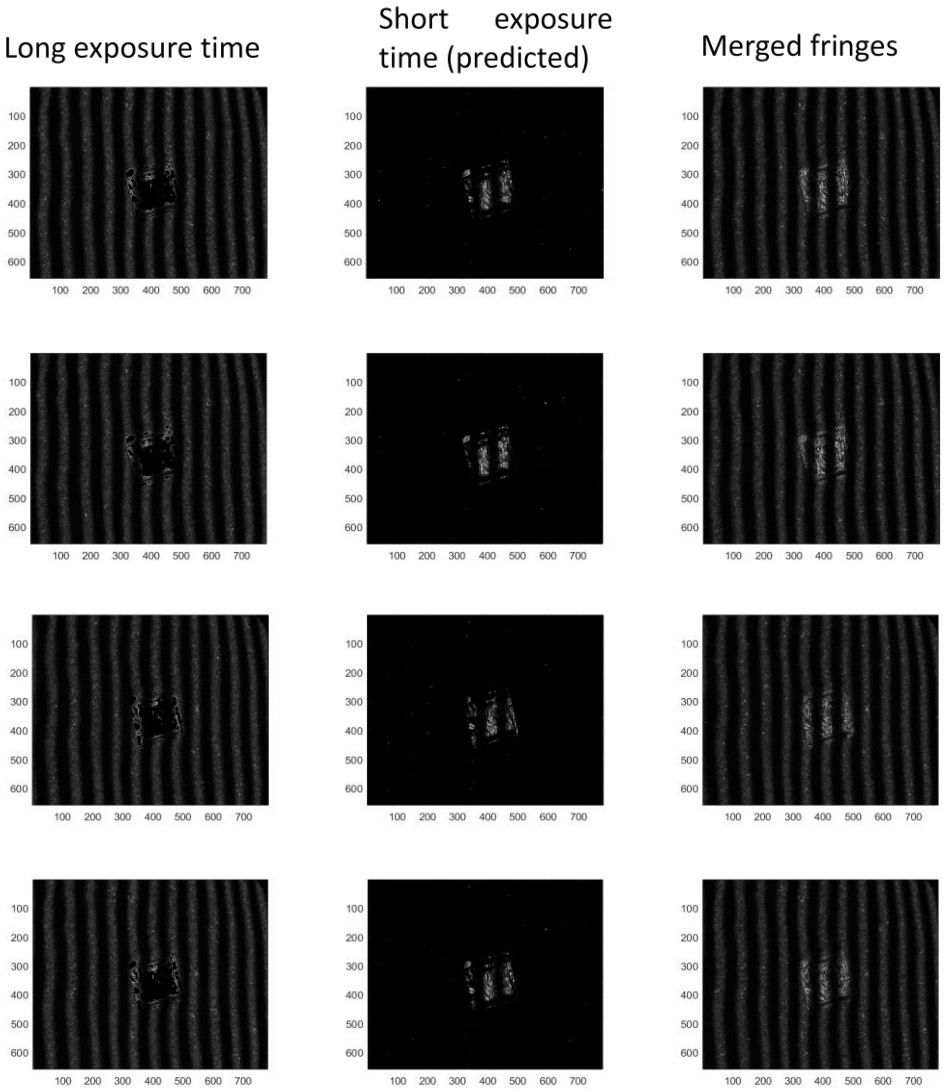

(c) Fringes with long exposure time and short exposure time and merged fringes

Figure 4. 19 The captured fringes with two measurements and the merged fringes

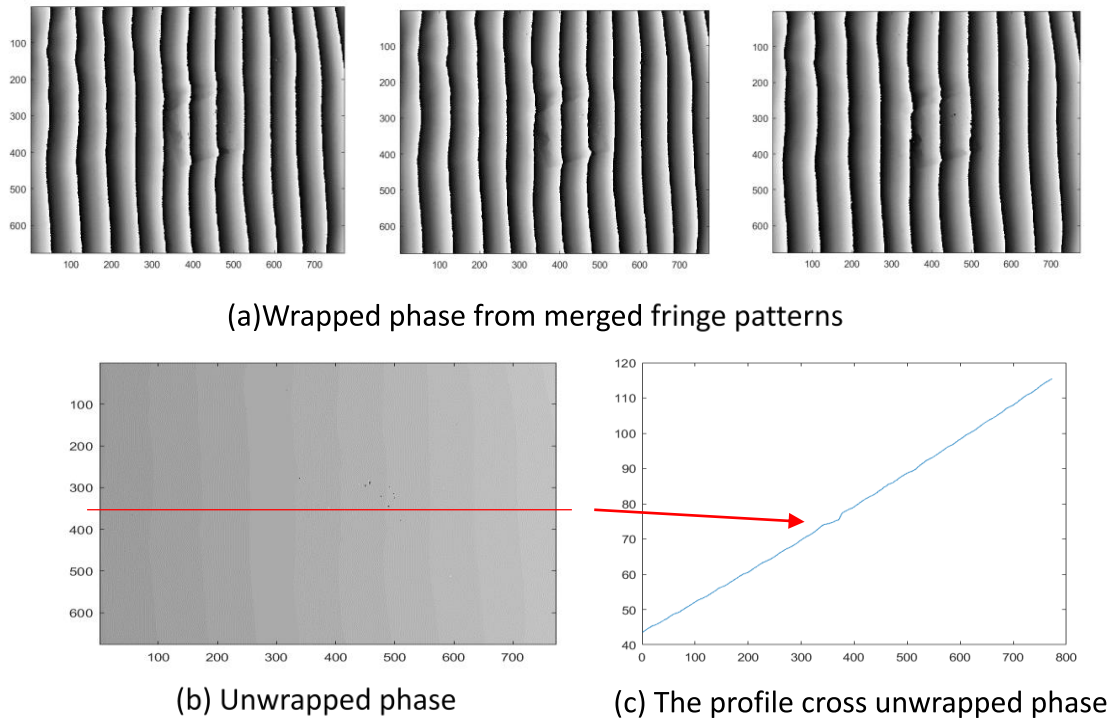

Figure 4. 20 The wrapped phase and the unwrapped phase with the fringe frequency 81 80 72

Figure 4.21 shows the one layer of EBAM manufactured square part with high reflective features and the powder with a low reflective rate. The surface was measured successfully simultaneously with the whole process taking approximately 4 seconds for the two measurements. Compared with the traditional HDR multi-exposure time method, which is indicated in Figure 4.4, the proposed method reduced the measurement time from 16 seconds down to 4 seconds. Due to the prediction of the measured surface category and corresponding exposure time, the measurement efficiency has been improved. The square built parts within the powder bed showed evidence of the defect termed part swelling. Edge thermal swelling is a common defect in the manufacturing process. If the solid edge is much higher than the powder level, it can cause damage to the powder delivery rake and corrective action needs to be taken or the process abandoned. Figure 4.21 (b) shows the orthogonal 2D extracted profiles across the reflective region which shows the edge swelling thermal height value which is higher than the powder bed and printed centre area. Knowing this, a threshold height value would be set to determine whether to process halt or not according to the defect size.

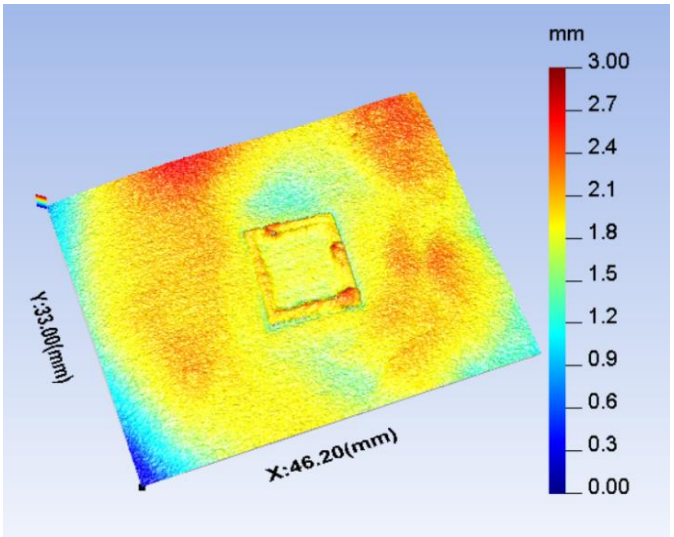

(a) Measurement results of the manufacturing square and the powder surface which have dynamic range reflective characteristic (X and Y represent the size of the measured surface)

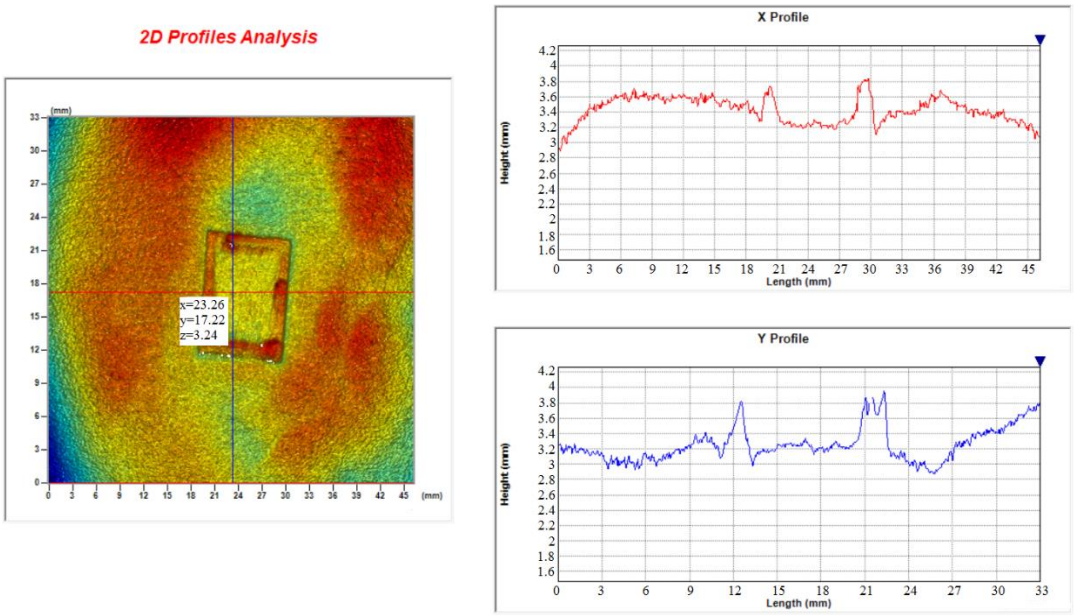

(b) 2D extracted profiles across the shiny region

Figure 4. 21 The measurement result of a manufacturing square

Figure 4.22 shows the 3D measurement results of printed parts manufactured by EBAM. Based on the printed parts classifier (shown in Figure 4.16 and Figure 4.17), these samples were classified by SVM classifiers. Figure 4.22 (a) and (b) show sample1 and 2 which were belonging to category 3 with a suitable exposure time of 30ms. Figure 4.22 (c) shows sample 3 which was belonging to category 5 with a suitable exposure time of 25ms. In Figure 4.22 (c), four depression-type defects can

be viewed in the middle of the surface. These depressions could cause incomplete melting in subsequent layers due to uneven powder thickness on the surface. In such a case, the system can be set to determine whether to rectify the problem in the subsequent layer melting by adjusting the energy input at the defect position. Note, X and Y represent the dimensions of the measured samples along with the X and Y directions.

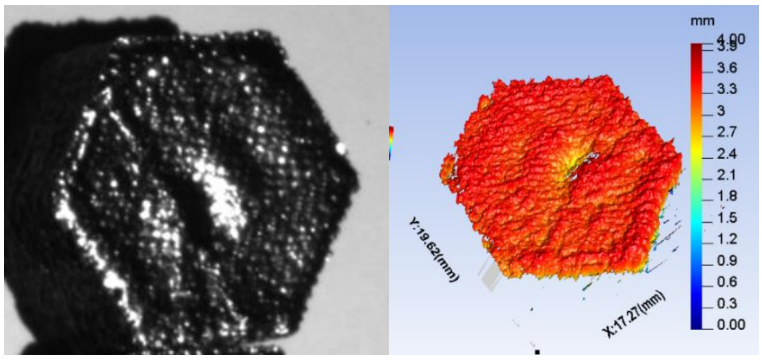

(a) Sample 1 belongs to category 3 measured by exposure time 30ms

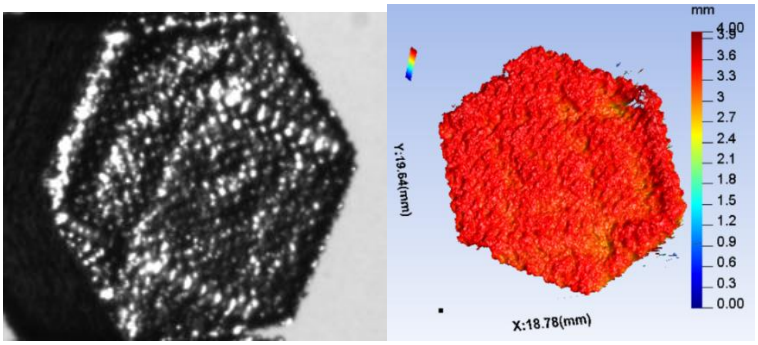

(b) Sample 2 belongs to category 3 measured by exposure time 30ms

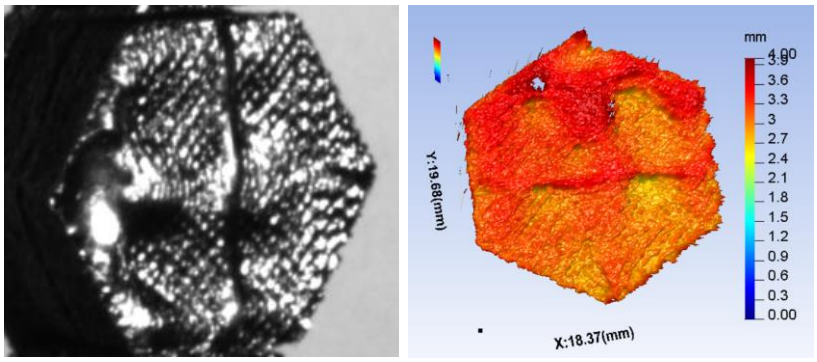

(c) Sample 3 belongs to category 5 measured by exposure time 25ms

Figure 4. 22 Measurement result of printed parts with prediction exposure time (X and Y represent the size of the square projected measured surface)

4.5 Summary

In this chapter, an in-situ monitoring technique, using a fringe projection profilometry was further developed to facilitate inspection of the powder bed and resolidified part surface produced by an EBAM. After the electron beam melting the powder is solidified and the reflective characteristic of the surface changes from diffuse to highly reflective. This phenomenon increases the difficulty for in-process measurement systems to measure both diffuse powder and reflective metal surfaces. A novel intelligent fringe projection technique using the SVM algorithm is proposed to measure such high dynamic range surfaces. By training the exposure time and saturation pixel number of different surfaces, the inspected surfaces are classified and predicted by an SVM classifier. The training error is evaluated, and the correct recognition rate is better than 91% on the printed samples, which indicates the proposed training method can effectively predict the measurement surface. Post melting the system has the capability for inspecting both powder bed and metal surface sequentially. The examples of melting edge swelling on a part within a powder bed during and point defects on builds show the measurement system offers a key tool to enable improved manufacturing accuracy and control during the EBAM process. The system has been developed on a commercial EBAM machine and control software integrated into the AM machine control. Using machine-based triggering the measurement speed is around 2 secs for the powder bed inspection and less than 5 secs for the melting surface and surrounding powder inspection during each measurement cycle, in implementation, this should not incur extra-time loss during the manufacturing process. The presented system is fully integrated into the build cycles of the EBAM machine providing a “closed-door”, high-speed measurement process.

Compared with current methods for addressing high dynamic range issues, the author considers that the intelligence of the fringe projection system has been improved and the inspection efficiency combined into a working commercial environment. By predicting the printed surface reflectance, the surface was classified by the classifier, therefore the appropriate exposure time was set. The system achieved high precision measurement without adding extra-time loss in the complete AM process. At the same time, this method can also be used in other fields where high dynamic measurement issues need to be solved. However, there are still some issues that need to be

addressed in the future. At present, the method investigated in this chapter still requires two measurements. Due to the different reflectivity of the printed surface and the powder, the measurement time could be reduced in the future. A high accuracy measurement method which is based on measuring different surface roughness's and an adaptive intelligent fringe projection needs to investigate to realize multiple examples of surface reflectivity through a single measurement.

Chapter 5 Theoretical and experimental investigation of structure light system for high precision and reflective surface after post-machining

This chapter provides a theoretical and experimental investigation of specular surface measurement based on deflectometry technique. The chapter is divided into six sections: section 5.1 is an introduction to deflectometry technique and applications, section 5.2 covers the 3D measurement principles of deflectometry, and section 5.3 is the development of the proposed deflectometry technique, and section 5.4 is system calibration simulation, and section 5.5 gives experiment results and section 5.6 is a summary.

5.1 Introduction

In chapter 3 and chapter 4, in-process inspections have been introduced. However, in the application of AM, after manufacturing, post-process inspection needs to be performed. Often X-ray Computer Tomography for internal and external structural inspection or CMM for dimension inspection is applied. AM parts however are further processed either chemically or mechanically to enhance their precision and surface finish. Following such post process finishing e.g. polishing, the surface becomes highly reflective and specular. The deflectometry technique is one of the detection approaches for inspecting such specular surfaces [100]. This technology can be applied not only to the post process AM field but also to other ultra-precision machined surfaces. With the development of ultra-precision machining, especially the complex geometrical surface with superior functional performance, a high precision metrology method becomes the key to achieve a higher manufacturing performance. Optical metrology methods have been investigated for high-precision surface measurement, such as interference inspection, PMD, DPMD, confocal microscopy [185]. However, there are clear measurement issues, such as low measurement precision, multi-colour crosstalk, low system calibration precision, low measurement speed which arise with the application of a particular technique. Therefore, a method for inspection high-precision specular surface with the characteristic of high precision, high speed, high effective need to be investigated especially as a complimentary inspection technology for post process AM parts. Phase measuring deflectometry (PMD) has been studied

for the measurement of the three-dimensional (3D) shape of specular ultra-precision objects. The principle of PMD is that a computer generates sinusoidal fringe patterns and the fringes are collected at a camera. From a different viewpoint, fringe patterns are reflected by a measured surface and deformed with regarding the slope and height of the specular surface. The deformed fringe patterns can be captured by a camera. Phase information in the deformed fringe patterns is demodulated to obtain the slope of the measured specular surface or the height. The 3D shape of the test surface can then be reconstructed by integrating the gradients or the obtained height information by using different methods.

In this chapter, methods for measuring discontinuous specular surfaces based on the PMD technique are investigated in this instance as a post process metrology technology for AM parts. Three-generation systems are developed to measure the full-field 3D shape of the complex specular surface with colour fringe measurement. Prototype 1 system consists of one camera, one LCD screen, and a translation stage. The depth information of the measured object can be obtained after a single movement. Prototype 2 system consists of one camera, two LCD screens, and a beam splitter (BS). A mathematical model with geometric relations of parallel planes was derived to directly relate an absolute phase map to depth data, instead of the gradient. All equipment is fixed but has certain position relation limitations. The phase map is used to calculate the depth information after system calibration. Prototype 3 system uses flexible mounted but fixed components to null the restriction of position relationship. System calibration methods are reported. Experimental results show that the proposed developed DPMD method can obtain the full-field 3D shape of specular objects having discontinuous or complex geometrical surfaces accurately and effectively.

5.2 Measurement principle of direct phase measurement deflectometry

5.2.1 DPMD based on LCD parallel position relationship

The deflectometry system usually consists of an LCD screen and a camera. The measurement principle of deflectometry is mirror imaging. The standard sinusoidal fringes generated by the computer to the LCD. The fringes are reflected via the measured surface and captured by the camera from another view. The computer performs reconstruction calculations based these deformed images. Different from the

measurement principle of the fringe projection system, the deformed fringes in the deflectometry system contain not only depth information but also gradient information. That is, the factors affecting the deformation of these fringes are not only surface depth but also the gradient of the measured surface. Since the factors influencing fringe deformation include depth h and gradient θ, two sets of known parameters are required to optimise h and θ. In this case, two sets of parameters are obtained by moving the LCD screen, and a reference plane is also set, in which the reference plane is parallel to the display screen. The height difference between the measured surface and the reference plane is the desired depth information.

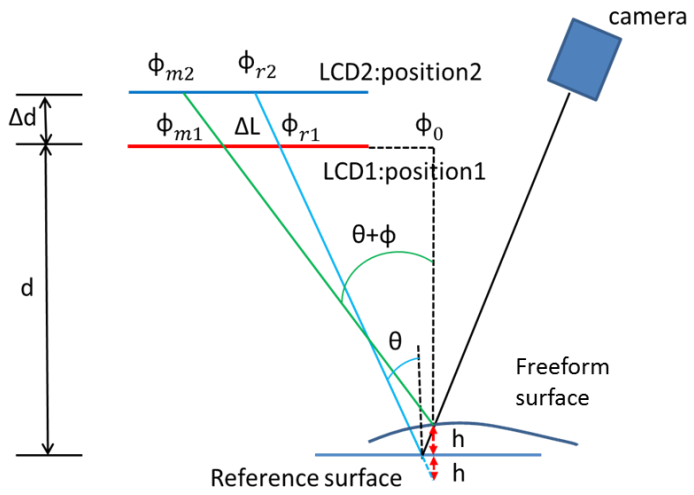

Figure 5. 1 Schematic setup of the 3D measurement system based on moving

Figure 5.1 shows the schematic setup of the 3D shape measurement system of specular surfaces using DPMD, which obtains depth data from the phase map directly. The system comprises an LCD screen, a CCD camera, and a translation stage. When the LCD at position 1, the fringe information deformed by the reflection of the measured surface and the fringe information reflected by the reference plane (calibrated by the high-precision mirror) is collected. Then the LCD is moved to position 2 by a translation stage, the moving distance is Δd . Same as position 1, the fringe information deformed by the reflection of the measured surface, and the fringe information reflected by the reference plane is captured again. According to the geometric relation shown in Figure 5.1, the following relation can be expressed:

$$(\varphi_{r1} - \varphi_{r2})q/2\pi = \Delta d\tan\theta \qquad 5.1$$

$$(\varphi_{m1} - \varphi_{m2})q/2\pi = \Delta d\tan(\theta + \varphi) \qquad 5.2$$

$$(d + h)\tan\theta + \Delta l = (d-h)\tan(\theta+\varphi) \quad 5.3$$

$$(\varphi_{r1} - \varphi_{m1})q/2\pi = \Delta l \quad 5.4$$

Where d is the distance between display position 1 and the reference plane, Δd is the moving distance. φ_{r1} is the absolute phase reflected through the reference plane at position 1. φ_{r2} is the absolute phase reflected through the reference plane at position 2. φ_{m1} is the absolute phase reflected through the measured surface at position 1. φ_{m2} is the absolute phase reflected through the measured surface at position 2. q is the fringe period. θ is the reflection angle of the screen reflected through the reference plane. φ is twice the gradient angle. Δl is the distance on LCD_1' between the two incident rays deflected by the measured surface and the reference mirror. Equation 5.1 to Equation 5.6 can be simplified into the following Equation:

$$h = \frac{\Delta d(\varphi_{r1} - \varphi_{m1}) - d[(\varphi_{r1} - \varphi_{r2}) - (\varphi_{m1} - \varphi_{m2})]}{(\varphi_{m1} - \varphi_{m2}) + (\varphi_{r1} - \varphi_{r2})}. \quad 5.5$$

The model is established in a reference coordinate system. In Equation 5.5, h is the absolute height from the reference surface. During the measurement, the absolute height information can be reconstructed by the phase value directly, which the system realises the measurement of discontinuous surface. The disadvantage of this method is that the LCD screen still needs to be moved once in the measurement process, and the measurement accuracy also depends on the positioning accuracy of the translation stage.

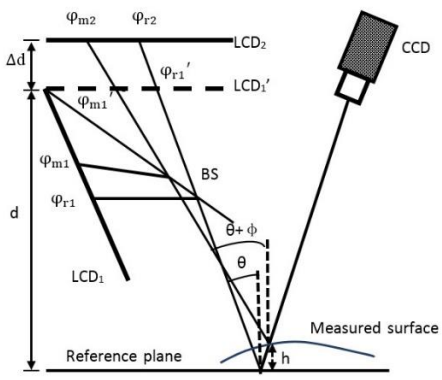

Figure 5. 2 A deflectometry system based on beam splitter

Based on the geometrical model of Equation 5.5, a new deflectometry system was designed, which consisted of one CCD camera, two LCD screens, and one beam splitter (BS) as shown in Figure 5.2. The BS was set in one proper position, such that the virtual image LCD1´ was strictly parallel to LCD2. This condition can influence

measurement accuracy. Moreover, a reference plane was set to get absolute depth data which is parallel to the two screens. The rays of light are displayed and reflected into the CCD camera via the measured surface and the reference mirror, as illustrated in Figure 5.2. The incident rays correspond to the same reflection light. The distance between LCD1´ and LCD2 and that between the reference plane and LCD1´ are denoted Δd and d, respectively. The absolute phases of the two incident rays are denoted φ_{r1}(or φ_{r1}´) and φ_{r2} on the reference mirror and φ_{m1} (or φ_{m1}´) and φ_{m2} on the measured specular surface. θ and θ+Φ are the angle between the incident ray and the normal vector of the reference mirror and the angle between the incident ray and the normal vector of the measured specular surface respectively, same as in Figure 5.1. Parameter h stands for the height of the measured specular surface with respect to the reference mirror. Because the optimum three-frequency selection method is calculated the absolute phase pixel by pixel, the height of the specular objects having isolated and/or discontinuous surfaces can be obtained from the phase value directly. After system calibration to calculate the values of Δd and d, the depth data can be calculated by Equation 5.5. The disadvantage of this method is that the position of LCDs is the strict condition, in which LCD1´ and LCD2 are parallel, as well as the reference plane is parallel with them.

5.2.2 Based on arbitrary LCD position DPMD

It is difficult to guarantee the parallel position relationship discussed in section 5.2.1, a method with arbitrary LCD positions to solve these strict conditions was investigated.

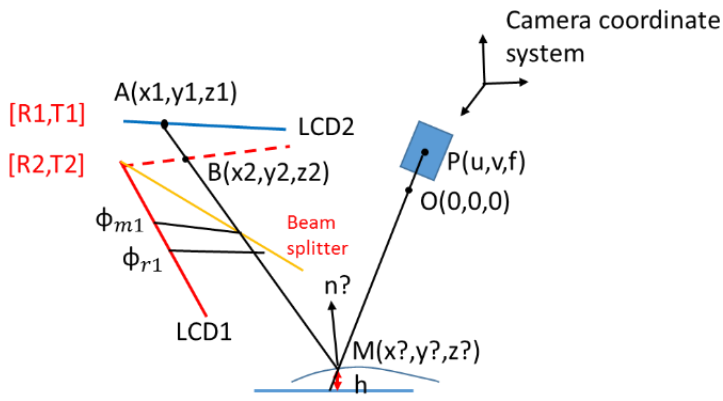

Figure 5. 3 Schematic setup of the developed 3D deflectometry system

Figure 5.3 shows the schematic setup of the developed 3D shape deflectometry system of specular surfaces using DPMD. The system comprises two LCD screens, a

CCD camera, and a plate beam splitter (BS). The positions of the two screens can be set arbitrary. The two screens display blue fringes and red fringes respectively. The red fringe shown on LCD1 is reflected by the BS to form a virtual image screen in the position of the red dotted line in Figure 5.3. The blue and red overlapping fringes are reflected into the CCD camera via the specular tested sample. Therefore, the two screens can be viewed at the same time by the camera. The measurement procedure is as follows：

Step1: Horizontal and vertical sinusoidal fringes are displayed on two screens, where LCD1 shows red patterns and LCD2 shows blue patterns respectively.

Step2: The absolute phase is calculated by using the four-step phase-shifting algorithm and the optimised three-frequency selection algorithm.

Step3: The coordinates value of the two LCDs are calculated by the absolute phase in the LCD coordinate systems.

Step4: LCD coordinate systems are converted into the camera coordinate system.

Step5: The coordinate of the measured object in the camera coordinate system is calculated by using the system geometry structure relationship and the camera internal parameters.

The camera-imaging model is a pinhole model. There is a one-to-one correspondence between the pixels on the CCD chip and the pixels on the screens. The coordinate values of the two LCDs in the LCD coordinate systems can be calculated by the absolute phase as follow:

$$xi = (Pn \times \frac{Ps}{2\pi}) \times \phi_v \qquad 5.6$$

$$yi = (Pn \times \frac{Ps}{2\pi}) \times \phi_h \qquad 5.7$$

where ϕ_v and ϕ_h are the vertical and horizontal phase value calculated by vertical and horizontal fringes, P_s is the size of LCD pixel pitch, P_n is the number of LCD pixels per fringe period. Therefore, the coordinate (x_1, y_1) of point A can be calculated. Then, the transformation relationship between the two coordinate systems can be expressed as follows:

$$\begin{bmatrix} x_{c1} \\ y_{c1} \\ z_{c1} \end{bmatrix} = [R\ T] * \begin{bmatrix} x_i \\ y_i \\ 0 \\ 1 \end{bmatrix} \qquad 5.8$$

where R and T are respectively the rotation and translation matrices of the LCDs in the camera coordinate system. Therefore, the coordinate (x_{c1}, y_{c1}, z_{c1}) of point A can be calculated by Equation 5.8. The coordinate (X, Y, Z) of the measured point M can be expressed by internal parameters of the camera as shown in Equation 5.9.

$$Z\times \begin{bmatrix} u \\ v \\ 1 \end{bmatrix} = Ain \times \begin{bmatrix} X \\ Y \\ Z \\ 1 \end{bmatrix} \qquad 5.9$$

$$Ain=\begin{bmatrix} \alpha & \gamma & u_0 & 0 \\ 0 & \beta & v_0 & 0 \\ 0 & 0 & 1 & 0 \end{bmatrix} \qquad 5.10$$

Ain is the internal parameters of the camera. (u,v) is the image coordinate of the image point P. The coordinate (X, Y, Z) of the measured point M can be also expressed by the coordinates of the two screens as shown in equation 5.11.

$$\frac{X-x_{c1}}{x_{c2}-x_{c1}} = \frac{Y-y_{c1}}{y_{c2}-y_{c1}} = \frac{Z-z_{c1}}{z_{c2}-z_{c1}} \qquad 5.11$$

Point A(x_{c1}, y_{c1}, z_{c1})and point B(x_{c2}, y_{c2}, z_{c2}) are on LCD1 and LCD2 respectively, where the mapping of the same pixel of the CCD occurs. After camera calibration, internal parameters and external parameters of the camera can be determined. The coordinate of the measured surface can be obtained by equation 5.9, equation 5.10, and equation 5.11.

5.3 Development of system

5.3.1 Prototype 1 with one camera and one projector

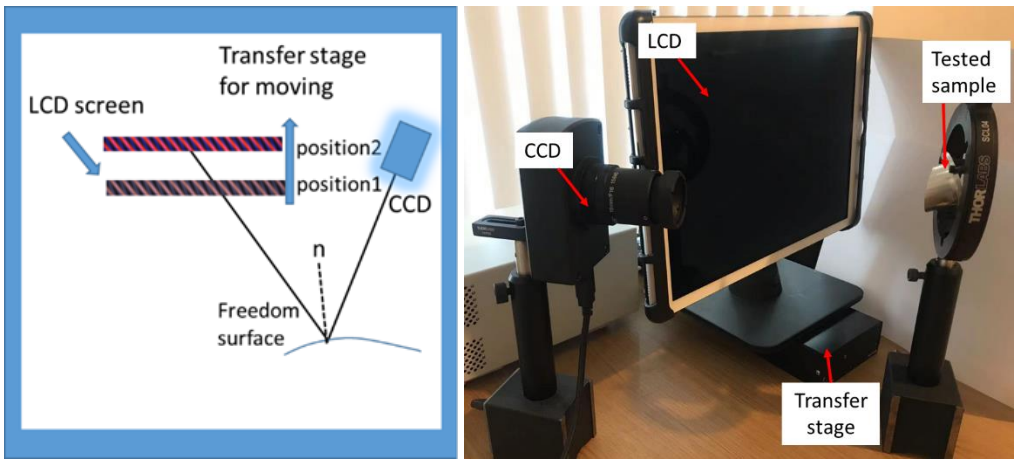

Figure 5. 4 Prototype 1 with one camera and one projector

Generation 1 system consisted of a camera and a screen which was fixed on a translation stage. During the measuring procedure, the screen needed to be moved to two positions. The limitations of generation 1 were that the precision of the moving guide limits the accuracy of the measuring system, and the operation is time-consuming.

5.3.2 Prototype 2 with one camera and two LCDs

Based on generation1, a generation 2 system was developed that consisted of one camera and two screens instead of a translation stage. A beam splitter (BS) is used to realise the parallel design of two LCD screens that display different colours on each screen separately and thus avoid mechanically moving a screen to two positions. A mathematical model is derived to directly relate an absolute phase map to depth data. Because it had strict constraints to two LCD screens and a reference mirror, this had associated system errors. The simultaneous acquisition of two colour channels also increases the measurement efficiency.

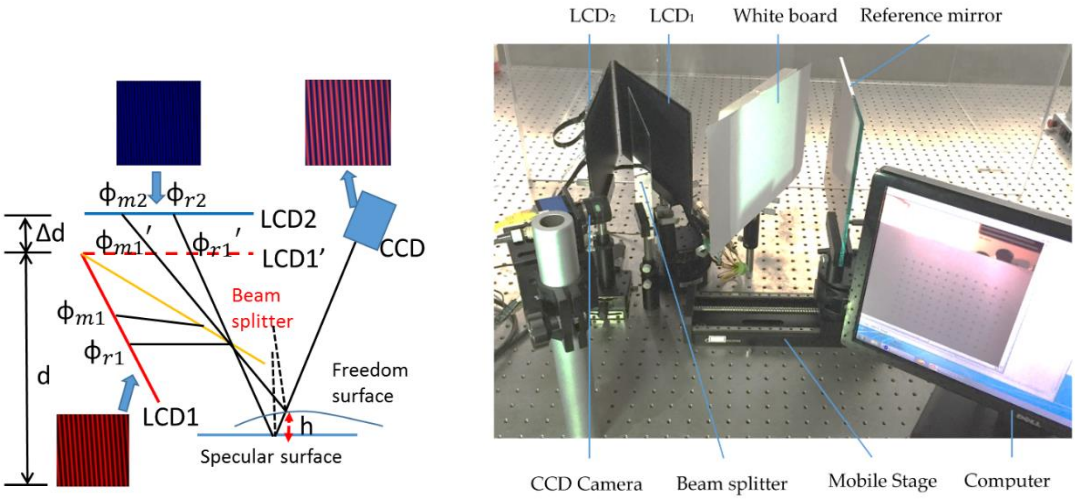

Figure 5. 5 Prototype 2 with one camera, two screens and a BS

5.3.3 Prototype 3 with freedom position of LCDs

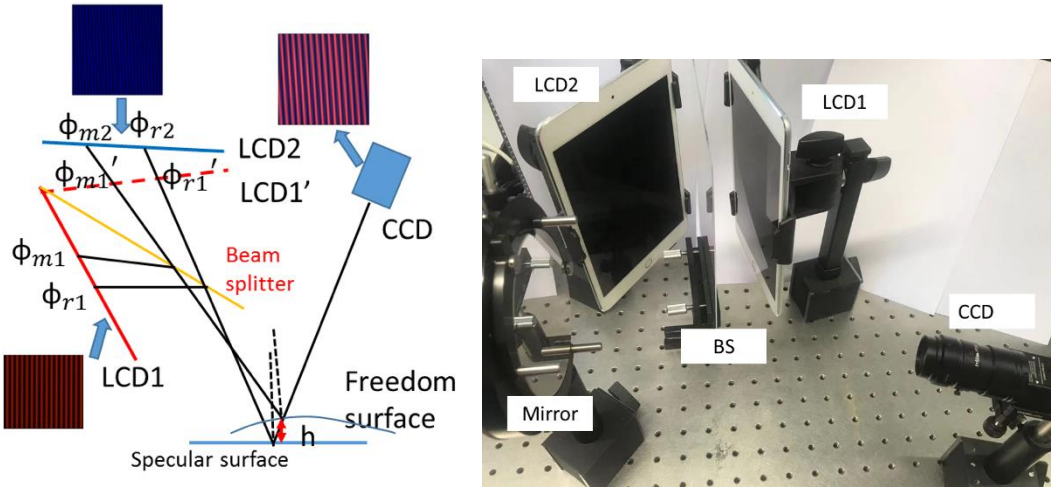

Figure 5. 6 Prototype 3 with arbitrary position of LCDs

Parallelism of the two LCD screens is not easy to achieve, a direct PMD method, which can be freely placed on the display screen was then studied. Different from the previous two methods, the fringes need to be displayed in both horizontal and vertical directions in this method.

5.4 System calibration

System calibration is a significant step of the optical systems, and the associated measurement precision is determined by the accuracy of the calibration results. This chapter mainly studies the corresponding calibration methods according to different measuring systems.

5.4.1 Prototype 1 and 2 system calibration

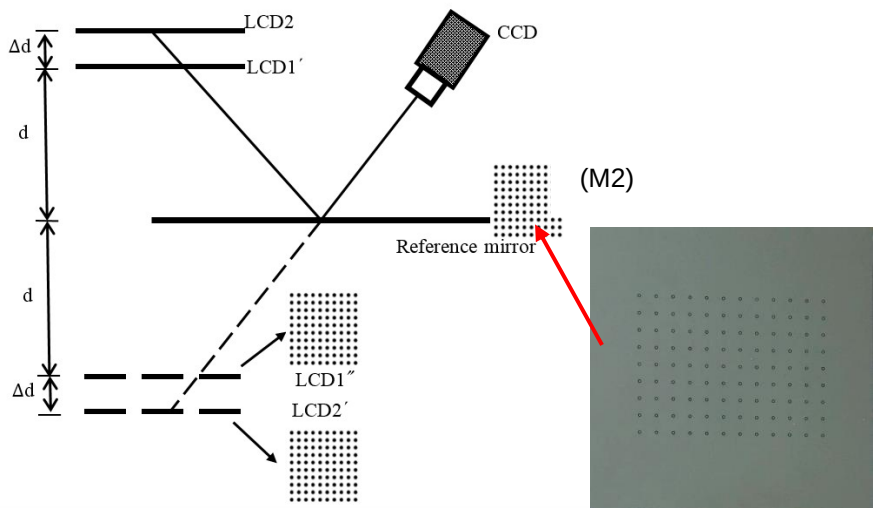

Figure 5. 7 Schematic of the calibration method

During the calibration procedure, two accurate plane mirrors are employed. M_1 is an ideal plane surface, M_2 is also a plane mirror with a ring marker matrix with known separation. Due to the limitation of the structure of prototype 2, the image position of the two screens in the camera coordinate system is parallel, so the parallel position relationship needs to be adjusted as a first step. The adjustment method is shown in Figure 5.7. The system consists of two LCD screens, a CCD camera, and a plate BS. M2 is employed to adjust the positions. A concentric circles image is generated by the software and displayed on both LCD screens. The camera captures the rings on two components surface and the M2 calibration mirror. The centre points of the rings can be extracted from three components. After camera calibration, the external parameters of the three components in the camera coordinate system can be obtained by using the known separation between neighbouring markers and the internal parameters of the camera. Based on the obtained external parameters, namely, the positions of three components in the camera coordinate system, the relative orientation of the three components is adjusted. This procedure is repeated several times until the relative position of the three components is parallel.

To calibrate Equation 5.5, the parameters denoted Δd and d need to be calculated and the absolute phase of the two screens on the reference plane needs to be obtained as well. Figure 5.8 shows the calibration method of the prototype 2 system.

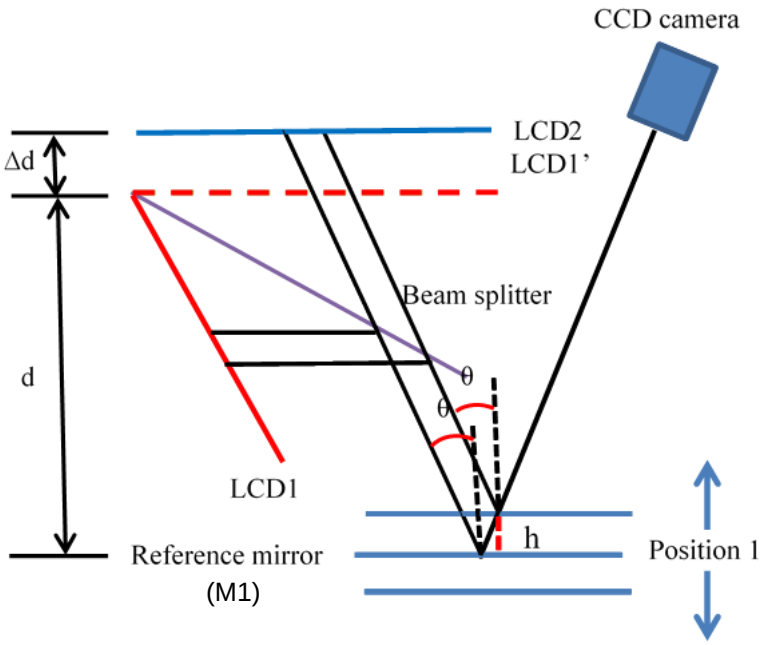

Figure 5. 8 Schematic calibration method of the 3D measurement system, prototype 2

Two high-precision planar mirrors are applied to calibrate parameters. The BS is set in a position, such that a virtual image LCD_1' of LCD_1 is parallel to LCD_2, two LCD screens are located at two different positions. Moreover, the two screens are parallel to the reference plane. The calibration mirror is fixed on a translation stage. The parallelism is established by repeating the adjustment of the relative orientations of the three components (the two LCD screens and the mirror at the reference plane) and generating pre-distorted fringe patterns for compensation. After the adjustment of the display screen and reference mirror is fixed, the calibration method and procedure are as following:

Step1: Calibrate the camera by using a chessboard in the depth of field.

Step2: Transferring the calibration mirror M1 to several known positions, and at each position, the fringe patterns reflected by the calibration mirror M1 are captured.

Step3: The M2 mirror replaces M1. It is fixed on the translation stage and moved to the middle position of the other M1 positions.

Step4: Set this position as the reference position. The two screens display the fringe pattern and circle ring texture pattern on both screens, the camera captures these images which are reflected by the calibration mirror and the mirror texture.

Step5: Calculate the absolute phase map and then use it for calculation Δd

Step6: Extract the centre markers of the texture image on the reference plane and the centre of the texture image on LCD1 at the reference position.

Step7: The external parameters of the LCD1 and reference plane are calculated by using the camera internal parameters and the coordinates of the mark points, namely the distance d.

The parameters of Δd and d need to be determined beforehand. In step2, M_1 is fixed on an accurate translating stage and moved to a known position Δh along the normal direction of the two LCD screens, as illustrated in Figure 5.8. At each mirror position, fringe pattern sets, having the optimum fringe numbers, are generated, and displayed on LCD_2 and LCD_1. The displayed fringe patterns are reflected by M_1 and captured by the CCD camera.

The geometric relationship in Figure 5.8 gives the relations as following:

$$(\varphi_{r1}{}' - \varphi_{r2})\frac{q}{2\pi} = \Delta d\tan\theta, \qquad 5.12$$

$$(d + \Delta h)\tan\theta - \Delta l = (d - \Delta h)\tan\theta \qquad 5.13$$

$$\Delta l = (\varphi_{m1}{}' - \varphi_{r1}{}')\frac{q}{2\pi}, \qquad 5.14$$

where the parameters q, d, Δd, Δl and θ have the same meaning as before. Δh is moving distance. The obtained absolute phase has the relationship

$$\Delta d = 2\Delta h(\varphi_{r1}{}' - \varphi_{r2})/\,(\varphi_{m1}{}' - \varphi_{r1}{}'). \qquad 5.15$$

In principle, one known depth Δh and the corresponding phase value can determine Δd. To improve the accuracy of Δd, the translating stage moves to several known positions to build an over-determined equation set.

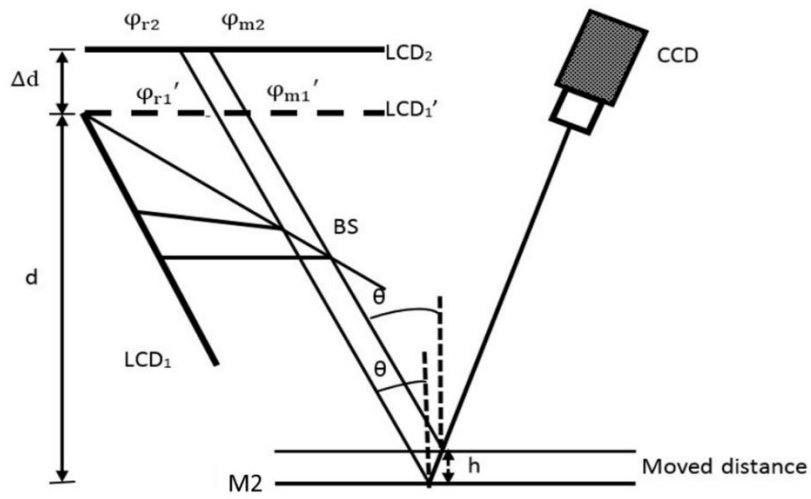

Figure 5. 9 Diagram of the calibration of d

To determine d, mirror M_2 is positioned parallel to the LCD screen and its surface is chosen as the reference plane, as illustrated in Figure 5.9. After calibrating the internal parameters of the CCD camera, the orientation of M_2 is determined in the camera coordinate system using the hollow ring marker matrix on the surface of M_2. The same hollow ring marker matrix is generated by software and displayed on the LCD_1 screen. Owing to the reflection from the surface of M_2, the CCD camera can view and capture the marker matrix at the position LCD_1" (the virtual image of LCD_1´). The orientation of LCD_1" (LCD_1´) is therefore obtained in the camera coordinate system using the hollow ring marker matrix on LCD_1. Distance d can be calculated using the obtained orientation of M_2 and LCD_1 in the same camera coordinate system.

Using the proposed calibration methods, the two parameters d and Δd were calibrated and their values are 154.532 mm and 17.905 mm respectively.

The layout has two advantages. 1) There are no moving parts during calibration and measurement, and there is thus no effect on the resultant data from moving

components. 2) Two sets of fringe patterns can be captured simultaneously by a colour CCD camera when the fringe patterns are coded into different colour channels of the two LCD screens.

5.4.2 Prototype 3 calibration

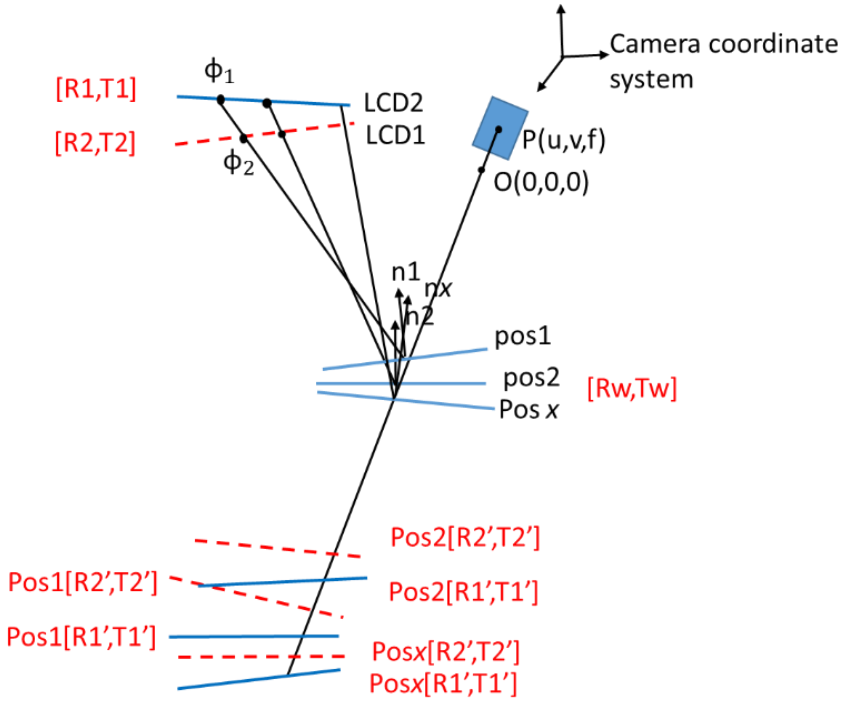

Figure 5. 10 Diagram of R/T matrices Calibration Method

Based on the measurement principle of prototype 3, the calibration process calculates the rotation and translation matrices (R and T) in Equation 5.8, namely, to obtain the positions of two LCDs. M1 is employed during the calibration. The mirror is positioned in different angles and positions, the two screens display chessboard images for which the size of the grids are known based on the LCD pixel size as shown in Figure 5.10. The camera captures two screens separately. Following the camera calibration procedure, the internal parameters of the camera and the virtual images external parameters can be obtained.

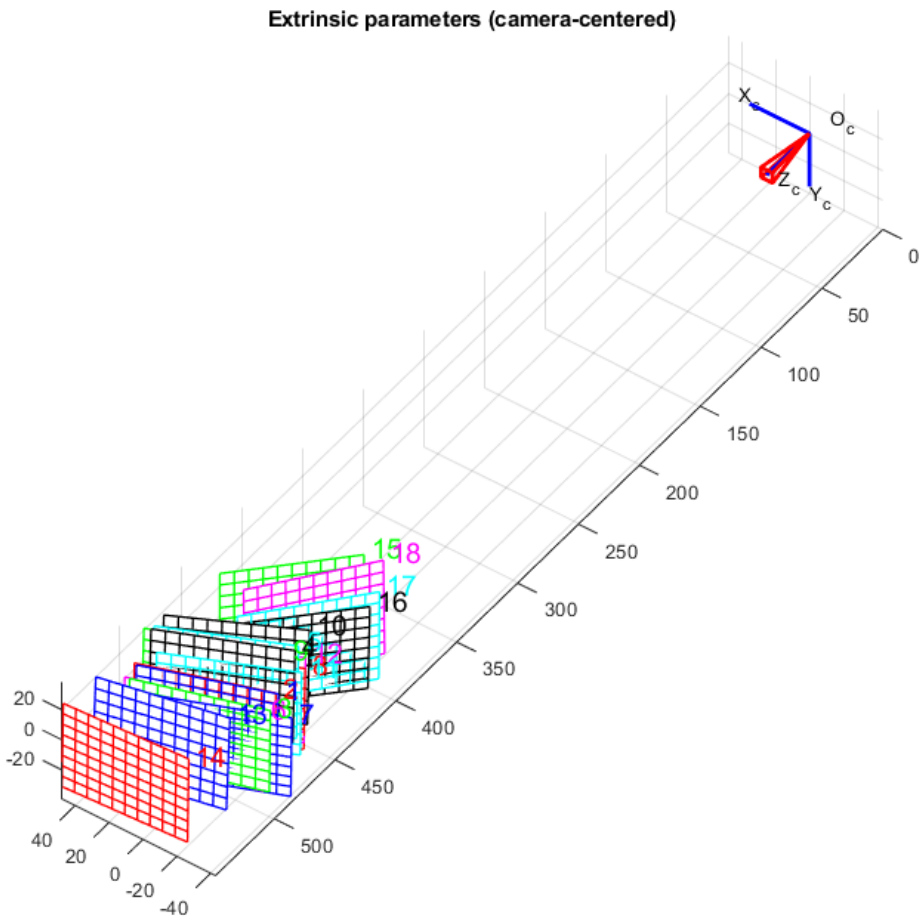

Figure 5. 11 The calibration results of camera

In fact, this results in the position of the virtual images of the LCDs, while the position of the actual LCDs can be converted as follows, namely, from R'T' to real RT in the camera coordinate system,

$$\begin{aligned} R^{'}(I-ee^{\mathrm{T}}) &= (I-2nn^{\mathrm{T}})R \\ T^{'} &= (I-2nn^{\mathrm{T}})T+2dn \end{aligned} \qquad 5.16$$

Where n is the M1 mirror normal vector in the camera coordinate, I is the 3×3 identity matrix, e is $[0\ \ 0\ \ 1]^{\mathrm{T}}$, d is the distance between the mirror and camera along n vector. According to the P3P method[186][101] and Mahalanobis[187] distance criterion, the real LCDs positions can be calibrated. Table 5.1 Table 5.2 and Table 5.3 show the calibration results.

Table 5. 1 Internal parameters of camera

1.0919e+04	0	1.1106e+03
0	1.0776e+04	1.0019e+03
0	0	1

Table 5. 2 [R1,T1] matrix

0.5207	0.0580	-0.8518	171.7818
-0.0642	0.9975	0.0287	-2.0585
0.8513	0.0398	0.5231	335.2081
0	0	0	1

Table 5. 3 [R2 T2] matrix

-0.8425	-0.1989	0.5006	142.0636
-0.3346	0.9215	-0.1969	-5.8015
-0.4222	-0.3334	-0.8430	315.2481
0	0	0	1

5.4.3 Chromatic aberration calibration

In both fringe projection system and deflectometry system, colour fringes are used for fast measurement as they have more information compared to monochrome fringes. By capturing coloured fringe patterns, the phase information can be retrieved from the two or three colour channels at the same time as shown in Figure 5.12, which can decrease the number of captured images. However, chromatic aberration and crosstalk will become problems in the measurement. Therefore, chromatic aberration compensation is necessary.

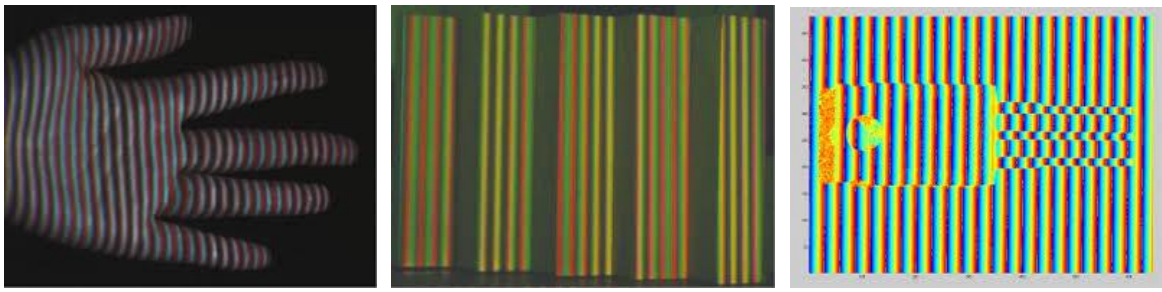

Figure 5. 12 Applications of multi-colour channels acquisition in fringe projection system

A series of colour fringes are used to calculate phase value, which aims to increase the measurement speed and capturing efficiency in the deflectometry system. Due to

the different refractive indices in different colour channels, refraction aberration occurs between different colour channels when a light beam passes through an optical lens. This would affect the phase measurement accuracy. The method for compensating chromatic aberration is to use an LCD screen (or projector) to generate red, green, and blue sinusoidal fringe patterns in turn. The colour CCD camera captures the red, green, and blue fringe patterns in front of the screen respectively. The sequential fringe patterns can be calculated using the phase-shifting algorithm with an optimised three-fringe number selection to find the absolute phase maps corresponding to the three colour channels. Selecting one colour as the datum colour channel, the phase difference can be calculated by comparing the other two colour channels with it. The phase difference between red and blue colour channels (as an example) can be represented as Equation 5.17:

$$\Delta\phi_{rb}(x,y) = \varphi_r(x,y)\text{-}\varphi_b(x,y) \qquad 5.17$$

Where $\Delta\phi_{rb}$ is the phase difference between red and blue channels, φ_r is the absolute phase in the red channel, φ_b is the absolute phase in the blue channel, x and y are the row and column of the pixels. The screen displays two sets of red and blue fringe patterns with the same number of fringes. Because of chromatic aberration, the number of captured fringes in the red channel and blue channel are differently denoted as a fringe aberration FA_{rb}. If the fringe aberration can be calculated from the phase difference, the chromatic aberration can then be corrected on the screen or the projector where the fringe patterns are displayed or projected. There is a ratio relationship between phase difference and fringe aberration as demonstrated in Equation 5.18:

$$\frac{FA_{rb}(x,1)}{F} = \frac{\Delta\phi_{rb}(x,end)-\Delta\phi_{rb}(x,1)}{\varphi_b(x,end)-\varphi_b(x,1)} \qquad 5.18$$

where F is the number of projected or displayed fringes, FA_{rb} is the fringe aberration, $\varphi_b(x,end)$-$\varphi_b(x,1)$ is the phase range for each row, $\Delta\phi_{rb}(x,end) - \Delta\phi_{rb}(x,1)$ is the phase difference range for each row across the field. After getting FA_{rb} , the screen (or projector) displays the number of fringes as F-FA_{rb} instead of the original number F, which can correct the chromatic aberration. Some experiment results are shown in Figure 5.13. Y-axis is the fringe number difference between the red channel and the blue channel. In the measurement process, the number of blue fringes is subtracted from the difference of the number of fringes to generate new fringe patterns for display,

which realises the correction of the colour difference of the red and blue channels. The same method is used for other colour channels.

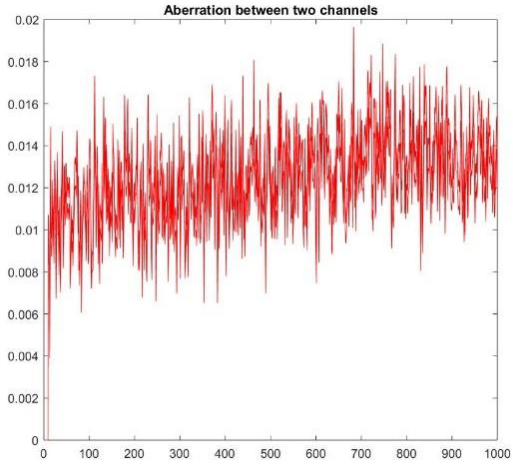

Figure 5. 13 The fringe aberration between the red and blue channels for all columns

5.5 Experiment

Two measurement systems, as illustrated in Figure 5.14, were developed to obtain the 3D shape of specular objects by displaying the same fringe pattern onto two LCD screens. Prototype 2 consists of a computer, a CCD camera, two LCD screens and a plane BS. The two LCD screens are from LG Electronics Inc. The CCD camera is the industrial camera from SVS Company with the model number ECO655 and a resolution of 2050 × 2448 pixels. The camera supports external and internal trigger modes. The relative positions of the two LCDs and BS were adjusted to let LCD_2 be parallel to the virtual image LCD_1' of LCD_1. After the parameters of Δd and d were calibrated using the method described above, the 3D shape of the specular surface could be measured by the developed system. Prototype 3 consists of a computer, a CCD camera, two LCD screens and a plane BS. The two LCD screens are iPad mini4. The CCD camera is the industrial camera from Ximea Company with the model number MQ042CG-CM and a resolution of 2048 × 2048 pixels. Two LCDs can be placed freely without the restriction of position.

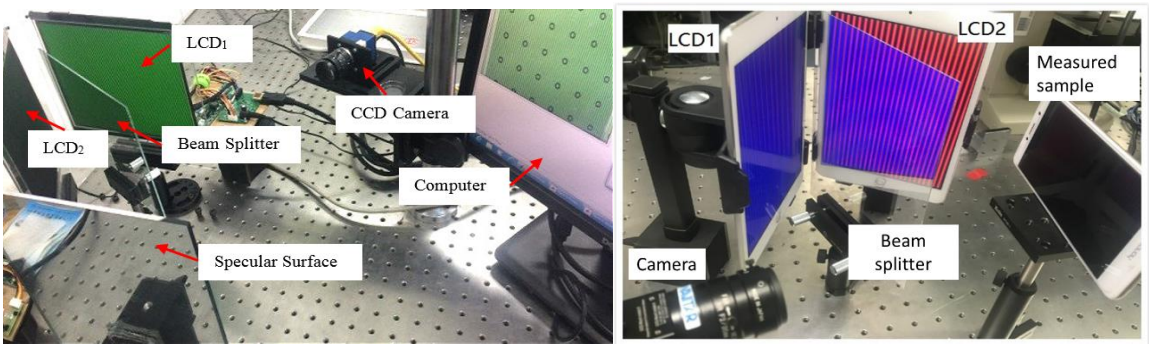

Figure 5. 14 Hardware of the prototype 2 system and prototype 3 system

To evaluate the accuracy of the 3D measurement system, the plate mirror M_1 was placed on an accurate translating stage with a resolution of 1 μm. The plate was positioned at −3.7, −1.3, 1.3 and 3.7 mm with respect to the reference plane. At each position, depth data were calculated. The translating distance of the stage, the measured average distance and absolute error (i.e., absolute difference between the measured average distance and position of the stage) are listed in Table 5.4. The maximum absolute error was smaller than 0.064 mm. The results clearly show that the proposed calibration method accurately converts the absolute phase into depth data. Due to the fact that all the points on one plane mirror have the same depth value to the reference plane in principle, the flatness of the plane can be used to calculate the repeatability of the measurement in the same condition. The repeatability value of the measurement is revealed by measuring a mirror plane 10 times.

Table 5. 4 Experimental results for the accurately positioned mirror (Unit: mm)

Position of the mirror	-3.7	-1.3	1.3	3.7
Measured distance	-3.764	-1.353	1.341	3.743
Absolute error	0.064	0.053	0.041	0.043

In order to further test the accuracy of the 3D measuring system, an artificial step artifact with discontinuous specular surfaces has been designed and manufactured, as illustrated in Figure 5.15. The distance between neighbouring steps was measured by a coordinate measuring machine (CMM). Twelve sinusoidal fringe patterns having optimum fringe numbers of 64, 63 and 56 were generated by software and sequentially displayed on the two LCD screens. The fringe patterns reflected by the specular surface of the artificial step were captured by the CCD camera. Depth data were obtained from the captured fringe patterns, as illustrated in Figure 5.15. As listed in

Table 5.5, the measurement results obtained by the deflectometry system were compared to that by obtained from the CMM method. The maximum absolute error was 0.052mm.

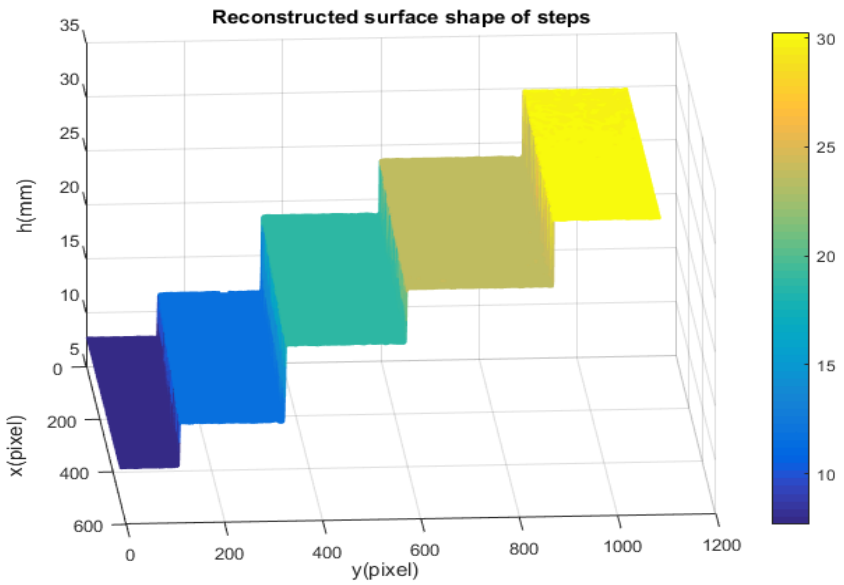

Figure 5. 15 Measured depth of the measured step

Table 5. 5 Experimental results on the measured step (Unit: mm)

Step distance	Measured distance	Absolute error
3.987	3.935	0.052
7.025	7.046	0.021
5.006	4.972	0.034
6.099	6.053	0.046

A monolithic multi-mirror array on the Mid-Infrared Instrument (MIRI) Spectrometer Optics for the James Webb Space Telescope, which has multiple discontinuous specular surfaces, was then measured by the developed 3D measurement system, as illustrated in Figure 5.16. Twelve sinusoidal fringe patterns having optimum fringe numbers of 64, 63 and 56 were generated by software and sequentially displayed on the two LCD screens. The fringe patterns reflected by the specular surface of the monolithic multi-mirror array were deformed and captured by the triggered CCD camera from another viewpoint. Using the four-step phase-shift algorithm, three wrapped phase maps were calculated for the measured specular object, as shown in Figure 5.17(a)–(c). The absolute phase of each pixel was determined using the optimum three-fringe selection method, as shown in Figure 5.17(d). Depth data were obtained as shown in Figure 5.18. Because the reflected fringe patterns by the

connecting surface cannot be seen by the CCD camera, only step surface data without the connecting surfaces are obtained. The results show that the proposed method can directly measure a specular object having isolated and/or discontinuous surfaces. In order to capture the reflected fringe patterns by the multiple surfaces, the base surface of the monolithic multi-mirror arrays needs to have an angle with respect to the reference plane. Therefore, the calculated depth data on both two groups (Mirror 1 to Mirror 11 and Mirror 12 to Mirror 21) have a positive slope.

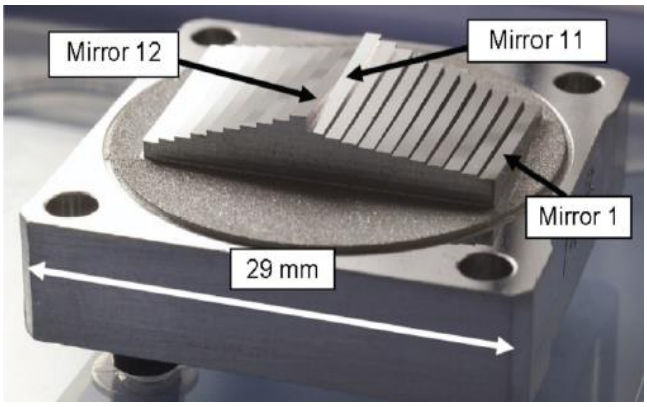

Figure 5. 16 A monolithic multi-mirror array on the MIRI Spectrometer Optics for the James Webb Space Telescope

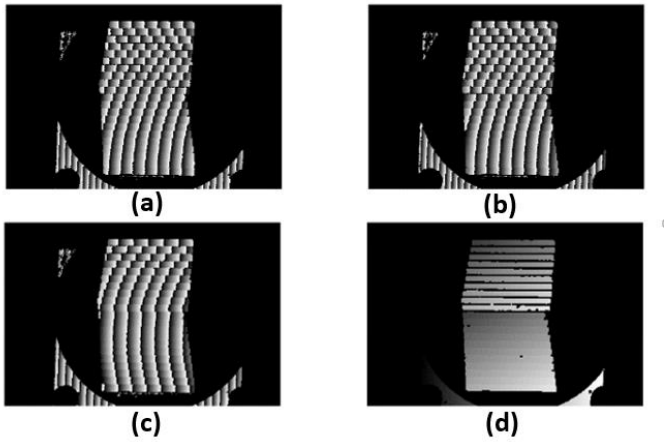

Figure 5. 17 Phase of the monolithic multi-mirror array. (a), (b), (c) are three wrapped phase maps having 64, 63 and 56 projected fringes, while (d) is the absolute phase map

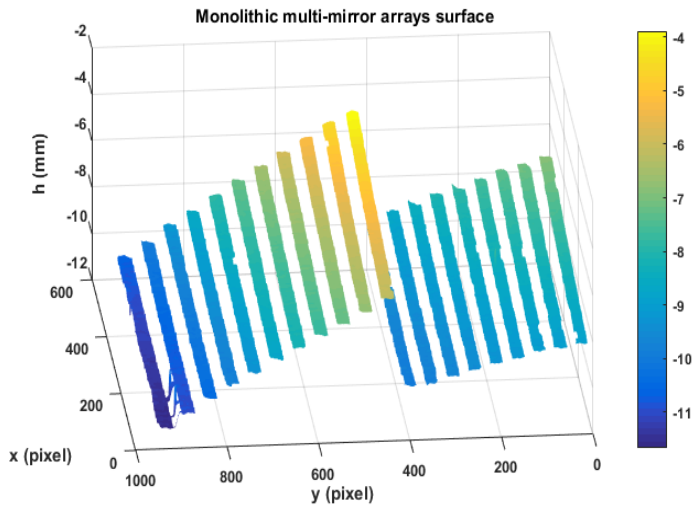

Figure 5. 18 Measured depth of the monolithic multi-mirror array

5.6 Summary

This chapter provided a theoretical and experimental investigation of specular surface measurement based on deflectometry technique. Three-generation systems were developed to measure the full-field 3D shape of the complex specular surface with colour fringe measurement. Prototype 1 system consisted of one camera, one LCD screen, and a translation stage. The depth information of the measured object could be obtained after a single movement. However, this method needs to move the screen during measurement, so the measurement time was increased, and the measurement accuracy also depended on the precision of the translation stage. Prototype 2 system consisted of one camera, two LCD screens, and a beam splitter (BS), which improved the moving issue. Using a BS to change the optical path, prototype 2 achieved the requirement of all hardware fixed. A mathematical model with geometric relations of parallel planes were derived to directly relate an absolute phase map to depth data, instead of the gradient. All equipment was fixed but has certain position relation limitations. Prototype 3 system avoided position limitations, it was flexible fixed components to get rid of the restriction of position relationship. System calibration methods were reported. Experimental results showed that the proposed developed DPMD method can obtain the full-field 3D shape of specular objects having discontinuous or complex geometrical surfaces accurately and effectively and as a result, DPMD could be used as a complimentary fast acquisition inspection tool for post processed AM parts

Chapter 6 Conclusions and Future work

6.1 Conclusions

This thesis mainly studies two technologies, fringe projection technology and deflectometry technology. Based on the measurement principles of these two technologies, the author developed calibration methods, implemented phase analysis algorithms, error correction algorithms, and these improved the measurement accuracy of the systems. In addition, the fringe projection system was embedded in a commercial EBM machine.

For the fringe projection technique, an in-situ inspection system was investigated in order to acquire and reconstruct the 3D shape of the powder bed and printed parts in an EBM machine. A novel surface fitting algorithm was developed in the system calibration protocol to improve measurement accuracy and vertical resolution, this reduced the influence of phase error and random noise. The accuracy of the inspection system was improved from 32.5 μm to 15.8 μm by implementing the improved calibration method. The vertical measurement resolution is around 20 μm. Another novel system calibration method was investigated to eliminate phase error from calibration board marks in fringe projection system. The reference coordinate system was established by using the whiteboard in the depth calibration process. Compared with the proposed fitting phase method, the advantage of this method is that the true depth is retained and the measurement results are closer to the original model. The disadvantage is that the accuracy of transverse data is not high, because the depth of transverse calibration is obtained through the proposed system, and the depth measurement accuracy of the system is 10 microns. One based on LUT for nonlinear calibration was investigated, this can be used in both fringe projection and deflectometry systems. The simulated and actual experimental data have shown the validity and feasibility of the proposed inspection technique. For powder bed inspection or other rough surfaces, the measurement speed is around 2 secs which therefore facilitates in situ metrology.

After electron beam melting, the powder is solidified and the reflective characteristic of the surface changes from diffuse to reflective. This phenomenon increases the difficulty for in-situ measurement systems when attempting to measure both diffuse

powder and reflective metal surfaces and this requires optimal setting of the exposure time and pixel saturation threshold. A novel intelligent fringe projection technique using the SVM algorithm is used to measure such high dynamic range surfaces. The exposure time and saturation pixel number of different surfaces were used as training features and the inspected surfaces are classified and predicted by an SVM classifier. The correct recognition rate is better than 91% on the printed samples, which indicates the proposed training method can effectively predict the measurement surface. The developed system can measure the powder bed and the printed sample as the same time. The measurement time was under 5 seconds during this inspection.

After 3D shape rough and reflective surfaces was obtained, the author also studied a 3D shape measurement method for specular or ultra- precision surfaces (resulting from post processing of AM components). A deflectometry technique was investigated for specular surface inspection. Three-generations of systems were developed to measure the full-field 3D shape of the complex specular surface with colour fringe measurement. A mathematical model including the geometric relations of the CCD and LCD was derived to directly relate an absolute phase map to depth data, instead of the gradient. Prototype 1 system consisted of one camera, one LCD screen, and a translation stage to measure the depth information of the measured object, which needs to move the screen during measurement. Prototype 2 system was considered to fix all equipment without transformation, which consisted of one camera, two LCD screens, and a beam splitter(BS). All equipment was fixed but has certain position relation limitations. Prototype 3 system tried to avoid position limitations, it was flexible with fixed components to get rid of the restriction of position relationship. System calibration methods were investigated. All deflectometry systems, colour fringes were applied to improve the efficiency of measurement. However, chromatic aberration was involved, which can lead to a system error. The chromatic aberration was compensated. Through the number of fringes pre-process, namely the original fringes plus or minus the number difference between the different colour channels. Consequently system error was compensated. Experimental results showed that the proposed developed DPMD method could obtain the full-field 3D shape of specular objects having discontinuous or complex geometrical surfaces accurately and

effectively. The maximum measurement error was 52 μm. As a result, DPMD could be used as a complimentary fast acquisition inspection tool for post processed AM parts.

Overall, this thesis investigated the principle, apparatus, algorithm and operation of both fringe projection system and deflectometry system, viewed as complimentary system for AM quality assurance. The two systems were established and the mathematical models were established. Different calibration methods are studied to realize the measurement function of the systems for different roughness surfaces inspection. The effects of errors in different systems were analysed and corrected. The fringe projection system is now fully integrated into the build cycles of the AM machine providing a “closed door”, high-speed measurement process.

6.2 Future work

Based on current research, there are still areas for improvement.

For the fringe projection system, calibration of projector needs to be further studied. The distortion of projector lens can be corrected by the calibration of projector, and the position relationship between projection pixel and camera pixel can also be calibrated. Eliminating nonlinear effects pixel by pixel is also meaningful.

The projector model Light Crafter 4500 has uneven projection illumination issue. This issue would affect image recolonization and exposure time prediction. The fringe projection system needs to be modified to deal with the uneven intensity of projector for nonlinear effects corrections and increasing prediction correct rate.

Current powder bed measurement speed was 2 seconds and the HDR surfaces measurement was 5 seconds. 12 fringes need to be projected onto the surfaces. Therefore, optimizing the acquisition algorithm needs to be investigated to improve capture speed to 1 sec or less. A methodology that can reduce the number of fringe need to be studied for HDR measurement, at present, the method investigated still requires two measurements. Due to the different reflectivity of the printed surface and the powder, the measurement time could be reduced in the future. A high accuracy measurement method which is based on measuring different surface roughness’s and an adaptive intelligent fringe projection needs to researched in order to realize multiple examples of surface reflectivity through a single measurement.

Reconstruction accuracy could be improved. A method that can improve the measurement accuracy in the depth direction in order to get high resolution in fringe projection system would be highly beneficial. For high precision and fine parts using finer powders, the measurement accuracy still needs to be improved to under 10 μm. In addition, it needs to consider the influence of phase error and ambient light and production conditions on the measurement environment.

For deflectometry system, the measurement accuracy was 52 μm, which is lower than the methods obtained shape map from slope by integration. A method can measure depth data of discontinues surfaces from phase map directly with high measurement accuracy need to be developed.

In both systems, automation and intelligent control need to be involved in the future. A variety of machine learning algorithms need to be applied to increase the intelligence of the systems. Feature extraction, image recognition and other machine vision algorithms need to be applied in the classification and recognition of defects and automation feedback in the future.

The inspection data from the current systems need to be combined with other in process non-spatial inspection data to give multi-dimensional data. Efficient data fusion would then need to be to be considered.

Finally error analysis needs to be further studied. Additional sources of error could be analysed, the influence of the refraction of light in vacuum environment on system measurement accuracy according to the actual measurement system, crosstalk effect in colour measurement system, etc. should considered in the future research.

References

[1] Townsend A, Senin N, Blunt L, Leach RK, Taylor JS. Surface texture metrology for metal additive manufacturing: a review. Precision Engineering. 2016 Oct 1;46:34-47.

[2] Herderick E. Additive manufacturing of metals: A review. Materials science and technology. 2011 Oct 16;1413.

[3] Bourell DL, Leu MC, Rosen DW. Roadmap for additive manufacturing: identifying the future of freeform processing. The University of Texas at Austin, Austin, TX. 2009 Mar:11-5.

[4] Everton SK, Hirsch M, Stravroulakis P, Leach RK, Clare AT. Review of in-situ process monitoring and in-situ metrology for metal AM. Materials & Design. 2016 Apr 5; 95:431-45.

[5] https://www.iso.org/standard/69669.html

[6]Rieder H, Dillhöfer A, Spies M, Bamberg J, Hess T. Online monitoring of additive manufacturing processes using ultrasound. In11th European Conference on Non-Destructive Testing (ECNDT), Prague, Czech Republic, Oct 2014 Oct 6 (pp. 6-10).

[7]Zhang Y, Guo Y, Chen Y, Kang L, Cao Y, Qi H, Yang S. Ultrasonic-Assisted Laser Metal Deposition of the Al 4047Alloy. Metals. 2019 Oct;9(10):1111.

[8] https://www.sciaky.com/additive-manufacturing/wire-vs-powder

[9] Foster BK, Reutzel EW, Nassar AR, Hall BT, Brown SW, Dickman CJ. Optical layerwise monitoring of powder bed fusion. In Proc. 2015 Solid Freeform Fabrication Symposium, Austin, TX. 2015 Aug; pp: 10-12.

[10] Martin KF. A review by discussion of condition monitoring and fault diagnosis in machine tools. International Journal of Machine Tools and Manufacture. 1994 May 1; 34(4):527-51.

[11] Zhang ZH. Review of single-shot 3D shape measurement by phase calculation-based fringe projection techniques. Optics and Lasers in Engineering. 2012 Aug 1; 50(8):1097-106.

[12] Zhang S, Van Der Weide D, Oliver J. Superfast phase-shifting method for 3-D shape measurement. Optics express. 2010 Apr 26;18(9):9684-9.

[13] Zhang S, Yau ST. High-resolution, real-time 3D absolute coordinate measurement based on a phase-shifting method. Optics Express. 2006 Apr 3;14(7):2644-9.

[14] Li EB, Peng X, Xi J, Chicharo JF, Yao JQ, Zhang DW. Multi-frequency and multiple phase-shift sinusoidal fringe projection for 3D profilometry. Optics express. 2005 Mar 7;13(5):1561-9.

[15] Liu Y, Blunt L, Zhang Z, Rahman HA, Gao F, Jiang X. In-situ areal inspection of powder bed for electron beam fusion system based on fringe projection profilometry. Additive Manufacturing. 2020 Jan 1;31:100940.

[16] Liu Y, Blunt LA, Gao F, Jiang XJ. High-dynamic-range 3D measurement for E-beam fusion additive manufacturing based on SVM intelligent fringe projection system. Surface Topography: Metrology and Properties. 2021 Jun 17.

[17] Liu Y, Blunt L, Gao F, Jiang X. A Simple Calibration Method for a Fringe Projection System Embedded within an Additive Manufacturing Machine. Machines. 2021 Sep;9(9):200.

[18] Liu Y, Huang S, Zhang Z, Gao N, Gao F, Jiang X. Full-field 3D shape measurement of discontinuous specular objects by direct phase measuring deflectometry. Scientific reports. 2017 Aug 31;7(1):1-8.

[19] Huang S, Liu Y, Gao N, Zhang Z, Gao F, Jiang X. Distance calibration between reference plane and screen in direct phase measuring deflectometry. Sensors. 2018 Jan;18(1):144.

[20] Zhang Z, Wang Y, Huang S, Liu Y, Chang C, Gao F, Jiang X. Three-dimensional shape measurements of specular objects using phase-measuring deflectometry. Sensors. 2017 Dec;17(12):2835.

[21] Liu Y, Blunt L, Gao F, Jiang J. In-situ high dynamic range inspection in Ebeam machine based on fringe projection profilometry. In21st International Conference of the European Society for Precision Engineering and Nanotechnology 2021 Jun 10 (pp. 315-318). euspen.

[22] Blunt L, Liu Y, Zhang Z, Smith C, Knight D, Gao F, Townsend A, Jiang X. An in-process, layer wise surface metrology system for a new E-Beam additive manufacturing machine. In20th International Conference of the European Society for Precision Engineering and Nanotechnology 2020 Jun 8 (pp. 565-568). euspen.

[23] Liu Y, Zhang Z, Blunt L, Saunby G, Dawes J, Blackham B, Rahman HA, Smith C, Gao F, Jiang X. In-situ inspection system for additive manufacturing based on phase measurement profilometry. In19th International Conference of the European Society for Precision Engineering and Nanotechnology 2019 (pp. 324-327). euspen.

[24] Liu Y, Zhang ZH, Blunt L, Saunby G, Dawes J, Blackham B,et al. In-situ areal inspection of powder bed for electron beam fusion AM system based on fringe projection. 2018 ASPE and euspen Summer Topical Meeting, Berkeley, US, Volume 69:259-264

[25] Bourell D, Wohlers T. Introduction to Additive Manufacturing. Additive Manufacturing. 2020;24.

[26] Zitelli C, Folgarait P, Di Schino A. Laser powder bed fusion of stainless steel grades: a review. Metals. 2019 Jul;9(7):731.

[27] https://www.renishaw.com/en/metal-powders-for-am--31457

[28] Schmidt M, Merklein M, Bourell D, Dimitrov D, Hausotte T, Wegener K, Overmeyer L, Vollertsen F, Levy GN. Laser based additive manufacturing in industry and academia. Cirp Annals. 2017 Jan 1;66(2):561-83.

[29] Dunsky C. Process monitoring in laser additive manufacturing. Industrial laser solutions. 2014;29(5):14-8.

[30] Biamino S, Penna A, Ackelid U, Sabbadini S, Tassa O, Fino P, Pavese M, Gennaro P, Badini C. Electron beam melting of Ti–48Al–2Cr–2Nb alloy: Microstructure and mechanical properties investigation. Intermetallics. 2011 Jun 1;19(6):776-81.

[31] Bhavar V, Kattire P, Patil V, Khot S, Gujar K, Singh R. A review on powder bed fusion technology of metal additive manufacturing. Additive manufacturing handbook. 2017 May 19:251-3.

[32] Udroiu R. POWDER BED ADDITIVE MANUFACTURING SYSTEMS AND ITS APPLICATIONS. Academic journal of manufacturing engineering. 2012 Dec 1;10(4).

[33] Lazaros N, Sirakoulis GC, Gasteratos A. Review of stereo vision algorithms: from software to hardware. International Journal of Optomechatronics. 2008 Nov 26;2(4):435-62.

[34] Hu X, Mordohai P. A quantitative evaluation of confidence measures for stereo vision. IEEE transactions on pattern analysis and machine intelligence. 2012 Jan 31;34(11):2121-33.

[35] Tippetts B, Lee DJ, Lillywhite K, Archibald J. Review of stereo vision algorithms and their suitability for resource-limited systems. Journal of Real-Time Image Processing. 2016 Jan;11(1):5-25.

[36] Picture was taken from http://www.ni.com/white-paper/14103/en/

[37] Hamzah RA, Ibrahim H. Literature survey on stereo vision disparity map algorithms. Journal of Sensors. 2016 Nov;2016.

[38] Sivaraman S, Trivedi MM. A review of recent developments in vision-based vehicle detection. In2013 IEEE Intelligent Vehicles Symposium (IV) 2013 Jun 23 (pp. 310-315). IEEE.

[39] Hirschmuller H. Improvements in real-time correlation-based stereo vision. InProceedings IEEE Workshop on Stereo and Multi-Baseline Vision (SMBV 2001) 2001 Dec 9 (pp. 141-148). IEEE.

[40] Cui Y, Schuon S, Chan D, Thrun S, Theobalt C. 3D shape scanning with a time-of-flight camera. Computer Vision and Pattern Recognition (CVPR), 2010 IEEE Conference on 2010 Jun 13 (pp. 1173-1180). IEEE.

[41] Chen F, Brown G, Song M. Overview of three-dimensional shape measurement using optical methods. Optical Engineering. 2000 Jan 1; 39(1):10-22.

[42] Lange R, Seitz P. Solid-state time-of-flight range camera. IEEE Journal of quantum electronics. 2001 Mar;37(3):390-7.

[43] Chiabrando F, Chiabrando R, Piatti D, Rinaudo F. Sensors for 3D imaging: Metric evaluation and calibration of a CCD/CMOS time-of-flight camera. Sensors. 2009 Dec;9(12):10080-96.

[44] Druml N, Fleischmann G, Heidenreich C, Leitner A, Martin H, Herndl T, Holweg G. Time-of-flight 3D imaging for mixed-critical systems. In2015 IEEE 13th International Conference on Industrial Informatics (INDIN) 2015 Jul 22 (pp. 1432-1437). IEEE.

[45] Hussmann S, Ringbeck T, Hagebeuker B. A performance review of 3D TOF vision systems in comparison to stereo vision systems. Stereo vision. 2008 Nov 1;372.

[46] Dörband B, Seitz G. Interferometric testing of optical surfaces at its current limit. Optik-International Journal for Light and Electron Optics. 2001 Jan 1;112(9):392-8.

[47] Hariharan P. Basics of interferometry. Elsevier; 2010 Jul 28.

[48] Richard Thompson A, Moran JM, Swenson Jr GW. Interferometry and synthesis in radio astronomy. Springer Nature; 2017.

[49] Takasaki H. Moiré topography. Applied optics. 1970 Jun 1;9(6):1467-72.

[50] Jin L, Otani Y, Yoshizawa T. Shadow moiré profilometry by frequency sweeping. Optical Engineering. 2001 Jul;40(7):1383-6.

[51] Takeda M. Fringe formula for projection type moiré topography. Optics and lasers in Engineering. 1982 Jan 1;3(1):45-52.

[52] Idesawa M, Yatagai TI. General theory of projection-type moire topography. Sci. Papers IPCR. 1977;71:57-70.

[53] KuKim S, KiPaik J. Out-of-focus blur estimation and restoration for digital auto-focusing system. Electronics letters. 1998 Jun 11;34(12):1217-9.

[54] Kim SK, Park SR, Paik JK. Simultaneous out-of-focus blur estimation and restoration for digital auto-focusing system. IEEE Transactions on Consumer Electronics. 1998 Aug;44(3):1071-5.

[55] Lin J, Zhang C, Shi Q. Estimating the amount of defocus through a wavelet transform approach. Pattern Recognition Letters. 2004 Mar 1;25(4):407-11.

[56] Geng J. Structured-light 3D surface imaging: a tutorial. Advances in Optics and Photonics. 2011 Jun 30;3(2):128-60.

[57] Salvi J, Fernandez S, Pribanic T, Llado X. A state of the art in structured light patterns for surface profilometry. Pattern recognition. 2010 Aug 1;43(8):2666-80.

[58] Forbes A. Structured light from lasers. Laser & Photonics Reviews. 2019 Nov;13(11):1900140.

[59] Gu F, Cao H, Song Z, Xie P, Zhao J, Liu J. Dot-coded structured light for accurate and robust 3D reconstruction. Applied Optics. 2020 Nov 20;59(33):10574-83.

[60] Young M, Beeson E, Davis J, Rusinkiewicz S, Ramamoorthi R. Coded structured light. In2007 IEEE Conference on Computer Vision and Pattern Recognition 2007 Jun 17 (pp. 1-8). IEEE.

[61] Tsai MJ, Hung CC. Development of a high-precision surface metrology system using structured light projection. Measurement. 2005 Oct 1;38(3):236-47.

[62] Etzion T. Constructions for perfect maps and pseudorandom arrays. IEEE Transactions on information theory. 1988 Sep;34(5):1308-16.

[63] Petriu EM, Sakr Z, Spoelder HJ, Moica A. Object recognition using pseudo-random color encoded structured light. InProceedings of the 17th IEEE Instrumentation and Measurement Technology Conference [Cat. No. 00CH37066] 2000 May 1 (Vol. 3, pp. 1237-1241). IEEE.

[64] Petković T, Pribanić T, Đonlić M. Single-shot dense 3D reconstruction using self-equalizing De Bruijn sequence. IEEE Transactions on Image Processing. 2016 Aug 26;25(11):5131-44.

[65] Fan JT, Han C, Zhang C, Li MX, Bai BX, Yang HM. Study of a new decoding technology for De Bruijn structured light. Dianzi Xuebao(Acta Electronica Sinica). 2012 Mar;40(3):483-8.

[66] Pages J, Salvi J, Collewet C, Forest J. Optimised De Bruijn patterns for one-shot shape acquisition. Image and Vision Computing. 2005 Aug 1;23(8):707-20.

[67] Posdamer JL, Altschuler MD. Surface measurement by space-encoded projected beam systems. Computer graphics and image processing. 1982 Jan 1;18(1):1-7.

[68] Horn E, Kiryati N. Toward optimal structured light patterns. Image and Vision Computing. 1999 Feb 28;17(2):87-97.

[69] Zhang S. High-speed 3D shape measurement with structured light methods: A review. Optics and Lasers in Engineering. 2018 Jul 1;106:119-31.

[70] Jia P, Kofman J, English CE. Two-step triangular-pattern phase-shifting method for three-dimensional object-shape measurement. Optical Engineering. 2007 Aug;46(8):083201.

[71] Wu K, Xi J, Yu Y, Yang Z. 3D profile measurement based on estimation of spatial shifts between intensity ratios from multiple-step triangular patterns. Optics and Lasers in Engineering. 2013 Apr 1;51(4):440-5.

[72] Huang PS, Zhang S, Chiang FP. Trapezoidal phase-shifting method for three-dimensional shape measurement. Optical Engineering. 2005 Dec;44(12):123601.

[73] Bell T, Li B, Zhang S. Structured light techniques and applications. Wiley Encyclopedia of Electrical and Electronics Engineering. 1999 Dec 27:1-24.

[74] Zhang Z, Zhang D, Peng X. Performance analysis of a 3D full-field sensor based on fringe projection. Oprics and lasers in engineering.2004 Sep 1; 42(3):341-53.

[75] Jia P, Kofman J, English CE. Comparison of linear and nonlinear calibration methods for phase-measuring profilometry. Optical Engineering. 2007 Apr; 46(4):043601.

[76] Huang L, Chua PS, Asundi A. Least-squares calibration method for fringe projection profilometry considering camera lens distortion. Applied optics. 2010 Mar 20;49(9):1539-48.

[77] Hu Q; Huang PS; Fu Q; Chiang FP. Calibration of a three-dimensional shape measurement system. Optical Engineering 2003 Feb,42(2,487-93.

[78] Zhang Z; Ma H; Guo T; Zhang S; Chen J. Simple, flexible calibration of phase calculation-based three-dimensional imaging system. Optics letters 2011 Apr 1,36(7),1257-9.

[79] Windecker R; Fleischer M; Körner K; Tiziani H. Testing micro devices with fringe projection and white-light interferometry. Optics and Lasers in Engineering 2001 Aug 31, 36(2), 141-54.

[80] Sutton M; Zhao W; McNeill S; Schreier H; Chao YJ. Development and assessment of a single-image fringe projection method for dynamic applications. Experimental Mechanics 2001 Sep 24, 41(3),205-17.

[81] Huang PS, Hu Q, Jin F, Chiang FP. Color-encoded digital fringe projection technique for high-speed three-dimensional surface contouring. Optical Engineering. 1999 Jun 1; 38(6):1065-71.

[82] Reich C, Ritter R, Thesing J. 3-D shape measurement of complex objects by combining photogrammetry and fringe projection. Optical Engineering. 2000 Jan; 39(1):224-31.

[83] Quan C, He X, Wang CF, Tay C, Shang H. Shape measurement of small objects using LCD fringe projection with phase shifting. Optics Communications. 2001 Mar 1; 189(1):21-9.

[84] Guan C, Hassebrook LG, Lau DL. Composite structured light pattern for three-dimensional video. Optics Express. 2003 Mar 10; 11(5):406-17.

[85] Zhang S, Yau ST. High dynamic range scanning technique. Optical Engineering. 2009 Mar;48(3):033604.

[86] Ekstrand L, Zhang S. Autoexposure for three-dimensional shape measurement using a digital-light-processing projector. Optical Engineering. 2011 Dec;50(12):123603.

[87]Suresh V, Wang Y, Li B. High-dynamic-range 3D shape measurement utilizing the transitioning state of digital micromirror device. Optics and Lasers in Engineering. 2018 Aug 1;107:176-81.

[88] Salahieh B, Chen Z, Rodriguez JJ, Liang R. Multi-polarization fringe projection imaging for high dynamic range objects. Optics express. 2014 Apr 21;22(8):10064-71.

[89] Liang R. Short wavelength and polarized phase shifting fringe projection imaging of translucent objects. Optical Engineering. 2014 Jan;53(1):014104.

[90] Jiang H, Zhao H, Li X. High dynamic range fringe acquisition: a novel 3-D scanning technique for high-reflective surfaces. Optics and Lasers in Engineering. 2012 Oct 1;50(10):1484-93.

[91]Klinker GJ, Shafer SA, Kanade T. Image segmentation and reflection analysis through color. InApplications of Artificial Intelligence VI 1988 Mar 29 (Vol. 937, pp. 229-244). International Society for Optics and Photonics.

[92]Shen HL, Cai QY. Simple and efficient method for specularity removal in an image. Applied optics. 2009 May 10;48(14):2711-9.

[93] Knauer MC, Kaminski J, Hausler G. Phase measuring deflectometry: a new approach to measure specular free-form surfaces. InOptical Metrology in Production Engineering 2004 Sep 10 (Vol. 5457, pp. 366-376). International Society for Optics and Photonics.

[94] Tang Y, Su X, Wu F, Liu Y. A novel phase measuring deflectometry for aspheric mirror test. Optics express. 2009 Oct 26;17(22):19778-84.

[95] Zhang Z, Wang Y, Huang S, Liu Y, Chang C, Gao F, Jiang X. Three-dimensional shape measurements of specular objects using phase-measuring deflectometry. Sensors. 2017 Dec;17(12):2835.

[96] Huang L, Idir M, Zuo C, Asundi A. Review of phase measuring deflectometry. Optics and Lasers in Engineering. 2018 Aug 1;107:247-57.

[97] Tang Y, Su X, Liu Y, Jing H. 3D shape measurement of the aspheric mirror by advanced phase measuring deflectometry. Optics express. 2008 Sep 15;16(19):15090-6.

[98] Zhou T, Chen K, Wei H, Li Y. Improved method for rapid shape recovery of large specular surfaces based on phase measuring deflectometry. Applied optics. 2016 Apr 1;55(10):2760-70.

[99] Krasinski J, Heller DF, Kafri O. Phase object microscopy using moire deflectometry. Applied optics. 1985 Sep 15;24(18):3032-6.

[100] Xu Y, Gao F, Jiang X. A brief review of the technological advancements of phase measuring deflectometry. PhotoniX. 2020 Dec;1:1-0.

[101] Ren H, Gao F, Jiang X. Iterative optimization calibration method for stereo deflectometry. Optics express. 2015 Aug 24;23(17):22060-8.

[102] Xu Y, Gao F, Jiang X. Performance analysis and evaluation of geometric parameters in stereo deflectometry. Engineering. 2018 Dec 1;4(6):806-15.

[103] Guo H, Tao T. Specular surface measurement by using a moving diffusive structured light source. InOptical Design and Testing III 2007 Nov 28 (Vol. 6834, p. 68343E). International Society for Optics and Photonics.

[104] Liu Y, Lehtonen P, Su X. High-accuracy measurement for small scale specular objects based on PMD with illuminated film. Optics & Laser Technology. 2012 Mar 1;44(2):459-62.

[105] Feng S, Chen Q, Gu G, Tao T, Zhang L, Hu Y, Yin W, Zuo C. Fringe pattern analysis using deep learning. Advanced Photonics. 2019 Feb;1(2):025001.

[106] Zhang L, Chen Q, Zuo C, Feng S. High-speed high dynamic range 3d shape measurement based on deep learning. Optics and Lasers in Engineering. 2020 Nov 1;134:106245.

[107] Xiang S, Deng H, Wu J, Zhu C. Absolute phase unwrapping with SVM for fringe-projection profilometry. IET Image Processing. 2020 Apr 15;14(12):2645-51.

[108] Spoorthi GE, Gorthi S, Gorthi RK. PhaseNet: A deep convolutional neural network for two-dimensional phase unwrapping. IEEE Signal Processing Letters. 2018 Nov 1;26(1):54-8.

[109] Yan K, Yu Y, Huang C, Sui L, Qian K, Asundi A. Fringe pattern denoising based on deep learning. Optics Communications. 2019 Apr 15;437:148-52.

[110] Huang L, Kemao Q, Pan B, Asundi AK. Comparison of Fourier transform, windowed Fourier transform, and wavelet transform methods for phase extraction from a single fringe pattern in fringe projection profilometry. Optics and Lasers in Engineering. 2010 Feb 1;48(2):141-8.

[111] Kemao Q. Windowed Fourier transform for fringe pattern analysis. Applied Optics. 2004 May 1;43(13):2695-702.

[112] Kemao Q, Wang H, Gao W. Windowed Fourier transform for fringe pattern analysis: theoretical analyses. Applied optics. 2008 Oct 10;47(29):5408-19.

[113] Kemao Q. Two-dimensional windowed Fourier transform for fringe pattern analysis: principles, applications and implementations. Optics and Lasers in Engineering. 2007 Feb 1;45(2):304-17.

[114]Gdeisat MA, Burton DR, Lalor MJ. Spatial carrier fringe pattern demodulation by use of a two-dimensional continuous wavelet transform. Applied optics. 2006 Dec 1;45(34):8722-32.

[115] Zhong J, Zeng H. Multiscale windowed Fourier transform for phase extraction of fringe patterns. Applied Optics. 2007 May 10;46(14):2670-5.

[116] Trusiak M, Służewski Ł, Patorski K. Single shot fringe pattern phase demodulation using Hilbert-Huang transform aided by the principal component analysis. Optics Express. 2016 Feb 22;24(4):4221-38.

[117] Gdeisat M, Burton D, Lilley F, Arevalillo-Herráez M. Fast fringe pattern phase demodulation using FIR Hilbert transformers. Optics Communications. 2016 Jan 15;359:200-6.

[118] Chen W, Su X, Cao YP, Zhang QC, Xiang LQ. Method for eliminating zero spectrum in Fourier transform profilometry. Optics and Lasers in Engineering. 2005 Nov 1;43(11):1267-76.

[119] Luo F, Chen W, Su X. Eliminating zero spectra in Fourier transform profilometry by application of Hilbert transform. Optics Communications. 2016 Apr 15;365:76-85.

[120] Yan K, Yu Y, Sun T, Asundi A, Kemao Q. Wrapped phase denoising using convolutional neural networks. Optics and Lasers in Engineering. 2020 May 1;128:105999.

[121] Zhang H, Su H. Wrapped phase based SVM method for 3D object recognition. In2009 2nd IEEE International Conference on Computer Science and Information Technology 2009 Aug 8 (pp. 206-209). IEEE.

[122] Takeda M, Mutoh K. Fourier transform profilometry for the automatic measurement of 3-D object shapes. Applied optics. 1983 Dec 15;22(24):3977-82.

[123] Zuo C, Feng S, Huang L, Tao T, Yin W, Chen Q. Phase shifting algorithms for fringe projection profilometry: A review. Optics and Lasers in Engineering. 2018 Oct 1;109:23-59.

[124] Yamaguchi I, Zhang T. Phase-shifting digital holography. Optics Letters. 1997 Aug 15; 22(16):1268-70.

[125] Pan B, Kemao Q, Huang L, Asundi, A. Phase error analysis and compensation for nonsinusoidal waveforms in phase-shifting digital fringe projection profilometry. Optics Letters. 2009; 34(4), 416-418.

[126] Kaplan ST, Ulrych TJ. Phase unwrapping: a review of methods and a novel technique. InCSPG CSEG Convention 2007 May (pp. 534-537).

[127] Judge TR, Bryanston-Cross PJ. A review of phase unwrapping techniques in fringe analysis. Optics and Lasers in Engineering. 1994 Jan 1;21(4):199-239.

[128] Chan PH, Bryanston-Cross PJ, Parker SC. Fringe-pattern analysis using a spatial phase-stepping method with automatic phase unwrapping. Measurement Science and Technology. 1995 Sep 1;6(9):1250.

[129] Huntley JM, Saldner H. Temporal phase-unwrapping algorithm for automated interferogram analysis. Applied Optics. 1993 Jun 10;32(17):3047-52.

[130] Saldner HO, Huntley JM. Temporal phase unwrapping: application to surface profiling of discontinuous objects. Applied optics. 1997 May 1;36(13):2770-5.

[131] Huntley JM, Saldner HO. Shape measurement by temporal phase unwrapping: comparison of unwrapping algorithms. Measurement Science and Technology. 1997 Sep;8(9):986.

[132] Huntley JM, Saldner HO. Error-reduction methods for shape measurement by temporal phase unwrapping. JOSA A. 1997 Dec 1;14(12):3188-96.

[133] Reich C, Ritter R, Thesing J. White light heterodyne principle for 3D-measurement. Sensors, Sensor Systems, and Sensor Data Processing 1997 Sep 25 (Vol. 3100, pp. 236-244). International Society for Optics and Photonics.

[134] Petz M, Tutsch R. Reflection grating photogrammetry: a technique for absolute shape measurement of specular free-form surfaces. Optical Manufacturing and Testing VI 2005 Aug 18 (Vol. 5869, p. 58691D). International Society for Optics and Photonics.

[135] Towers CE, Towers DP, Jones JD. Optimum frequency selection in multifrequency interferometry. Optics Letters. 2003 Jun 1;28(11):887-9

[136] Towers CE, Towers DP, Jones JD. Absolute fringe order calculation using optimised multi-frequency selection in full-field profilometry. Optics and Lasers in Engineering. 2005 Jul 1;43(7):788-800.

[137] Zhang Z, Towers CE, Towers DP. Time efficient color fringe projection system for 3D shape and color using optimum 3-frequency selection. Optics express. 2006 Jul 10;14(14):6444-55.

[138] Everton SK, Hirsch M, Stravroulakis P, Leach RK, Clare AT. Review of in-situ process monitoring and in-situ metrology for metal additive manufacturing. Materials & Design. 2016 Apr 5;95:431-45.

[139] Berumen S, Bechmann F, Lindner S, Kruth JP, Craeghs T. Quality control of laser-and powder bed-based Additive Manufacturing (AM) technologies. Physics procedia. 2010 Jan 1; 5:617-22.

[140] Pavlov M, Doubenskaia M, Smurov I. Pyrometric analysis of thermal processes in SLM technology. Physics Procedia. 2010 Jan 1; 5:523-31.

[141] Hu D, Kovacevic R. Sensing, modeling and control for laser-based additive manufacturing. International Journal of Machine Tools and Manufacture. 2003 Jan 1; 43(1):51-60.

[142] Grasso M, Colosimo BM. Process defects and in situ monitoring methods in metal powder bed fusion: a review. Measurement Science and Technology. 2017 Feb 15;28(4):044005.

[143] Shrestha S, Chou K. A build surface study of powder-bed electron beam additive manufacturing by 3D thermo-fluid simulation and white-light interferometry. International Journal of Machine Tools and Manufacture. 2017 Oct 1; 121:37-49.

[144] Zhang B, Ziegert J, Farahi F, Davies A. In situ surface topography of laser powder bed fusion using fringe projection. Additive Manufacturing. 2016 Oct 31; 12:100-7.

[145] Townsend A, Racasan R, Blunt L. Surface-specific additive manufacturing test artefacts. Surface Topography: Metrology and Properties. 2018 May 16;6(2):024007.

[146] Gomez C, Su R, Thompson A, DiSciacca J, Lawes S, Leach RK. Optimization of surface measurement for metal additive manufacturing using coherence scanning interferometry. Optical Engineering. 2017 Jul;56(11):111714.

[147] Croom, B. P., Bumgardner, C., & Li, X. (2016). Unveiling residual stresses in air plasma spray coatings by digital image correlation. Extreme Mechanics Letters, 7, 126-135.

[148] Bartlett, J. L., Croom, B. P., Burdick, J., Henkel, D., & Li, X. (2018). Revealing mechanisms of residual stress development in additive manufacturing via digital image correlation. Additive Manufacturing, 22, 1-12.

[149] Bartlett, J. L., & Li, X. (2019). An overview of residual stresses in metal powder bed fusion. Additive Manufacturing.

[150] Holzmond, O., & Li, X. (2017). In situ real time defect detection of 3D printed parts. Additive Manufacturing, 17, 135-142.

[151] Southon N, Stavroulakis P, Goodridge R, Leach R. In-process measurement and monitoring of a polymer laser sintering powder bed with fringe projection. Materials & Design. 2018 Nov 5; 157:227-34.

[152] Tammas-Williams S, Zhao H, Léonard F, Derguti F, Todd I, Prangnell PB. XCT analysis of the influence of melt strategies on defect population in Ti–6Al–4V components manufactured by Selective Electron Beam Melting. Materials Characterization. 2015 Apr 30; 102:47-61.

[153] Zanini F, Carmignato S. X-ray computed tomography for measurement of additively manufactured metal threaded parts. InProceedinf of ASPE/euspen Summer Topical Meeting 2018.

[154] Pears N, Liu Y, Bunting P, editors. 3D imaging, analysis and applications. New York: Springer; 2012 May 22

[155] Sidambe AT. Three dimensional surface topography characterization of the electron beam melted Ti6Al4V. Metal powder report. 2017 May 1;72(3):200-5.

[156] Gomez C, Su R, Thompson A, DiSciacca J, Lawes S, Leach RK. Optimization of surface measurement for metal additive manufacturing using coherence scanning interferometry. Optical Engineering. 2017 Jul;56(11):111714.

[157] Kim F, Villarraga-Gómez H, Moylan S. Inspection of Embedded Internal Features in Additive Manufactured Metal Parts Using Metrological x-ray Computed Tomography. InAmerican Society Precision Engineering 2016 Summer Topical Meeting 2016 (pp. 191-195).

[158] Kerckhofs G, Pyka G, Loeckx D, Van Bael S, Schrooten J, Wevers M. The combined use of micro-CT imaging, in-situ loading and non-rigid image registration for 3D experimental local strain mapping on porous bone tissue engineering scaffolds under compressive loading. InProceedings of European Conference for non-Destructive Testing (ECNDT) 2010 Jun.

[159] Foster BK, Reutzel EW, Nassar AR, Hall BT, Brown SW, Dickman CJ. Optical layerwise monitoring of powder bed fusion. In Proc. 2015 Solid Freeform Fabrication Symposium, Austin, TX. 2015 Aug; pp: 10-12.

[160] Martin KF. A review by discussion of condition monitoring and fault diagnosis in machine tools. International Journal of Machine Tools and Manufacture. 1994 May 1; 34(4):527-51.

[161] Xie Z, Wang J, Zhang Q. Complete 3D measurement in reverse engineering using a multi-probe system. International Journal of Machine Tools and Manufacture. 2005 Oct 1; 45(12-13):1474-86.

[162] Zhang Z, Huang S, Meng S, Gao F, Jiang X. A simple, flexible and automatic 3D calibration method for a phase calculation-based fringe projection imaging system. Optics Express. 2013 May 20; 21(10):12218-27.

[163] Zhang Z. A flexible new technique for camera calibration. IEEE Transactions on pattern analysis and machine intelligence. 2000 Nov;22(11):1330-4.

[164] Lippiello V, Villani L. Managing redundant visual measurements for accurate pose tracking. Robotica. 2003 Oct;21(5):511-9.

[165] Fitzgibbon A, Pilu M, Fisher RB. Direct least square fitting of ellipses. IEEE Transactions on pattern analysis and machine intelligence. 1999 May; 21(5):476-80.

[166] Ayodele TO. Types of machine learning algorithms. New advances in machine learning. 2010 Feb 1;3:19-48.

[167] Maulud D, Abdulazeez AM. A Review on Linear Regression Comprehensive in Machine Learning. Journal of Applied Science and Technology Trends. 2020 Dec 31;1(4):140-7.

[168] Noble WS. What is a support vector machine?. Nature biotechnology. 2006 Dec;24(12):1565-7.

[169] Zhang Z. Introduction to machine learning: k-nearest neighbors. Annals of translational medicine. 2016 Jun;4(11).

[170] Dreiseitl S, Ohno-Machado L. Logistic regression and artificial neural network classification models: a methodology review. Journal of biomedical informatics. 2002 Oct 1;35(5-6):352-9.

[171] Navada A, Ansari AN, Patil S, Sonkamble BA. Overview of use of decision tree algorithms in machine learning. In2011 IEEE control and system graduate research colloquium 2011 Jun 27 (pp. 37-42). IEEE.

[172] Likas A, Vlassis N, Verbeek JJ. The global k-means clustering algorithm. Pattern recognition. 2003 Feb 1;36(2):451-61.

[173] Liaw A, Wiener M. Classification and regression by randomForest. R news. 2002 Dec 3;2(3):18-22.

[174] Saritas MM, Yasar A. Performance analysis of ANN and Naive Bayes classification algorithm for data classification. International Journal of Intelligent Systems and Applications in Engineering. 2019 Jun 30;7(2):88-91.

[175] Van Der Maaten L, Postma E, Van den Herik J. Dimensionality reduction: a comparative. J Mach Learn Res. 2009 Oct 26;10(66-71):13.

[176] Chen T, He T, Benesty M, Khotilovich V, Tang Y, Cho H. Xgboost: extreme gradient boosting. R package version 0.4-2. 2015 Aug 1;1(4):1-4.

[177] Qi CR, Su H, Mo K, Guibas LJ. Pointnet: Deep learning on point sets for 3d classification and segmentation. InProceedings of the IEEE conference on computer vision and pattern recognition 2017 (pp. 652-660).

[178] Qian J, Feng S, Tao T, Hu Y, Liu K, Wu S, Chen Q, Zuo C. High-resolution real-time 360 3D model reconstruction of a handheld object with fringe projection profilometry. Optics letters. 2019 Dec 1;44(23):5751-4.

[179] Marrugo AG, Gao F, Zhang S. State-of-the-art active optical techniques for three-dimensional surface metrology: a review. JOSA A. 2020 Sep 1;37(9):B60-77.

[180] Zhao H, Xu Y, Jiang H, Li X. 3D shape measurement in the presence of strong interreflections by epipolar imaging and regional fringe projection. Optics express. 2018 Mar 19;26(6):7117-31.

[181] Pal M, Foody GM. Feature selection for classification of hyperspectral data by SVM. IEEE Transactions on Geoscience and Remote Sensing. 2010 Feb 22;48(5):2297-307.

[182]Mavroforakis ME, Theodoridis S. A geometric approach to support vector machine (SVM) classification. IEEE transactions on neural networks. 2006 May 8;17(3):671-82.

[183]Romero R, Iglesias EL, Borrajo L. A linear-RBF multikernel SVM to classify big text corpora. BioMed research international. 2015 Jan 1;2015.

[184] Sun L, Fu S, Wang F. Decision tree SVM model with Fisher feature selection for speech emotion recognition. EURASIP Journal on Audio, Speech, and Music Processing. 2019 Dec;2019(1):1-4.

[185] Zhang Z, Chang C, Liu X, Li Z, Shi Y, Gao N, Meng Z. Phase measuring deflectometry for obtaining 3D shape of specular surface: a review of the state-of-the-art. Optical Engineering. 2021 Feb;60(2):020903.

[186] Hesch JA, Mourikis AI, Roumeliotis SI. Mirror-based extrinsic camera calibration. InAlgorithmic Foundation of Robotics VIII 2009 (pp. 285-299). Springer, Berlin, Heidelberg.

[187] Hesch JA, Mourikis AI, Roumeliotis SI. Camera to robot-body calibration using planar mirror reflections. University of Minnesota, Dept. of Comp. Sci. & Eng., Tech. Rep. 2008 Jul;1.